Investigation of Thermoelectric Properties of Lead-free Tin Telluride and Skutterudite

A thesis submitted in Partial Fulfillment of the Degree of

MASTER OF SCIENCE

as a part of

Integrated Ph.D. Programme (Chemical Science)

By

Ananya Banik

New Chemistry Unit

Jawaharlal Nehru Centre for Advanced Scientific Research

(*A deemed University*)

Bangalore, India

(March 2015)

Dedicated to my beloved parents

Declaration

I hereby declare that this thesis entitled "*Investigation of Thermoelectric Properties of Lead-free Tin Telluride and Skutterudite*" is an authentic record of research work that has been carried out by me at Solid State Chemistry Laboratory, New Chemistry Unit, Jawaharlal Nehru Centre for Advanced Scientific Research, Bangalore, India under supervision of Dr. Kanishka Biswas. This work has not been submitted elsewhere for the award of any degree or diploma. Whenever contributions of others are required, every effort is made to indicate it clearly, with due reference to the literature, and acknowledgement of collaborative research and discussions.

Date :
Bangalore, India Ananya Banik

Certificate

Certified that the work described in this thesis titled "*Investigation of Thermoelectric Properties of Lead-free Tin Telluride and Skutterudite*" has been carried out by Ms. Ananya Banik at Solid State Chemistry Laboratory, New Chemistry Unit, Jawaharlal Nehru Centre for Advanced Scientific Research, Bangalore, India under my supervision and that it has not been submitted elsewhere for the award of any degree or diploma.

Date :
Bangalore, India

Dr. Kanishka Biswas
(Research Supervisor)

Acknowledgements

Completion of my M.S. thesis necessitated a lot of guidance and supports from many people. I take this opportunity to mention a few of them. However, my sincere thanks extend to everyone who has played a role in making this dream a reality.

Firstly, I would like to thank my research supervisor, Dr. Kanishka Biswas for suggesting me research problems and guiding me throughout. He has been a constant source of inspiration for me. I greatly admire his enthusiasm towards science. I express my hearty gratitude to him for giving me an opportunity to work under his guidance. I also wish to thank him for correcting me with patience and for forgiving my flaw.

I would like to thank Prof. C. N. R. Rao, FRS, the chairman of New Chemistry Unit (NCU) for his generous support and encouragement throughout my stay in JNCASR. His presence has given me immense inspiration to indulge in active research. I also thank him for providing the infrastructure and facilities to carry out my research work. I am grateful to him for giving me the opportunity to do semester projects in his laboratory.

I would like to thank our collaborator, Prof. U. Waghmare and his students, Dr. Sandhya Shenoy and Shashwat Anand. I have learnt a lot whenever we had meeting with them or discussion with them. I am grateful to Prof. A. Sundaresan for allowing me to use PPMS for Hall measurement.

I thank my past and present lab mates Satya Narayan, Manoj, Arindom, Subhajit, Dr. Suresh and Dr. Chithaiah for their cheerful company and help in various occasions. I got the opportunity to learn a lot about research and many instruments from them. Their discussion on past experience, valuable inputs about research life and experiments helped me immensely.

I would like to thank JNCASR for providing me all the facilities.

I would like to express my sincere thanks to Prof. T. Govindaraju for giving me the opportunity to do semester projects in his laboratory.

I am thankful to all faculty members of New Chemistry Unit and Chemistry & Physics Material Science Unit of JNCASR for their courses. In particular, I would like to thank Prof. U. Waghmare for valuable discussions, during and after my course work.

I am thankful to Sunita, Rana, Nagarjuna, Promoda and Dr. Maity for their help during semester projects and introducing me to the way of research. I thank Mr. Somnath Ghara for his help during Hall measurement.

Constant assistance and a friendly nature of the technical staff helped me doing my experiments smoothly. Here, I would like to acknowledge Mrs. Usha (TEM), Mrs. Selvi (FESEM), Mr. Anil (XRD), Mr. Vasu (IR) and Mrs. Bhavya (SEM) for their technical help. I am thankful to all the academic, administrative, technical, security, complab and health center staffs for making our campus life smooth and easy.

I express my deep gratitude to all my high school and undergraduate teachers for training me to be disciplined, the basics of science and for growing my interest in research field.

I thank all of my 2012 Int. Ph. D. batch mates for having a wonderful time with them.

I have been benefited a lot from my senior Ph.D. and Int. Ph.D. students. Their help and advice made my academic and non academic life a memorable and comfortable one here at JNC. I am thankful to all of them. A special thanks to Sohini, Dipanwita, Soumyabrata, Syamantak, Chandradhis and Moumita for all the moments I spent with them and also for supporting me any time I required. I also thank Balaka, Amrita, Saurav, Arka, Asmita, Anwesadi for the joyous time we spent.

Lastly, I would like to acknowledge the most important people of my life, my parents and my family. Without their unconditional love and support all my efforts would have gone to vain. I am grateful to you all for whatever you gave me and I dedicate my thesis to you.

Preface

Thermoelectric effect enables direct conversion of thermal to electrical energy or vice versa and provides an alternative route for power generation and refrigeration. Although PbTe is most efficient material for power generation application, environmental concern about lead (Pb) prevents its use in thermoelectric module for large scale applications. Hence, the goal of thermoelectric community is to design Pb- free thermoelectric materials with high efficiency. The thesis entitled "*Investigation of Thermoelectric Properties of Lead-free Tin Telluride and Skutterudite*" demonstrates the study of electronic structure and optimization of the thermoelectric properties of SnTe and $CoSb_3$. The thesis has been divided into four chapters.

Chapter I of this thesis begins with a brief introduction of thermoelectrics and its useful approaches to solve energy related issues. Herein, I have discussed the key concept in the field of thermoelectric material research along with the present understanding and latest development.

Chapter II discusses about the promising thermoelectric performance of Pb-free Indium (In)-doped $SnTe_{1-x}Se_x$ (x = 0-0.15) system. SnTe, a lead-free rock-salt analogue of PbTe, having valence band structure similar to PbTe, recently has attracted attention for thermoelectric heat to electricity generation. Resonant level formation in the valence band through In doping along with the increase in the contribution of heavy hole valence band through solid solution alloying significantly improved the Seebeck coefficient, which resulted a promising thermoelectric figure of merit, *ZT*, of ~0.8 at 860 K in *p*-type 1.5 mol% In doped $SnTe_{0.85}Se_{0.15}$ sample.

Chapter III deals with the effect of Mg alloying on the electronic structure and the thermoelectric properties of SnTe. Incorporation of Mg in SnTe decreases energy difference between the light hole and heavy hole valence bands, leading to an enhanced Seebeck coefficient which results maximum *ZT* of ~1.2 at ~860 K for *p*-type $Sn_{0.94}Mg_{0.09}Te$.

Chapter IV deals with low temperature soft chemical synthesis and thermoelectric properties of Ba-filled *p*-type skutterudite ($CoSb_3$) nanocrystals. Efficient phonon scattering by nanoscale grain boundaries and the additional phonon damping due to the rattling of Ba in the void of nanocrystalline $CoSb_3$ give rise to low thermal conductivity, which results in improved thermoelectric performance in nanocrystalline *p*-type $Ba_{0.048}CoSb_3$.

Contents

Chapter 1

A Brief Introduction to Thermoelectrics

1.1. Introduction

The rising global energy demand is causing a dramatic acceleration of social unrest. Impact of climate change on the environment due to combustion of nonrenewable energy sources is becoming increasingly alarming. Driven by the demand for clean and sustainable energy sources, thermoelectricity has become a significant part of research portfolio seeking to identify new and efficient energy materials for power generation, as ~60% of energy is inevitably lost through heat dissipation (Figure 1.1).[1, 2] Exhaust from domestic heating, automobiles and industrial processes produce a large amount of unused waste heat that could be converted to electricity by using thermoelectric devices (Figure 1.1).[2, 3] As thermoelectric generators are all solid-state devices without any mobile parts, they are suitable for small-scale power generation and distribution.[4] For the past 40 years, thermoelectric generators have consistently provided power in remote terrestrial and extraterrestrial locations, especially on deep space probes such as Voyager.[3] Solid-state Peltier coolers offer precise thermal management for optoelectronics and passenger seat-cooling in automobiles. Efforts are already underway to replace the alternator in cars with a thermoelectric generator mounted on the exhaust stream, thereby improving the fuel efficiency.[3] The reliability and

stability of thermoelectrics makes them suitable for wider applications such as sub-ambient cooling of infrared detectors and thermal management systems in microprocessors etc.[3]

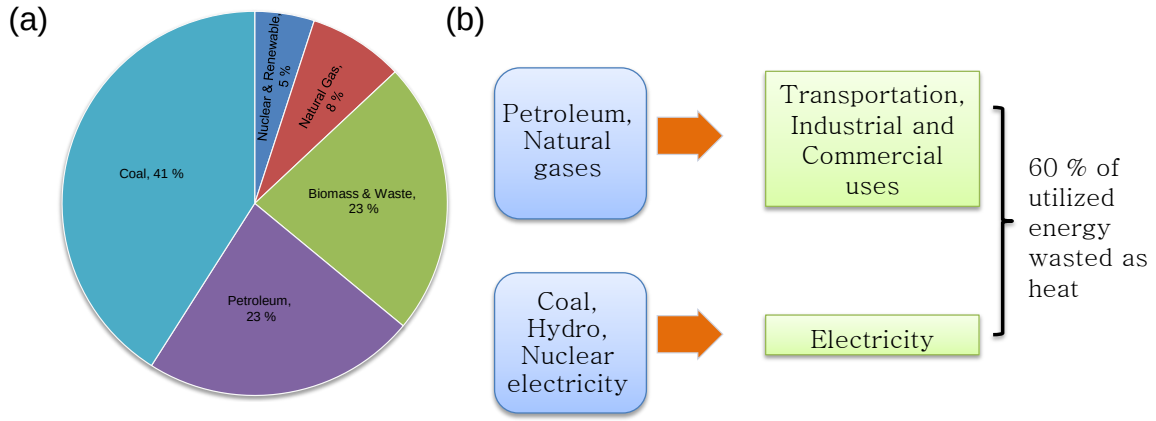

Figure 1.1 (a) Total energy consumption by type for India in year 2011 [Source-Ref 1]. (b) Schematic demonstrates how ~60 % of the utilized energy being lost as waste heat.

1.2. Origin of thermoelectric effect

Thermoelectric effect is related to direct and reversible conversion of waste-heat to electricity and vice versa.[5] It is based on two important transport effects: Seebeck effect and Peltier effect.

According to Seebeck effect, if two dissimilar metals are joined together with the junctions kept at different temperatures (temperature difference is ΔT), then a voltage difference (ΔV) will generate.[6] This voltage difference will be proportional to ΔT. The ratio of the generated voltage to the temperature difference (ΔV / ΔT) is related to an intrinsic property of the materials termed as Seebeck coefficient (S) or the thermopower (equation 1). This effect can be understood by establishing a temperature gradient across a material-the more energetic carriers of hot junction diffuse to a lower potential i.e. cold junction until an electric field is established to hinder the further flow of carriers.[7]

$$S = \frac{\Delta V}{\Delta T} \quad (1)$$

The inverse Seebeck effect is known as Peltier effect where the metal junctions either release or absorb the heat while current is passed in the close circuit.[8] The release or absorption of heat at metal junctions entirely depends on the direction of applied current. In a Peltier cooler, the circuit is connected to a d.c. power supply which drives the electric current (*I*) and heat flow (*Q*), thereby cooling the hot end due to the Peltier effect ($Q = STI$, where *T* is temperature in Kelvin scale).

Seebeck coefficient is very low for metals (of the order of 1 to 10 μV/K) and much larger for semiconductors (10^2-10^3μV/K).[7] For example, the degenerate semiconductor like *p*-Bi_2Te_3 has the *S* value of around 225 μV/K (holes are responsible for the positive value of Seebeck).[7] Hence the use of semiconductor materials can offer considerable amount of voltage generation for a given temperature gradient.

Thermoelectric (TE) couple consists of both *p*-type (positive Seebeck coefficient and hole carriers) and *n*-type (negative Seebeck coefficient and electron carriers) semiconductors connected through metallic conducting pad.[7] A TE module or device comprises an array of TE couples, which are arranged electrically in series and thermally in parallel.[3] Both refrigeration and power generation may be accomplished using the same module as shown in figure 1.2. In a thermoelectric generator, when temperature gradient is applied, the thermally excited holes from *p*-type and electrons from *n*-type semiconductor diffuse towards cold side from hot side and generate power in electric load connected through external circuit. Here, temperature difference produces the voltage (equation 1) and heat flow drives the electrical current, which determines the power output. As thermoelectric modules convert the localized

waste heat into electricity or vice versa, it is our choice of interest to use in various fields such as, waste heat utilization from all heat engines and automobiles, portable coolers, thermal management system in microprocessors. Performance of these devices depends on semiconducting materials used as *p*- and *n*-type leg. In the following section, I will focus on the parameters which determine conversion efficiency of these materials.

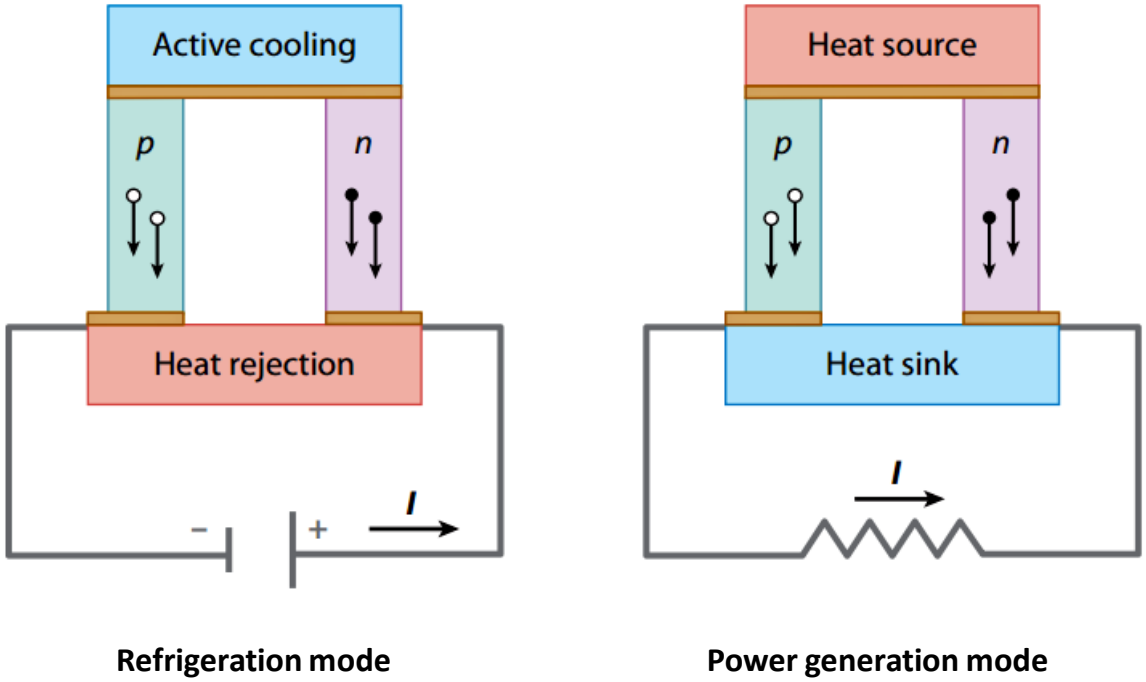

Figure 1.2 Generic diagram of a thermoelectric couple made of *n*-type and *p*-type thermoelectric materials. Power generation or refrigeration modes are possible, depending on the configuration.

1.3. Thermoelectric figure of merit (ZT)

In the early 1900s, E. Altenkirch introduced the concept of figure of merit.[8] It qualitatively showed that good thermoelectric materials should have high electrical conductivity (σ) to minimize Joule heating, low thermal conductivity (κ) to preserve heat at the junctions and maintain a large temperature gradient, and large Seebeck coefficients (S)

for maximum conversion of heat to electrical power or electrical power to heat. These properties define the dimensionless thermoelectric figure of merit, *ZT* as

$$ZT = \frac{\sigma S^2}{\kappa} T \tag{2}$$

where *T* is the temperature in Kelvin.[2, 3, 5, 7, 9-16] The quantity σS^2 is called the power factor and is the key to achieve high performance. A large power factor means that a large voltage and a high current generation. The thermal conductivity κ has a contribution from lattice vibrations, κ_{lat}, called the lattice thermal conductivity. Thus, $\kappa = \kappa_{el}+\kappa_{latt}$, where κ_{el} is the electronic thermal conductivity.

For power generation, the thermoelectric efficiency (η) is defined by combining the Carnot efficiency ($\eta_c = \Delta T/T_{hot}$) and the average figure of merit (ZT_{av}) as shown in equation 3.[5]

$$\eta_{TE} = \eta_c \frac{\left(\sqrt{1+ZT_{av}}-1\right)}{\left(\sqrt{1+ZT_{av}}+\frac{T_{cold}}{T_{hot}}\right)} \tag{3}$$

where T_{hot} and T_{cold} are the temperature of the hot and cold ends in a thermoelectric device and ΔT is their difference. Equation 3 indicates that increasing efficiency requires both high *ZT* values and a large temperature difference across the thermoelectric materials. Figure 1.3 illustrates the maximum conversion efficiency dependence of *ZT* for a given working temperature.[7, 17] As shown in figure 1.3, for T_{cold} = 300 K and T_{hot} = 800 K, if the $ZT \sim 2$, the maximum η is around 15-18 %, which is much lower than the Carnot efficiency (62.5%).[17] Market based thermoelectric devices currently available have a ZT_{av} of ~1 and operate at an efficiency of only around 6–8 %.[5] By increasing ZT_{av} a factor of 4, and depending on ΔT, the predicted efficiency can be increased to 30 %, a highly attractive prospect.

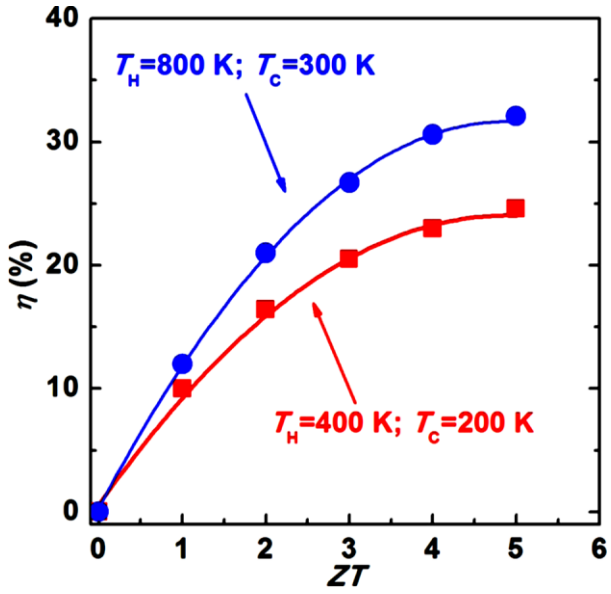

Figure 1.3 The maximum conversion efficiency dependence of figure of merit (*ZT*) values under certain working temperature.

1.4. Conflicting thermoelectric parameters

Fundamental to the field of thermoelectric materials is the need to optimize a variety of conflicting properties. To obtain a high figure of merit (*ZT*), high electronic conductivity (σ), high thermopower (*S*) and low thermal conductivity (κ) are required in a single material (equation 2).[5,18-22] As these transport characteristics depend on interrelated material properties, a number of parameters need to be optimized to maximize *ZT*.

1.4.1. Carrier concentration

For large Seebeck coefficient, there should be only single type of carrier.[3] Mixed *n*-type and *p*-type conduction will lead to both charge carriers moving to the cold end, cancelling out the induced Seebeck voltages. Insulators and semiconductors (in both cases carrier concentration is low) have very high Seebeck coefficients (equation 4), but very low electrical conductivity (see equation 5). The interrelationship between carrier concentration and Seebeck coefficient can be seen from the models of electron transport. For metals

or degenerate semiconductors (single parabolic band and energy-independent scattering approximation) [3] the Seebeck coefficient is given by:

$$S = \frac{8\pi^2 k_B^2}{3eh^2} m^* T \left(\frac{\pi}{3n}\right)^{2/3} \quad (4)$$

where n is carrier concentration and m^* is effective mass.

Electrical conductivity (σ) is related to n through the following expression.

$$\sigma = ne\mu \quad (5)$$

Here μ is carrier mobility. Figure 1.4 shows compromise between large thermopower and high electrical conductivity in thermoelectric materials to maximize the figure of merit, *ZT*. The peak value of *ZT* arises in the carrier concentration range of 10^{19}-10^{21} cm^{-3} (Figure 1.4) which falls in between metals and semiconductors - that is concentration found in heavily doped semiconductors (degenerate semiconductor).[3, 5]

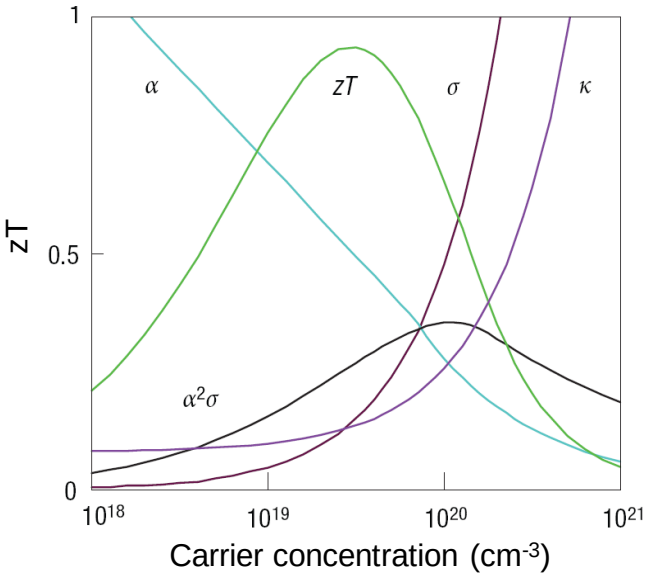

Figure 1.4 Optimizing *zT (~ZT)* through carrier concentration tuning. Maximization of *ZT* of a thermoelectric material involves a compromise of thermal conductivity (κ, plotted on the y axis from 0 to a top value of 10 $Wm^{-1}K^{-1}$) and Seebeck coefficient (S, 0-500 μVK^{-1}) with electrical conductivity (σ; 0 to 5,000 Scm^{-1}). Adapted with permission from ref. 3 *(Nat. Mater.* **2008**, *7*, 105). © 2008 Nature Publishing Group.

1.4.2. Effective mass

The effective mass of the charge carrier offers another conflict as large effective masses generate high thermopower but low electrical mobility. The m^* in equation (4) refers to the density-of-states effective mass, which increases with flat and narrow bands with high density of states at the Fermi surface. However, as the inertial effective mass is also related to m^*, heavy carriers will move with slower velocities, and therefore small mobility, which in turn leads to low electrical conductivity (equation 5). The precise relationship between effective mass and mobility is complex, and depends on electronic structure, scattering mechanism and anisotropy. In principle, these effective mass terms can be decoupled in anisotropic crystal structures.[3, 5] A equilibrium must be found for the effective mass (or bandwidth) for the dominant charge carrier, forming a compromise between high effective mass and high mobility. Optimum effective mass for thermoelectric is not known; good thermoelectric materials can be found within a wide range of effective masses and mobility: from low-mobility, high-effective-mass polaron conductors (oxides,[3] chalcogenides[3]) to high-mobility, low-effective-mass semiconductors (SiGe, GaAs). [5]

1.4.3. Electrical thermal conductivity

Additional confliction in material design comes from the necessity for low thermal conductivity.[3] Thermal conductivity in thermoelectrics appears from two sources: (1) electrons and holes transporting heat (κ_{el}) and (2) phonons travelling through the lattice (κ_{lat}). Here κ_{el} is directly related to the electrical conductivity through the Wiedemann–Franz law:

$$\kappa_{el} = L\sigma T \tag{6}$$

where L is the Lorenz factor, $2.4 \times 10^{-8}\,\mathrm{W\Omega K^{-2}}$ for free electrons.

The Lorenz factor can vary with carrier concentration. Accurate evaluation of κ_{el} is important, as κ_{lat} is often computed as the difference between κ_{total} and κ_{el} using the experimental electrical conductivity. Ambiguity in κ_{el} happens due to mixed conduction, which introduces bipolar term into the thermal conductivity. As this term is not considered into the Wiedemann–Franz law, the standard computation of κ_{lat} erroneously takes account of bipolar thermal conduction. This results in a perceived increase in κ_{lat} at high temperatures for low band gap materials like Bi_2Te_3 and PbTe.[5]

1.4.4. Lattice thermal conductivity

Glasses exhibit very low lattice thermal conductivity. In a glass, thermal conductivity is considered as a random walk of energy throughout a lattice rather than rapid transport via phonons, and leads to the concept of a minimum thermal conductivity, κ_{min}.[3] Actual glasses, however, make poor thermoelectrics because of the absence of needed 'electron-crystal' properties, required for superior electrical transport property (σ) — compared with crystalline semiconductors, they have lower mobility due to increased electron scattering and lower effective masses because of broader bands. Good thermoelectric materials are therefore crystalline materials that manage to scatter phonons without significantly interrupting the electrical conductivity.[3] The heat flow is carried by a spectrum of phonons with widely varying wavelengths and mean free paths (from less than 1 nm to greater than 10 μm), creating a need for phonon scattering agents at a variety of length scales.[3]

1.5. Ways to achieve high performance

1.5.1. Increment of the power factor

Several years ago Slack portrayed the chemical characteristics of materials that might prove

to be candidates for a good TE material; namely, the candidate materials should be narrow-band gap semiconductors with high-mobility carriers.[7] Mahan and colleagues[23, 24] also described characteristics of good TE materials. The potential materials are typically narrow-band-gap semiconductors (e.g., $E_G \approx 10k_BT$ or ≈ 0.25 eV at 300 K). Also, the mobility of the carriers must remain high. In semiconductors, the Seebeck coefficient and the electrical conductivity (both in the numerator of *ZT*) depend on the doping level and chemical composition. Therefore, these quantities must be optimized by electronic engineering for good TE performance.

The least unsolved problem in current research is to enhance the thermoelectric power of materials without sacrificing the electrical conductivity and to predict precisely which materials will have a high power factor. Increase in m^* can improve Seebeck coefficient (see equation 4). Hence one approach is to enhance σS^2 by creating distortions in the electronic density of states (DOS) near the Fermi energy. The well-known approaches in this regard are 1) formation of resonant level near Fermi energy and 2) convergence of electronic valleys.

Formation of resonant levels

Electronic transport properties of semiconductor generally follow Boltzmann theory. According to this, the Seebeck coefficient strongly depends on energy derivative of carrier density ($n(E)$) and mobility (μ) via Mott relation (equation 7), in which slight changes in the DOS can alter the *S* value.[25]

$$S = \frac{\pi^2}{3}\frac{k_B}{q}k_BT\left\{\frac{d[ln(\sigma(E))]}{dE}\right\}_{E=E_F} \tag{7}$$

$$= \frac{\pi^2}{3}\frac{k_B}{q}k_BT\left\{\frac{1}{n}\frac{dn(E)}{dE} + \frac{1}{\mu}\frac{d\mu(E)}{dE}\right\}_{E=E_F}$$

Here, $\sigma(E)$ is the electronic conductivity determined as a function of the band filling or Fermi energy, E_F ($\sigma(e) = n(E)q\mu(E)$) and $n(E)$ ($n(E) = g(E)f(E)$), the carrier density at the energy level, E (here q is the carrier charge, and $\mu(E)$ is the mobility as a function of energy, $f(E)$ is the Fermi function, *g(E) is density of state*). When electronic scattering is independent of energy, $\sigma(E)$ is just proportional to the density of states (DOS) at *E*. Figure 1.5, shows two hypothetical DOS diagrams. In figure 1.5 (a) the DOS varies rapidly near E_F and in figure 1.5(b) it does not. Based on the above expression it is clear that the system with rapid changing DOS near E_F is expected to have large thermopower.

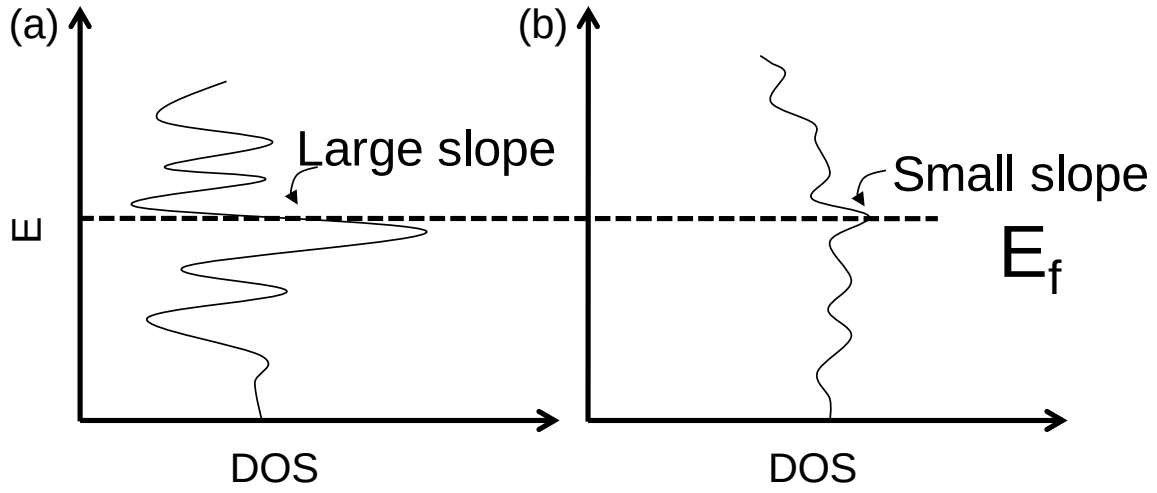

Figure 1.5 Hypothetical density of state (DOS) with (a) a large slope (d lnσ(E)/dE) and (b) a small slope near E_F.

Mahan and Sofo theory suggests that there are possibilities of the formation of the resonant states, from the impurity states, near to E_F of the semiconductors.[26] Heremans, *et al*. demonstrated experimentally that Tl doping improves *S* of PbTe by resonant level formation and thereby achieved the double value of *ZT*, as seen in the figure 1.6.[26]

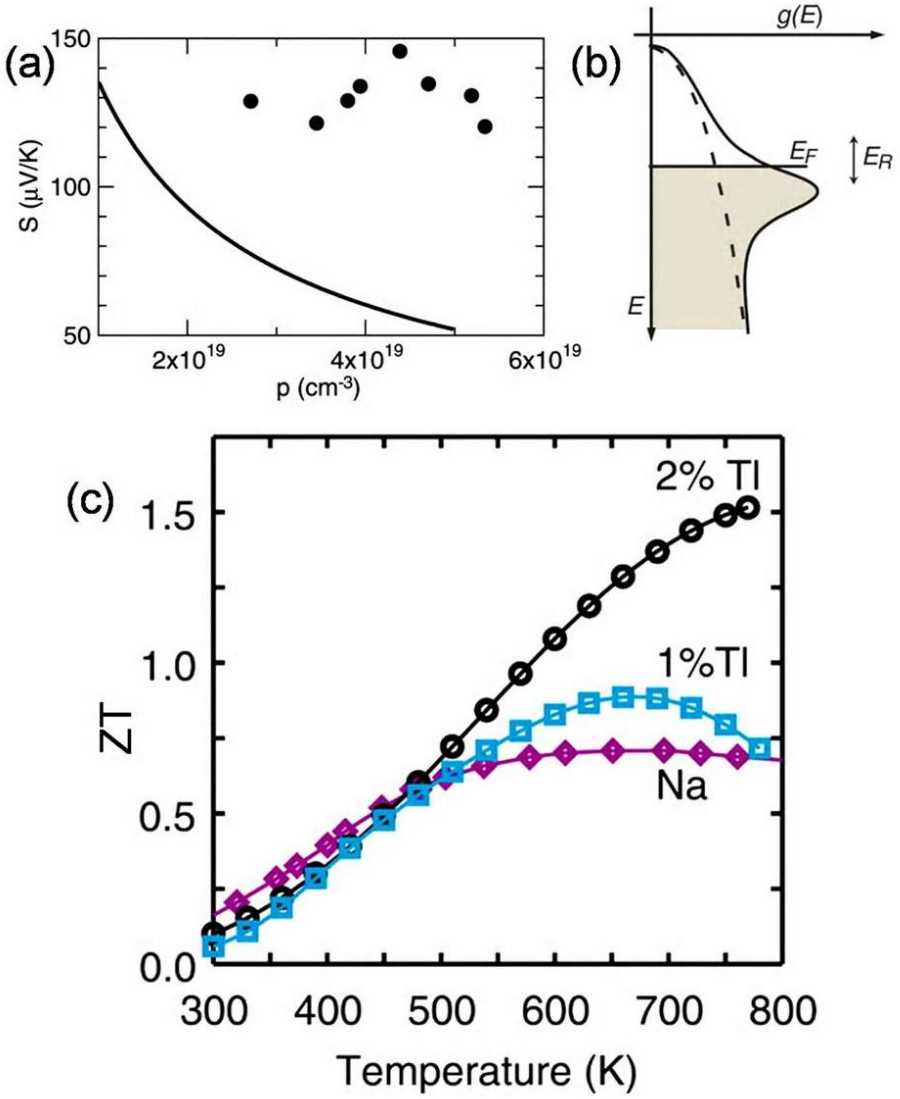

Figure 1.6 (a) Pisarenko relation of Seebeck coefficient versus hole concentration for PbTe (solid line) at 300 K compared to the results on Tl-PbTe sample. Significantly large *S* value in Tl-doped PbTe confirmed the presence of resonance level. (b) The formation of Tl resonant state (solid line) on PbTe DOS (dashed line). (c) The temperature dependent *ZT* values for $Tl_{0.02}Pb_{0.98}Te$ (black circles) and $Tl_{0.01}Pb_{0.99}Te$ (blue squares) compared to that of a reference sample of Na-PbTe (purple diamonds). Adapted with permission from ref. 26 (*Science* **2008**, *321*, 554). © 2008 AAAS.

Convergence of electronic valleys

Multiple pockets in valence or conduction band extreme gives rise to high Seebeck coefficient. Multiple degenerate valleys (separate pockets of Fermi surface with the same

energy) have the effect of producing large effective mass (m*) without explicitly reducing μ as shown in equation 8.[27] Hence, when the system is heavily doped, more valleys are populated, thus resulted in high power factor. Convergence of multiple charge carrying electronic band valleys is another effective way to create large effective mass.

$$m* = N_V m_b^* \tag{8}$$

Here N_V represents orbital degeneracy and m_b^* represents single valley density of state effective mass of degenerate valleys.

Pei *et al.* have demonstrated the band convergence of at least 12 valleys in doped $PbTe_{1-x}Se_x$ alloys, leading to an extraordinarily high *ZT* value of 1.8 at about 850 K, as seen in figure 1.7.[27] Alloying Se reduces the energy difference between the L and Σ bands of the PbTe making the two bands effectively converged. Hence enhancement in N_V from 4 (for L band) to 12 (for Σ band) results increase in m^*.

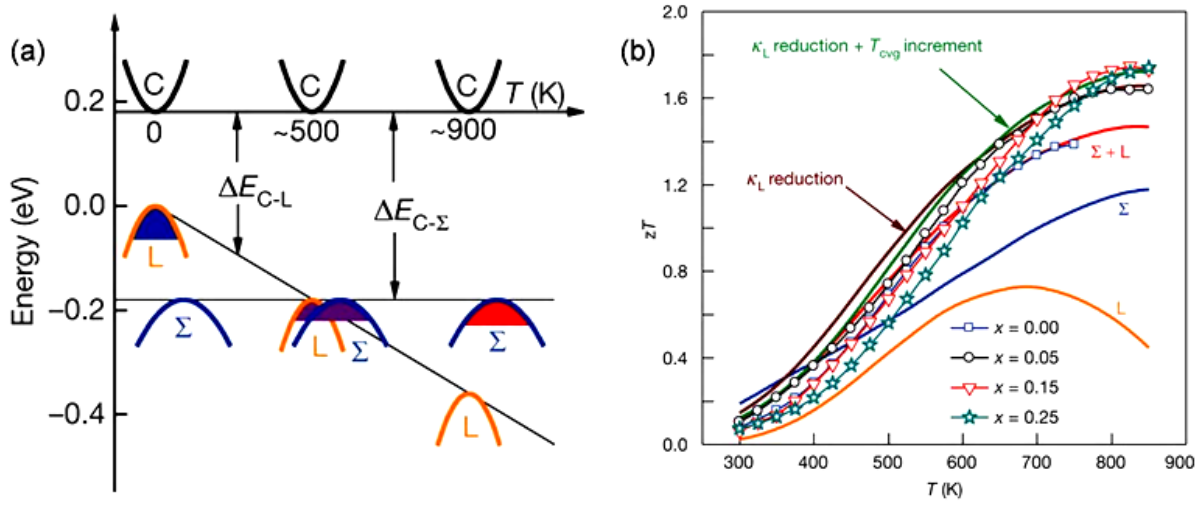

Figure 1.7 (a) Relative energy of the valence bands in $PbTe_{0.85}Se_{0.15}$. At, 500 K the two valence bands converge, resulting in transport contributions from both the L and Σ bands. (b) Temperature dependence of the *zT (~ ZT)* of *p*-$PbTe_{1-x}Se_x$ materials doped with 2 atom % Na. Adapted from ref. 27 (b) *(Nature* **2011**, *473*, 66) with permission. © 2011 Nature Publishing Group.

1.5.2. Reduction of thermal conductivity

As κ_{el} is proportional to σ by Wideman-Franz law (equation 6), the only way to decrease total thermal conductivity (κ_{total}) is to manipulate the lattice thermal conductivity (κ_{lat}). Above Debye temperature, κ_{lat} primarily depends on phonon mean free path; that means materials with higher phonon- phonon scattering will show lower value of κ_{lat}.[3]

A successful strategy to increase the *ZT* value is the optimization of an already promising compound by introducing point defects through the synthesis of isostructural solid solutions. Solid solution will provide environment of mass fluctuation throughout the crystal lattice (i.e. disorder) which induces strong phonon scattering and generally can lead to significantly lower thermal conductivity and a larger *ZT* value. For example, solid solutions of $PbTe_{1-x}Se_x$ and $Pb_{1-x}Sn_xTe$ have the lower thermal conductivity than that of pure PbTe (see Figure 1.8).[28]

Nanoscale inclusions in bulk materials can dramatically suppress the lattice thermal conductivity by scattering the longer mean free path heat-carrying phonons, as in $AgPb_mSbTe_{m+2}$ (LAST-m) (Figure 1.8), which resulted high *ZT* of 1.8.[29] Calculations predict that a wide size distribution of nanoparticles is preferable since it can effectively scatter different phonon modes and reduce thermal conductivity. This phenomena was first observed in a high performance thermoelectric system, so-called LAST-m.[29] The thermal conductivity at room temperature has been reduced from 2.0–2.5 W /mK for PbTe to 0.5–0.8 W /mK for LAST-m. The very low lattice thermal conductivity of the LAST system was attributed to the spontaneous and ubiquitous nanoscale precipitation of second phases in the PbTe matrix. After this observation, nanostructures were also observed in LASTT ($Ag(Pb_{1-x}Sn_x)_mSbTe_{2+m}$)[30] and SALT ($NaPb_mSbTe_{2+m}$).[31]

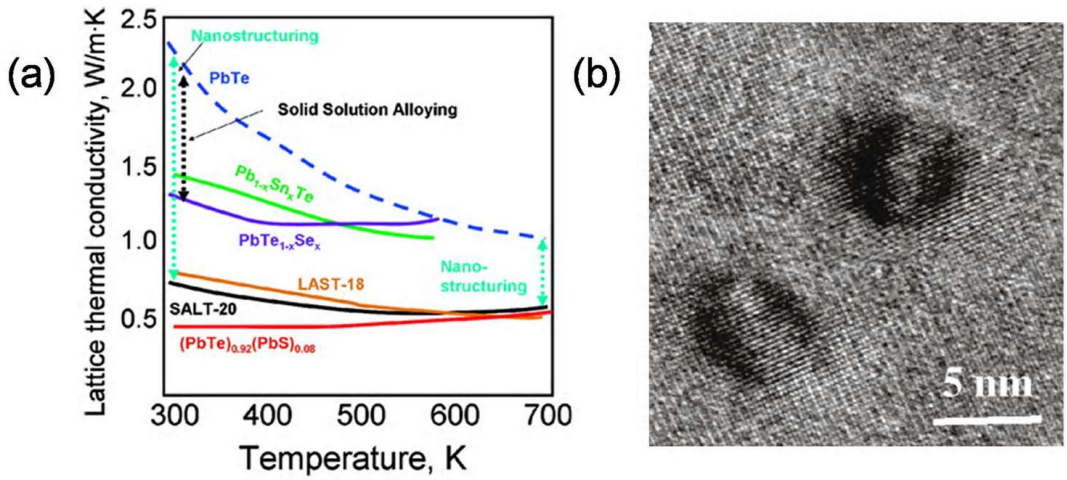

Figure 1.8 (a) Lattice thermal conductivity (κ_{lat}) as a function of temperature for various PbTe-based alloys and nanostructured samples. (b) High resolution transmission electron microscopy of a LAST-18 sample. Adapted with permission from ref. 28 (*Chem. Mater.* **2010**, *22*, 648). © 2010 American Chemical Society.

Another approach was proposed by Slack which was referred as 'phonon glass electron crystal (PGEC) approach.[32] In PGEC concept a glass like conductivity can co-exist with charge carriers of high mobility. A PGEC material contains cage or tunnel inside the crystal which reside massive atom that is small enough relative to the cage to rattle. This will produce phonon damping effect which result in significant reduction of thermal conductivity. Significant enhancement in *ZT* was observed for skutterudites and clathrates from PGEC approach.[33, 34]

1.6. State-of-art thermoelectric materials

In the recent decades, thermoelectric research is enjoying the "renaissance" period. Various innovative approaches have recently been introduced to improve *ZT such as* nanostructuring,[21] all-scale hierarchical architecturing,[2] matrix/precipitate band alignment,[11] formation of resonance level in electronic band[25, 26] and convergence of degenerate bands

through alloying.[27] Bi_2Te_3, an effective material for refrigeration, was first investigated by H. Julian Goldsmid in 1954.[35] The most commonly studied *p*-type compositions are near $(Sb_{0.8}Bi_{0.2})_2Te_3$ whereas *n*-type compositions are close to $Bi_2(Te_{0.8}Se_{0.2})_3$.[3, 36] For mid-temperature power generation, materials based on group IV- chalcogenides, such as PbTe and GeTe show best efficiency.[2, 37, 38] For high temperature applications, thermoelectric generators have typically used silicon–germanium alloys for both *n*- and *p*-type legs.[3] The *ZT* of these materials is quite low due to their high lattice thermal conductivity. Figure 1.9 shows the major milestones achieved for *ZT* over the past several decades as a function of both year and temperature.[12] In the following part, I will briefly discuss about most well known thermoelectric materials.

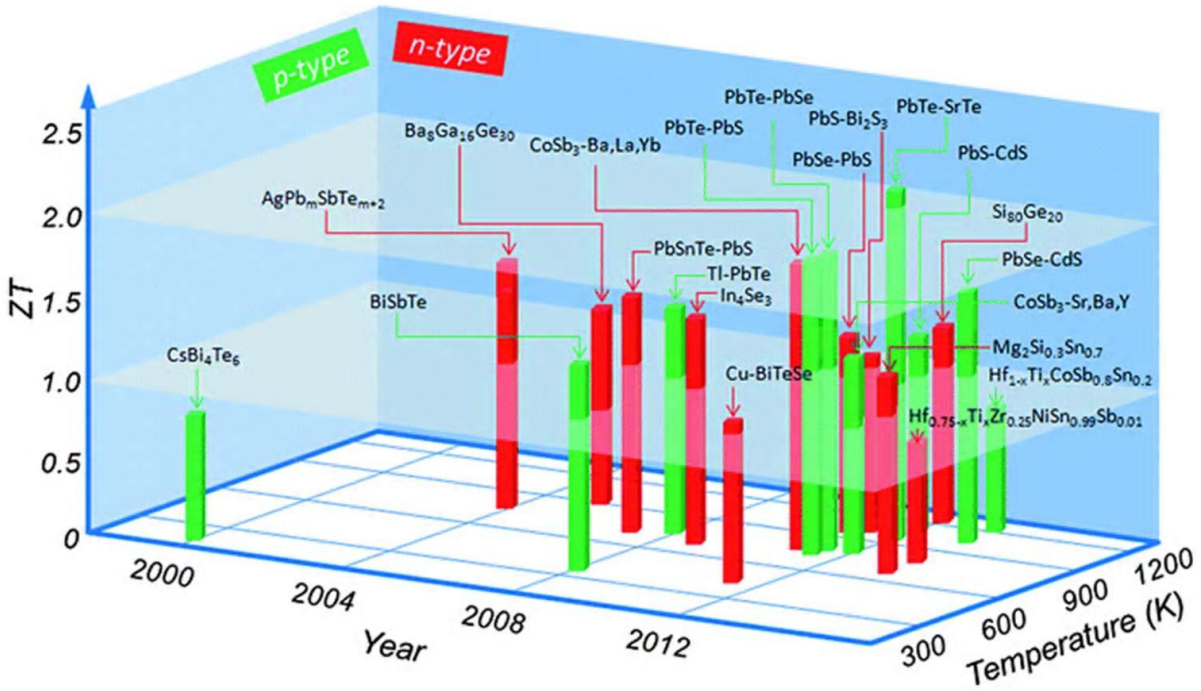

Figure 1.9 Current state-of-art bulk thermoelectric materials. Plot shows thermoelectric figure of merit (*ZT*) as a function of year and temperature. Adapted with permission from ref. 12 (*Energy Environ. Sci*. **2014**, *7*, 251). © 2014 Royal Society of Chemistry.

1.6.1. Bismuth chalcogenides

Bi_2Te_3 is a narrow-gap semiconductor with an indirect gap of ~0.15 eV. It crystallizes in the rhombohedral space group *R*-3*m*. The structure formed by of quintuple layers of Bi and Te (Te1-Bi-Te2-Bi-Te1); stacked by van der Waals interactions along the *c*-axis in the unit cell (Figure 1.10 (a)). This weak binding between the Te layers accounts for the ease of cleavage along the plane perpendicular to the *c*-axis and the anisotropic thermal and electrical transport properties of Bi_2Te_3.[7] The material with *ZT*~1.4 at 100 °C was prepared by ball milling followed by hot pressing (see Figure 1.10 (b)).[39] The *ZT* enhancement for this system arises from reducing the lattice thermal conductivity while maintaining a comparable power factor to that of the bulk *p*-type $Bi_{0.5}Sb_{1.5}Te_3$. This material is called "nanobulk" $Bi_{2-x}Sb_xTe_3$ and it is a single-phase material made of nanograins and micrograins mixed together (see Figure 1.10 (c)). Device made up with nanostructured Bi_2Te_3 has shown superior

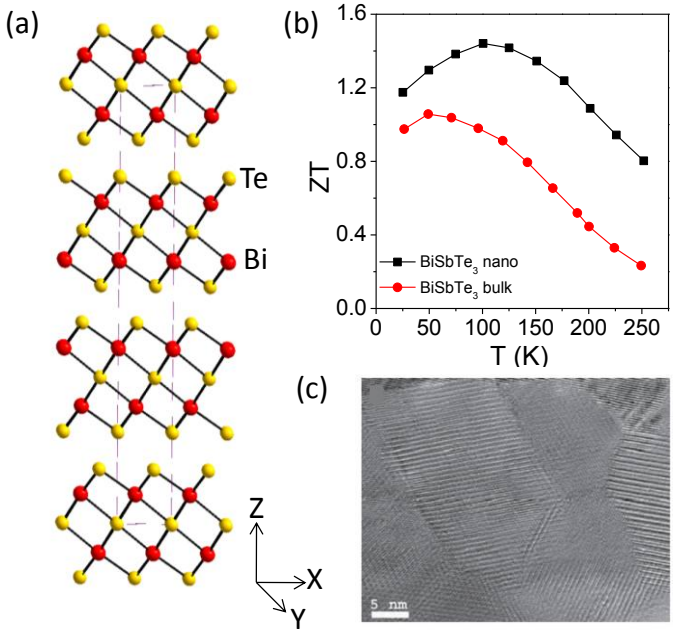

Figure 1.10 (a) Layered crystal structure of Bi_2Te_3. (b) Temperature dependent *ZT* of hot pressed nanostructured and market based ingot bismuth antimony telluride. (c) Transmission electron microscope (TEM) image showing nanocrystalline grain of high performance bismuth antimony telluride. Figure (b) and (c) are adapted with permission from ref. 39 **(***Science* **2008**, *320*, 634**).** © 2008 AAAS. http://www.sciencemag.org.

thermoelectric efficiency than that of the device from commercially available *p*-type Bi_2Te_3. Recently, promising thermoelectric performance has been achieved in nanostructured Bi_2Te_3, Sb_2Te_3 and their alloys synthesized by bottom up solution based microwave assisted synthesis.[40]

$CsBi_4Te_6$ is a promising material for low-temperature thermoelectric applications.[41] The presence of Bi-Bi bonds in the structure is responsible for the very narrow energy gap (~ 0.08 eV), nearly half of that of Bi_2Te_3. The narrower band gap is responsible for the maximum *ZT* value in $CsBi_4Te_6$ being at lower temperatures than in Bi_2Te_3. A *ZT* value of 0.8 at 225 K was obtained for 0.06 % SbI_3-doped $CsBi_4Te_6$.

1.6.2. Lead telluride

PbTe is the most efficient thermoelectric material for mid-range temperature (600–800 K) applications. It crystallizes in the NaCl crystal structure with Pb atoms occupying the cation sites and Te forming the anionic lattice. A band gap of 0.32 eV allows it to be optimized for power-generation applications and can be doped either *n*- or *p*-type with appropriate dopants. Significant enhancement of the Seebeck coefficient was achieved by introducing resonance level in the valence band of PbTe by doping 2 mol% thallium, resulted doubling of *ZT* to 1.5 at 773 K.[26] Highly doped *p*-type Na doped $PbTe_{1-x}Se_x$ also exhibit high performance thermoelectric properties (ZT~ 1.8 at 850 K) arising from convergence of the multiple valence bands.[27(b)]

Nanoscale inclusions in bulk materials can dramatically suppress the lattice thermal conductivity (κ_{latt}) by scattering the longer wavelength heat-carrying phonons, as shown first time in the case of $AgPb_mSbTe_{m+2}$.[29] In all these cases, however, the power factor ($S^2\sigma$) is also reduced because the nanoinclusions increase carrier scattering which in turn adversely

affects the carrier mobility. Biswas and coworkers have observed that by embedding endotaxial SrTe nanocrystals at concentration as low as 2% in *p*-type bulk PbTe the heat flow can be greatly inhibited without affecting the carrier mobility, thereby allowing a large power factor to be maintained, as shown in figure 1.11.[11] The insensitivity of carrier scattering was attributed to valence band alignment of SrTe and PbTe allowing facile hole transport (Figure 1.11(d)). The crystallographic alignment of SrTe and PbTe lattices and associated strain at

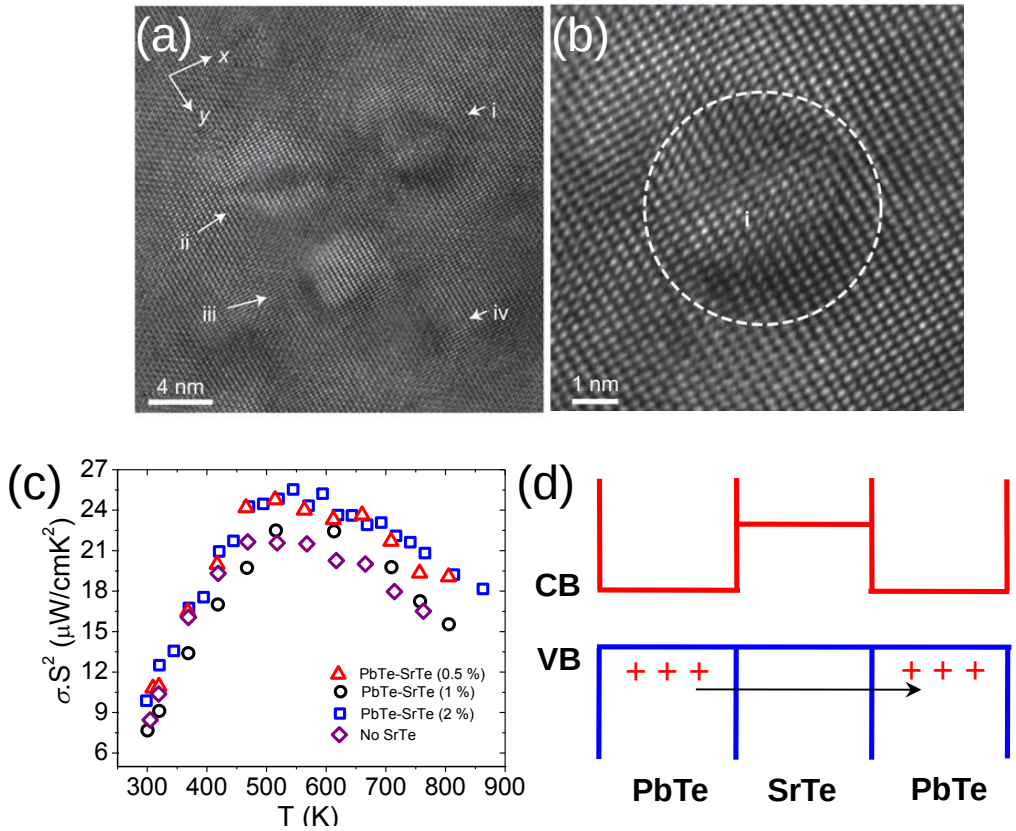

Figure 1.11 (a) High-resolution TEM phase contrast image of several endotaxial nanocrystals of SrTe in the PbTe matrix. Arrows indicate presence of SrTe. (b), Enlarged image of a particle depicting a coherent (with elastic strain) boundary between precipitate and matrix. (c) Power factor (σS^2) of PbTe–SrTe samples doped with 1% Na_2Te and a controlled sample containing no SrTe. (d) Schematic representation of the alignment of the valence band (VB) and conduction band (CB) energies of SrTe precipitates in the PbTe matrix at 300 K. Adapted with permission from ref. 11 *(Nat. Chem.* **2011**, *3*, 160). © 2011 Nature Publishing Group.

interfaces decouples phonon and hole transport leading to a thermoelectric figure of merit of

1.7 at ~ 800 K.[11] Later, similar research has been extended to PbTe-MgTe/CaTe/BaTe (matrix-nanoprecipitate) system, where promising thermoelectric performances have also been achieved.[42] Recently, Biswas and coworkers have demonstrated the substantial suppression of lattice thermal conductivity at high temperature in the PbTe-SrTe system that led to a record high *ZT* of ~2.2 at 915 K in spark plasma sintered-processed samples.[2] This is the result of introducing phonon scattering at all-length scales in a hierarchical fashion from atomic scale doping and endotaxial nanostructuring to mesoscale grain boundary engineering (Figure 1.12). With this new advance in the maximum *ZT*, average ZT_{avg} values of ~1.2 and

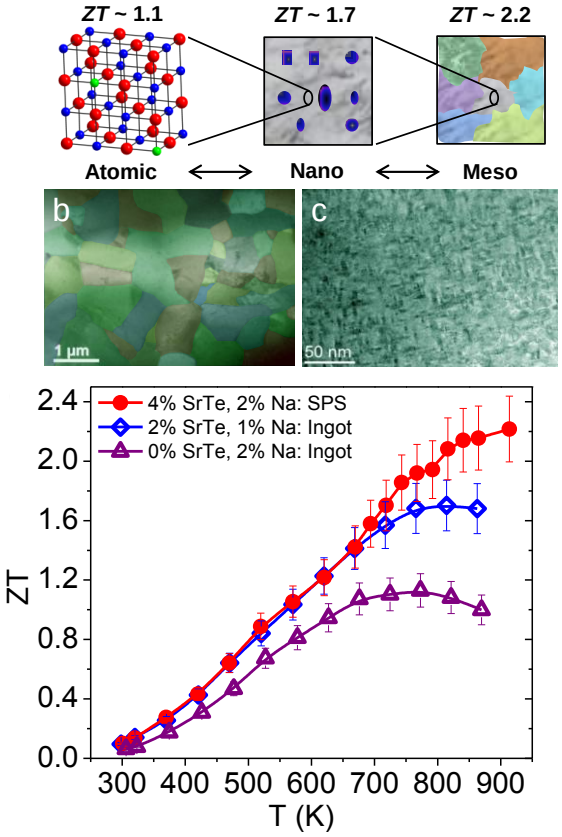

Figure 1.12 (a) Maximum achievable *ZT* values for the respective length scales: the atomic scale (alloy the nanoscale (PbTe matrix, grey; SrTe nanocrystals, blue) to the mesoscale (grain-boundary scattering). (b) TEM images shows the micro and nanostructures in spark-plasma-sintered PbTe–SrTe doped with Na. (c) Temperature dependent *ZT* for an ingot (atomic scale), endotaxial nanostructuted PbTe (atomic plus nanoscale) and spark-plasma-sintered PbTe (atomic + nano + mesoscale). Adapted with permission from ref. 2 (*Nature* 2012, *489*, 414). © 2012 Nature Publishing Group.

~1.7 were obtained for non-segmented and segmented thermoelectric devices respectively (segmentation with BiSbTe, *ZT* ~ 1.2 at 350 K). Considering a cold side temperature of 350 K and hot side 950 K for such devices waste heat conversion efficiencies respectively of ~16.5 and ~20 % were predicted.[2]

1.6.3. Skutterudites

Skutterudites are one of the promising classes of compounds for thermoelectric power generation. They crystallize in the cubic $CoAs_3$-type structure with the space group *Im*-3. The structure is composed of eight corner-shared XY_6 (X=Co, Rh, Ir; Y=P, As, Sb) octahedra. Linked octahedra gives rise to a void at the center of the $(XY_6)_8$ cluster, where the void space occupies a body-centered position of the cubic lattice. This void is large enough to accommodate large metal atoms to form filled skutterudites. Since the void-filling atoms can act as electron donors or acceptors, partially filling the void space of skutterudites can lead to an optimum electron concentration. At the same time, these atoms can also act as strong phonon-scattering centers to greatly reduce the lattice thermal conductivity. The "rattling" effect of these void-filling atoms has resulted in improvements in the thermoelectric properties of skutterudite. High *ZT* values of partially filled skutterudites with a small amount of Ni doping for Co, $Ba_{0.30}Ni_{0.05}Co_{3.95}Sb_{12}$ (*ZT* ~1.25 at 900 K) were reported.[43] Further improvement in the *ZT* was achieved by filling up multiple atom in the void of $CoSb_3$.[44]

1.6.4. Half Heusler compounds

Another class of compounds of considerable interest as potential thermoelectric materials for high-temperature applications are the half-Heusler (HH) compounds denoted as MNiSn (M=Ti, Hf, Zr). HH phases have the MgAgAs crystal structure which consists of three filled interpenetrating face centered cubic lattice sublattices and one vacant sublattice.

The general formula is XYZ, where X and Y are transition metals and Z is a main-group element. Another advantage of these compounds is their high melting points of 1100-1300 °C as well as their chemical stability with essentially zero sublimation at temperatures near 1000 °C. The Heusler intermetallic compounds with fully filled sublattices are metals (full-Heusler alloys), whereas the vacant Ni atom sites in half-Heusler compounds give rise to narrow bands resulting in *d*-orbital hybridization and substantial semiconducting character of the compounds. Sakurada and Shutoh reported a *ZT* value near 1.4 at 700 K for n-type $(Zr_{0.5}Hf_{0.5})_{0.5}Ti_{0.5}NiSn_{1-y}Sb_y$.[45]

1.7. Future outlook

The development of new materials and complex composites over the last 5–10 years has significantly improved the *ZT* values. It has been come from better theoretical understanding, development of new synthesis techniques, and state-of-the-art measurements that the field has progressed so far and promises to move forward further. For a long time it was thought that there was a practical barrier at $ZT = 1$, however new mechanisms for increasing the power factor and reducing the thermal conductivity in thermoelectric materials continue to emerge and increase the *ZT* value. Today, the most recent generation of bulk materials have $ZT \sim 1.6–2.6$ at approximately 700–900 K. To cross this *ZT* value, we need significant enhancement in power factor (σS^2) along with further reductions in the thermal conductivity. Unless this is achieved with an innovation of some new and unexpected single-phase material, which is needed, are new physical concepts on how the power factor can be enhanced 2–4-fold in the existing leading materials. In the following chapters we will focus

on the enhancement of power factor of Pb-free materials for high performance thermoelectrics.

References

1. Source: U.S. Energy Information Administration, International Energy Statics, Indian Central Electricity Authority.
2. Biswas, K.; He, J.; Blum, I. D.; Wu, C. I.; Hogan, T. P.; Seidman, D. N.; Dravid, V. P.; Kanatzidis, M. G. *Nature* **2012**, *489*, 414.
3. Snyder, G. J.; Toberer, E. S. *Nat. Mater.* **2008**, *7*, 105.
4. Rowe, D. M. (ed.) CRC Handbook of & Thermoelectrics (CRC, Boca Raton) **1995**.
5. Sootsman, J.; Chung, D. Y.; Kanatzidis, M. G. *Angew. Chem. Int. Ed.* **2009**, *48*, 8616.
6. Seebeck, A. *Ann. Chim. Phys.* **1826**, *56*, 133.
7. Tritt, T. M.; Subramanian, M. A. *Mater. Res. Soc. Bull.* **2006**, *31*, 188.
8. (a) Altenkirsch, E. *E. Phys. Z.* **1909**, *10*, 560. (b) Altenkirsch, E. *E. Phys. Z.* **1911**, *12*, 920.
9. Chen, G.; Dresselhaus, M. S.; Dresselhaus, G.; Fleurial, J. P.; Caillat, T. *Int. Mater. Rev.* **2003**, *48*, 45.
10. DiSalvo, F. J. *Science* **1999**, *285*, 703.
11. Biswas, K.; He, J.; Zhang, Q.; Wang, G.; Uher, C.; Dravid, V. P.; Kanatzidis, M. G. *Nat. Chem.* **2011**, *3*, 160.
12. Zhao, L. D.; Dravid, V. P.; Kanatzidis, M. G. *Energy Environ. Sci.* **2014**, *7*, 251.
13. Vedernikov, M. V.; Iordanishvili, E. K. *17th Int. Conf. on Thermoelectrics* **1998**, *1*, 37.
14. Chung, D. Y.; Iordanidis, L.; Choi, K. S.; Kanatzidis, M. G. *Bull. Korean Chem. Soc.* **1998**, *19*, 1283.
15. Tritt, T. M. *Ann. Rev. Mater. Res.* **2011**, *41*, 433.

16. Li, J. -F.; Liu, W. -S.; Zhao, L. -D.; Zhou, M. *NPG Asia Mater.* **2010**, *2*, 152.

17. Xie, W.; Weidenkaff, A.; Tang, X.; Zhang, Q.; Poon, J.; Tritt, T. M. *Nanomaterials* **2012**, *2(4)*, 379.

18. Mahan, G. D. *Solid State Physics* **1998**, *51*, 81.

19. Nolas, G. S.; Poon, J.; Kanatzidis, M. G. *Mater. Res. Soc. Bull.* **2006**, *31*, 199.

20. Rowe, D. M. *Renewable Energy* **1999**, *16*, 1251.

21. Sales, B. C. *Mater. Res. Soc. Bull.* **1998**, *23*, 15.

22. Snyder, G. J.; Caillat, T.; Fleurial, J.-P. *Phys. Rev. B* **2000**, *62*, 10185.

23. Mahan, G. D.; Sofo, JO. *Proc. Natl. Acad. Sci. U. S. A.* **1996**, *93*, 7436.

24. Mahan, G. D.; Sales, B; Sharp, J. *Phys. Today* **1997**, *50*, 42.

25. Heremans, J. P.; Wiendlocha, B.; Chamoire, A. M. *Energy Environ. Sci.* **2012**, *5*, 5510.

26. Heremans, J. P.; Jovovic, V.; Toberer, E. S.; Saramat, A.; Kurosaki, K.; Charoenphakdee, A.; Yamanaka, S.; Snyder, G. J. *Science* **2008**, *321*, 554.

27. (a) Pei, Y.; Wang, H.; Snyder, G. J. *Adv. Mater.* **2012**, *24*, 6125. (b) Pei, Y.; Shi, X.; LaLonde, A.; Wang, H.; Chen, L.; Snyder, G. J. *Nature* **2011**, *473*, 66.

28. Kanatzidis, M. G. *Chem. Mater.* **2010,** *22*, 648.

29. Hsu, K. F.; Loo, S.; Guo, F.; Chen, W.; Dyck, J. S.; Uher, C.; Hogan, T.; Polychroniadis, E. K.; Kanatzidis, M. G. *Science* **2004**, *303*, 818.

30. Androulakis, J.; Hsu, K. F.; Pcionek, R.; Kong, H.; Uher, C.; Dangelo, J. J.; Downey, A.; Hogan, T.; Kanatzidis, M. G. *Adv. Mater.* **2006**, *18*, 1170.

31. Poudeu, P. F. P.; D'Angelo, J.; Downey, A. D.; Short, J. L.; Hogan, T. P.; Kanatzidis, M. G. *Angew. Chem. Int. Ed.* **2006**, *45*, 3835.

32. Slack, G. A. In CRC Hand Book of Thermoelectrics; (ed. Rowe, M.) **1995**, 407 (CRC, Boca Raton).

33. Morelli, D. T.; Meisner, G. P.; Chen, B.; Hu, S.; Uher, C. *Phys. Rev. B* **1997**, *56*, 7376.

34. Saramat, A.; Svensson, G.; Palmqvist, A. E. C.; Stiewe, C.; Mueller, E.; Platzek, D.; Williams, S. G. K.; Rowe, D. M.; Bryan, J. D.; Stucky, G. D. *J. Appl. Phys.* **2006**, *99*, 023708.

35. Goldsmid, H. J.; Douglas, R. W. *J. Appl. Phys*. **1954**, 5, 386.

36. (a) Venkatasubramanian , R.; Siivola , E.; Colpitts, V.; O'Quinn, B. *Nature* **2001**, *413*, 597. (b) Zhao, L. -D.; Zhang, B. P.; Liu, W. -S.; Li, J. -F. *J. Appl. Phys.* **2009**, *105*, 023704.

37. Chen, Y.; Nielsen, M. D.; Gao, Y-B.; Zhu, T. J.; Zhao, X.; Heremans, J. P. *Adv. Energy Mater.* **2012**, *2*, 58.

38. Gelbstein, Y.; Davidow, J.; Girard, S. N.; Chung, D. Y.; Kanatzidis, M. G. *Adv. Energy Mater.* **2013**, *3*, 815.

39. Poudel, B.; Hao, Q.; Ma, Y.; Lan, Y.; Minnich, A.; Yu, B.; Yan, X.; Wang, D.; Muto, A.; Vashaee, D.; Chen, X.; Liu, J.; Dresselhaus, M. S.; Chen, G.; Ren, Z. *Science* **2008**, *320*, 634.

40. Mehta, R. J.; Zhang, Y.; Karthik, C.; Singh, B.; Siegel, R. W.; Tasciuc, T. B.; Ramanath, G. *Nat. Mater.* **2012**, *11*, 233.

41. Chung, D. Y.; Hogan, T.; Brazis, P.; Rocci-Lane, M.; Kannewurf, C.; Bastea, M.; Uher, C.; Kanatzidis, M. G. *Science* **2000**, *287*, 1024.

42. (a) Ahn, K.; Han, M. K.; He, J. Q.; Androulakis, J.; Ballikaya, S.; Uher, C.; Dravid, V. P.; Kanatzidis, M. G. *J. Am. Chem. Soc.* **2010**, *132*, 5227. (b) Biswas, K.; He, J. Q.;

Wang, G. Y.; Lo, S. H.; Uher, C.; Dravid, V. P.; Kanatzidis, M. G. *Energy Environ. Sci.* **2011**, *4*, 4675.

43. Tanga, X.; Zhang, Q.; Chen, L.; Goto, T.; Hirai, T. *J. Appl. Phys.* **2005**, *97*, 093712.
44. Shi, X.; Yang, J.; Salvador, J. R.; Chi, M.; Cho, J. Y.; Wang, H.; Bai, S.; Yang, J.; Zhang, W.; Chen, L. *J. Am. Chem. Soc.* **2011**, *133*, 7837.
45. Sakurada, S.; Shutoh, N. *Appl. Phys. Lett.* **2005**, *86*, 082105.
46.

Chapter 2

Lead-free Thermoelectrics: Promising Thermoelectric Performance in *p*-type $SnTe_{1-x}Se_x$ System[†]

Summary: Lead chalcogenides are the best performers for thermoelectric power generation at mid/high temperatures; however, environmental concern about Pb prevents its use in large-scale thermoelectric applications. SnTe, a Pb-free IV-VI narrow band gap semiconductor, has potential to be a good thermoelectric material due to having similar crystal structure and valence band characteristics as PbTe. In this chapter, I have discussed about the promising thermoelectric performance in high quality crystalline ingots of In-doped $SnTe_{1-x}Se_x$ (x = 0-0.15) synthesized by simple vacuum sealed tube melting reaction. First, we have optimized the lattice thermal conductivity of SnTe by solid solution alloying with SnSe. Resonant level formation in the valence band through In doping along with the increase in the contribution of heavy hole valence band through solid solution alloying significantly improved the Seebeck coefficient, resulting in a promising *ZT* of ~0.8 at 860 K in Pb-free *p*-type 1.5 mol% In doped $SnTe_{0.85}Se_{0.15}$ sample.

[†]Paper based on this study has been published in: A. Banik, and K. Biswas, *J. Mater. Chem. A* **2014**, *2*, 9602.

2.1. Introduction

Thermoelectric material can convert waste heat to electrical energy, thus it is expected to play an important role in future energy generation and conversion. The main focus in this field is to develop efficient, stable, environment friendly and inexpensive solid materials.[1-4] The dimensionless thermoelectric figure of merit, ZT, is defined as $ZT = \sigma S^2 T/(\kappa_{lat} + \kappa_{el})$ where σ, S, T, κ_{el} and κ_{lat} are the electrical conductivity, Seebeck coefficient, temperature, electronic thermal conductivity and lattice thermal conductivity, respectively. The recent advances reported in the performance of thermoelectric materials have been achieved mainly through remarkable decrease in the lattice thermal conductivity via phonon scattering by solid solution point defects, second phase nanoprecipitates,[5-7] meso-scale grain boundaries[6-8] and intrinsic bond anharmonicity.[9] However, the κ_{lat} cannot be reduced below amorphous limit as phonon mean free path cannot be smaller than inter atomic distance,[10] but recent reports on Cu_2Se and Cu_2S show that the κ_{lat} could be reduced below amorphous limit in the super ionic phase.[11] Significant improvement of the power factor (σS^2) coupled with low thermal conductivity is necessary to improve the performance of present thermoelectric materials. Approaches to improve the power factor includes enhancement of Seebeck coefficient through the formation of resonant level in the electronic bands[12-14] and convergence of degenerate electronic band valleys through alloying and carrier engineering.[15-18]

Lead chalcogenide and its alloys are the best performers for thermoelectric power generation,[1-3, 5-7, 12, 15] however, environmental concern about Pb prevents its use in large-scale thermoelectric application. Tin telluride (SnTe), a Pb free IV-VI narrow band gap semi-conductor, has the potential to be a good thermoelectric material due to the presence of similar valence band characteristics (light hole and heavy hole valence bands) [19-21] as PbTe. SnTe has

received limited attention because of the inability to control its very high carrier concentration (10^{20}-10^{21} cm^{-3}) which results in low *S* and high κ_{el}.[21] Intrinsic Sn vacancies are responsible for high *p*-type carrier concentration in SnTe.[22] Recently, SnTe has been used to alloy with other metal tellurides such as $AgSbTe_2$ to improve the thermoelectric performance.[23,24] Significant enhancement in the *ZT* of SnTe synthesized by high energy ball milling and spark plasma sintering have been achieved by the increase in Seebeck coefficient due to the formation of resonant level in the valence band through In doping.[14]

In SnTe, energy difference between light hole valence band (*L* band) and heavy hole valence band (Σ band) is ~0.3 eV,[19-21] which is similar to that in PbSe. Earlier investigation based on temperature dependent Hall coefficient measurement of SnTe suggests that the convergence of these two bands occurs at around 700 K.[25] Alloying lead chalcogenide with high band gap alkaline earth chalcogenides (MgTe and SrTe) has been known to decrease the energy difference between *L* and Σ bands to facilitate the convergence with respect to the temperature, thus resulted in improved Seebeck coefficient.[17, 26] Alloying of SnTe (E_g ~0.18 eV) with SnSe, which is a high band gap (E_g ~0.9 eV) semiconductor, may decrease the energy difference of the two valence band of SnTe, thus it will facilitate the convergence. Moreover, thermal conductivity of the SnTe can be further decreased by solid solution alloying with SnSe.

In this chapter, I present the promising thermoelectric performance in Pb-free In-doped $SnTe_{1-x}Se_x$ (x = 0-0.15) system synthesized by simple sealed tube melting reaction. We first optimized the thermal conductivity of SnTe through solid solution alloying with SnSe, then optimized sample was used for further improvement in Seebeck coefficient by In doping. Resonant level formation in the valence bands through In doping along with convergence of

valence bands through solid solution alloying significantly improved the Seebeck coefficient, resulting in a promising *ZT* of ~0.8 at 860 K in 1.5 mol% In doped $SnTe_{0.85}Se_{0.15}$.

2.2. Experimental section

2.2.1. Reagents. Tin (Alfa Aesar 99.99+ %), tellurium (Alfa Aesar 99.999+ %), selenium (Alfa Aesar 99.999+ %) and indium (Alfa Aesar 99.99+ %) were used for synthesis without further purification.

2.2.2. Synthesis. Ingots (~7 g) of $SnTe_{1-x}Se_x$ and pristine SnTe were synthesized by mixing appropriate ratios of high-purity starting materials of Sn, Se and Te in a quartz tube. The tubes were sealed under vacuum (10^{-5} Torr) and slowly heated to 450 ^oC over 12 hrs, then heated up to 900 ^oC in 5 hrs, soaked for 10 hrs, and cooled slowly to room temperature. In doped $SnTe_{1-x}Se_x$ samples were synthesized via similar procedure. Figure 2.1 shows picture of as synthesized sample.

Figure 2.1 Photograph of the as-synthesized ingot. Bar- and coin-shaped samples are used for electrical and thermal transport measurements, respectively.

2.2.3. Powder X-ray diffraction. Powder X-ray diffraction for all of the samples were recorded using a Cu K_α (λ = 1.5406 Å) radiation on a Bruker D8 diffractometer.

2.2.4. Electrical transport. Electrical conductivity and Seebeck coefficients were measured simultaneously under helium atmosphere from room temperature to 873 K on a ULVAC-RIKO ZEM-3 instrument system. The typical sample for measurement had parallelepiped shape with the dimensions of ~2 × 2 × 8 mm^3 as shown in figure 2.1. The longer direction coincides with the direction in which the thermal conductivity was measured.

2.2.5. Hall measurement. Carrier concentrations were determined using Hall coefficient measurements at room temperature with a PPMS system. Four-contact Hall-bar geometry was used for the measurement. At 300 K, we estimated the carrier concentration, *n*, from the formula: $n=1/eR_H$, where *e* is the electronic charge.

2.2.6. Thermal transport. Thermal diffusivity, *D*, was directly measured in the range 300−873 K by using laser flash diffusivity method in a Netzsch LFA-457. Coins with ~8 mm diameter and ~2 mm thickness were used in all of the measurements (Figure 2.1). Temperature dependent heat capacity, C_p, was derived using standard sample (pyroceram) in LFA-457. The total thermal conductivity, κ_{total}, was calculated using the formula, $\kappa_{total} = DC_p\rho$, where ρ is the density of the sample, measured using the sample dimension and mass. The density of the pellets obtained was in the range ~96% of the theoretical density.

2.3. Results and discussion

The designing strategy for improving the thermoelectric performance of SnTe is described below as two rational steps. First, the lattice thermal conductivity of SnTe was optimized by solid solution alloying with SnSe. Moreover, solid solution alloying facilitates valence band convergence in $SnTe_{1-x}Se_x$. Finally, the sample having lowest κ_{lat} has been chosen for further improvement in Seebeck coefficient through In doping.

2.3.1. Solid solution alloying in $SnTe_{1-x}Se_x$: We have synthesized several compositions of $SnTe_{1-x}Se_x$ (x = 0-0.15) by vacuum sealed tube melting reaction. Up to 15 mol% of Se incorporation, solid solution nature was retained in $SnTe_{1-x}Se_x$. Powder X-ray diffraction patterns of the pristine and $SnTe_{1-x}Se_x$ (x = 0.05-0.15) could be indexed on the cubic SnTe structure (*Fm*-3*m* space group) with no other second phase within the detection limits of powder XRD (Figure 2.2). The observed linear contraction in the lattice parameter in $SnTe_{1-x}Se_x$ (x = 0-0.15) and higher angle shift of PXRD peak (Figure 2.3) with increasing Se concentrations indicate the solid solution behavior. Ionic radius of Se (184 pm) is smaller than that of Te (207 pm). As smaller Se is introduced in the place of bigger Te, the unit cell undergoes a systematic contraction, leading

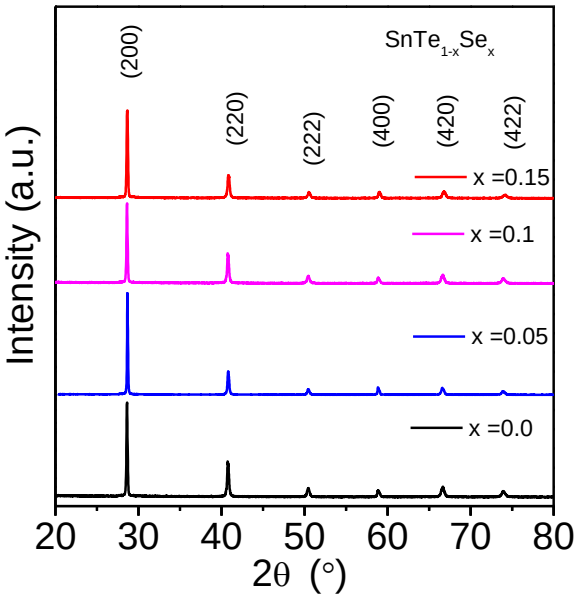

Figure 2.2 Powder XRD pattern of $SnTe_{1-x}Se_x$.

to decrease in the lattice parameter (Figure 2.3a). This gradual decrease of lattice parameter indicates an isomorphic substitution of bigger Te position by smaller Se.

Temperature dependent electrical conductivity (σ) and Seebeck coefficient (S) of $SnTe_{1-x}Se_x$ (x = 0-0.15) are presented in figure 2.4. Temperature dependence of σ confirms degenerate

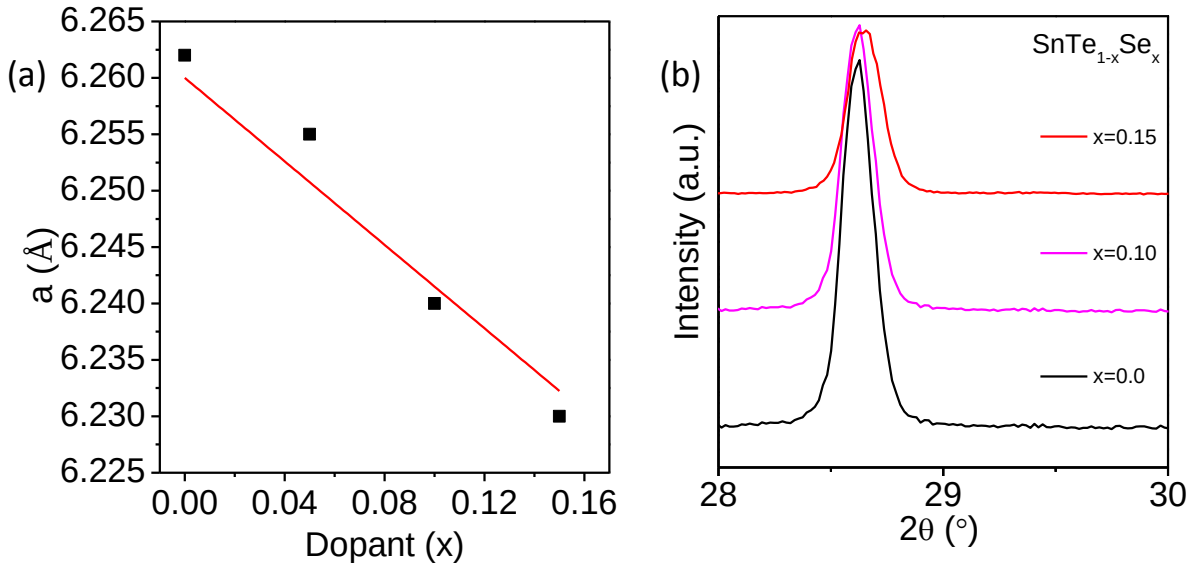

Figure 2.3 (a) Lattice parameter (*a*) vs. Se concentration (*x*) in $SnTe_{1-x}Se_x$ and red line indicates the Vegard's law for solid solution, and (b) higher angle shift of powder XRD pattern upon solid solution alloying.

semiconducting nature of $SnTe_{1-x}Se_x$ samples. Electrical conductivity decreases with increasing Se concentration. The electrical thermal conductivities, $\kappa_{el} = L \cdot \sigma \cdot T$, were extracted based on

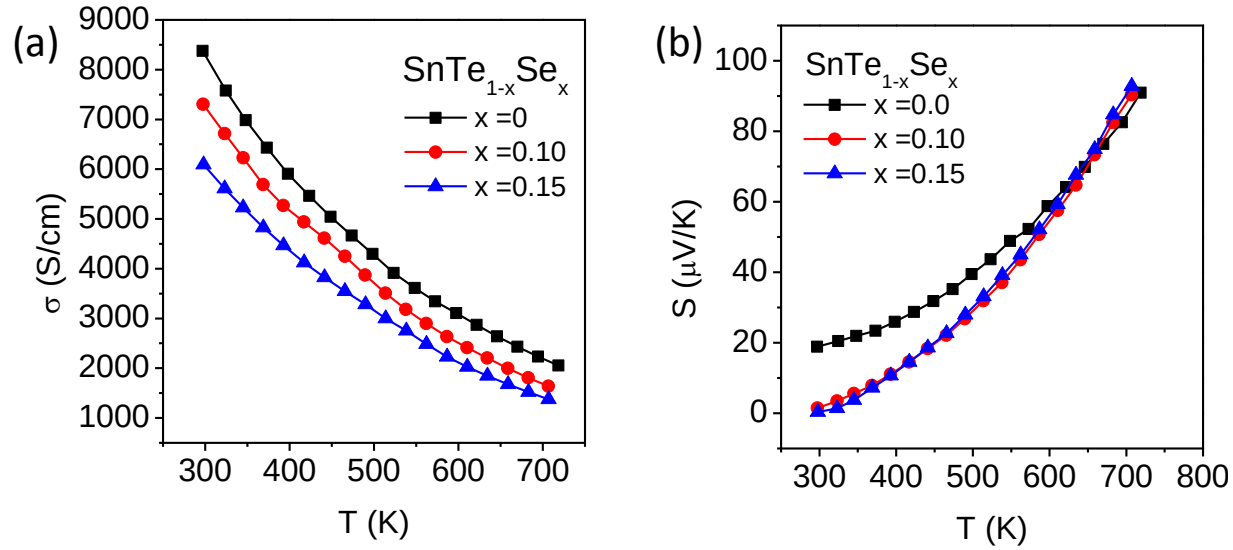

Figure 2.4 Temperature dependent (a) electrical conductivity (σ) and (b) Seebeck coefficient (*S*) of $SnTe_{1-x}Se_x$.

fitting of the respective Seebeck values (Figure 2.4 (b)) that estimate the reduced chemical potential from which the Lorenz number, *L*, can be obtained as explained in reference.[27]

In figure 2.5, temperature dependent thermal transport properties are presented. Fig 2.5 (a) and (c) show temperature dependence of thermal diffusivity (D) and total thermal conductivity (κ_{total}). Significant decrease in diffusivity (D) and thermal conductivity (κ_{total}) was observed with increasing Se concentration of $SnTe_{1-x}Se_x$ (x = 0-0.15) samples. In figure 2.5 (b), we have presented temperature dependent heat capacity (C_p) for $SnTe_{1-x}Se_x$. The κ_{lat} was

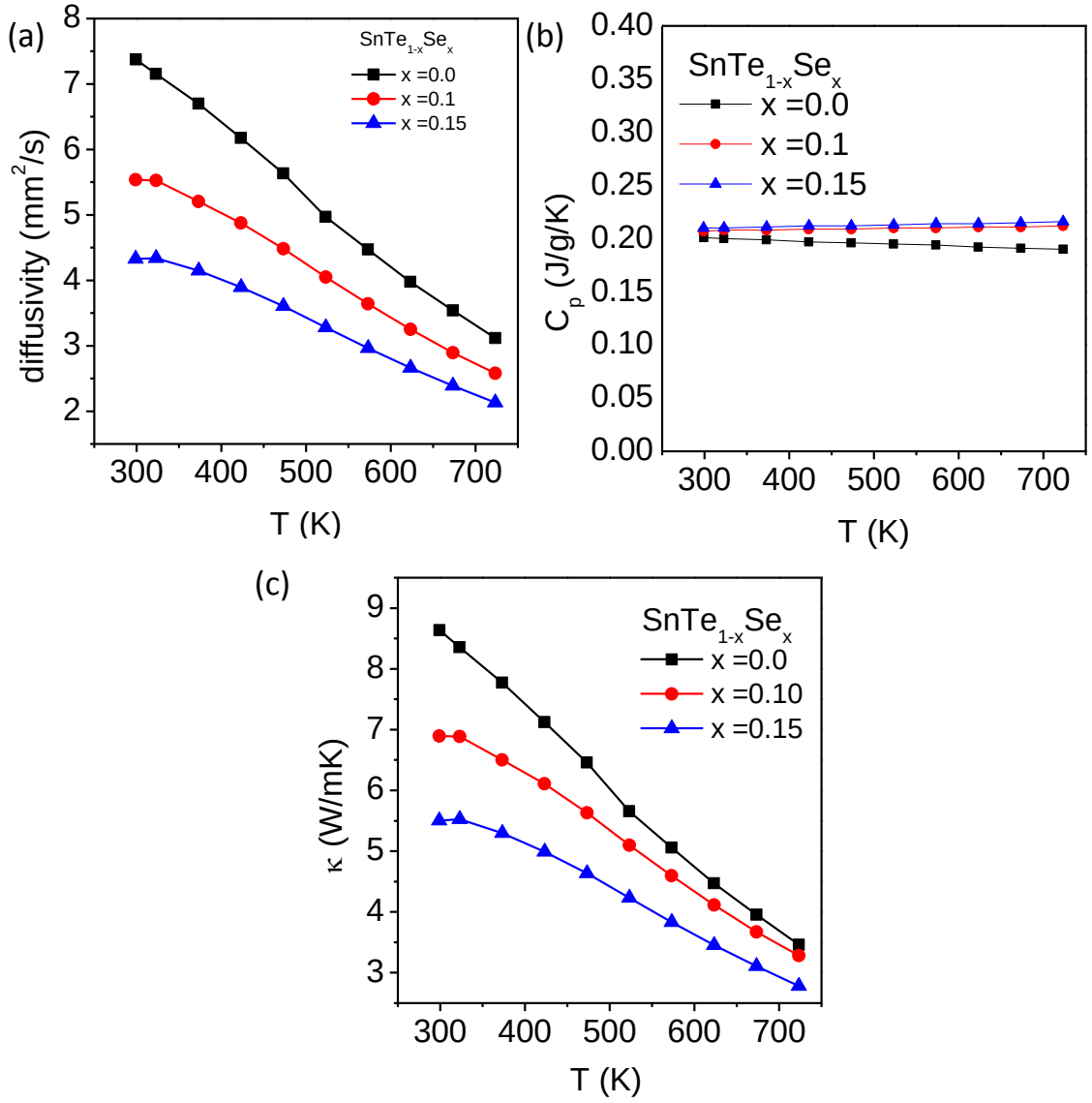

Figure 2.5 Temperature dependent (a) diffusivity (D), (b) specific heat (C_p) and (c) total thermal conductivity (κ_{total}) of $SnTe_{1-x}Se_x$.

obtained after subtracting the electronic part, κ_{el}, from the κ_{total}. Significant decrease of κ_{lat} have been achieved in $SnTe_{1-x}Se_x$ (x = 0.5-0.15) samples compared to that of pristine SnTe (Figure 2.6), which is due to the excess phonon scattering by the solid solution point defects formation and mass fluctuation. 15 mol% Se incorporated $SnTe_{1-x}Se_x$ has lowest κ_{lat}, hence $SnTe_{0.85}Se_{0.15}$ sample has been used for further investigation. Typically, $SnTe_{0.85}Se_{0.15}$ sample has κ_{lat} of ~1.27 $Wm^{-1}K^{-1}$ at 300 K, then it passes through a minima (~0.7 $Wm^{-1}K^{-1}$) at 535 K and reaches to ~0.94 $Wm^{-1}K^{-1}$ at 710 K (Figure 2.6).

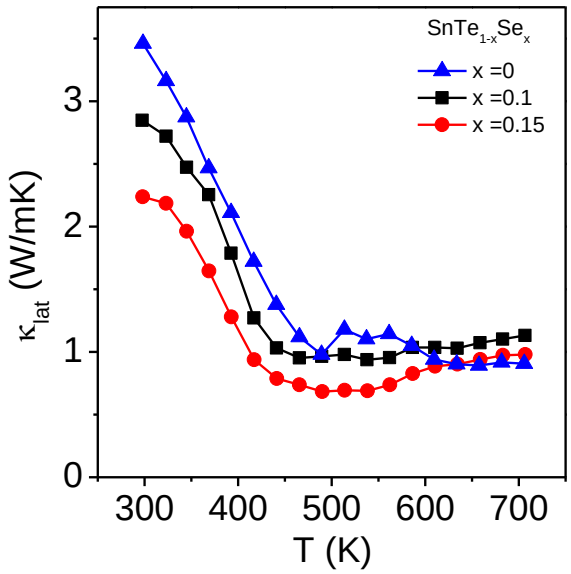

Figure 2.6 Temperature dependent lattice thermal conductivity (κ_{lat}) of $SnTe_{1-x}Se_x$.

We could not able to resolve the band gap (E_g) of the $SnTe_{1-x}Se_x$ (x = 0-0.15) samples by diffuse IR reflectance spectroscopy as the present samples are highly self doped (carriers ~10^{20} cm^{-3}) due to intrinsic Sn vacancy. Systematic increase in the E_g have been observed earlier in thin film samples of $SnTe_{1-x}Se_x$ with low carrier concentration.[28] If the energy of *L* (light hole) valence band reduced as the band gap increases, which reduces the band offset between *L* and Σ valence bands in SnTe, the heavy hole Σ band will play a significant role to increase in Seebeck in properly doped $SnTe_{0.85}Se_{0.15}$ sample. Similar decrease in the energy difference between *L* and

Σ valence bands in lead chacogenides have been achieved when alloyed with high band gap alkaline earth (Mg/Sr) chalcogenides.[17, 26]

2.3.2. In doping in $SnTe_{1-x}Se_x$: We have synthesized several In (0-2.5 mol%) doped $SnTe_{0.85}Se_{0.15}$ by similar sealed tube melting reaction. Powder X-ray diffraction patterns of the In -doped $SnTe_{0.85}Se_{0.15}$ could be indexed on the cubic SnTe structure (F*m*-3*m* space group) with no other impurity phase within the detection limits of powder XRD (Figure 2.7).

Electrical conductivity (σ) decreases with increasing In concentration up to 2.5 mol%, especially at room temperature from 6110 Scm^{-1} to 1240 Scm^{-1} (Figure 2.8). Typically, the room temperature σ of 1.5 mol% In doped $SnTe_{0.85}Se_{0.15}$ is 1670 Scm^{-1}, which decreases to 640 Scm^{-1} at 855 K, showing a typical degenerate semiconductor behavior. The room temperature

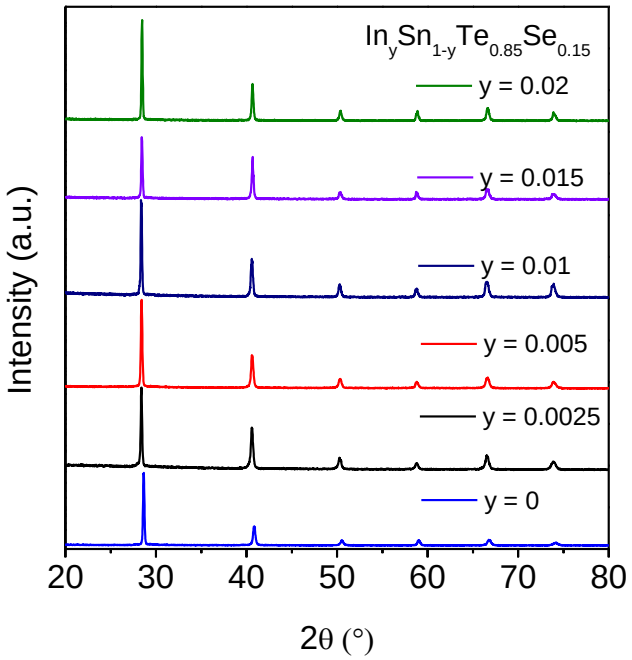

Figure 2.7 Powder XRD pattern of $In_ySn_{1-y}Te_{0.85}Se_{0.15}$.

Hall coefficients, R_H, of all In doped $SnTe_{0.85}Se_{0.15}$ samples are positive, which indicates the *p*-type conduction in this system. Carrier concentration (*n*) at 300 K increases with increasing the

In doping concentration up to 1 mol% and then decreases with further increasing In doping up to 2 mol% (Figure 2.8 (b)). Indium in IV-VI semiconductors have known to exhibit anomalous behavior, In can act both as *n*-type and *p*-type dopant in IV-VI semiconductor material.[13] In the present case, first, In substitutes the Sn in $SnTe_{0.85}Se_{0.15}$ and acts as acceptor, thus *p*-type carrier concentration increases. When the In concentration reaches beyond 1 mol%, extra In atom acts as donors, which decreases the hole carrier concentration in $SnTe_{0.85}Se_{0.15}$.[14] Similar mixed *p* and *n*-type doping behaviour of In in SnTe have been observed in recently reported In doped SnTe samples.[14] Room temperature hole mobility, defined as $\mu = \sigma/ne$, for various In doped $SnTe_{0.85}Se_{0.15}$ samples is plotted in Figure 2.8 (c). Decrease in room temperature σ value with the

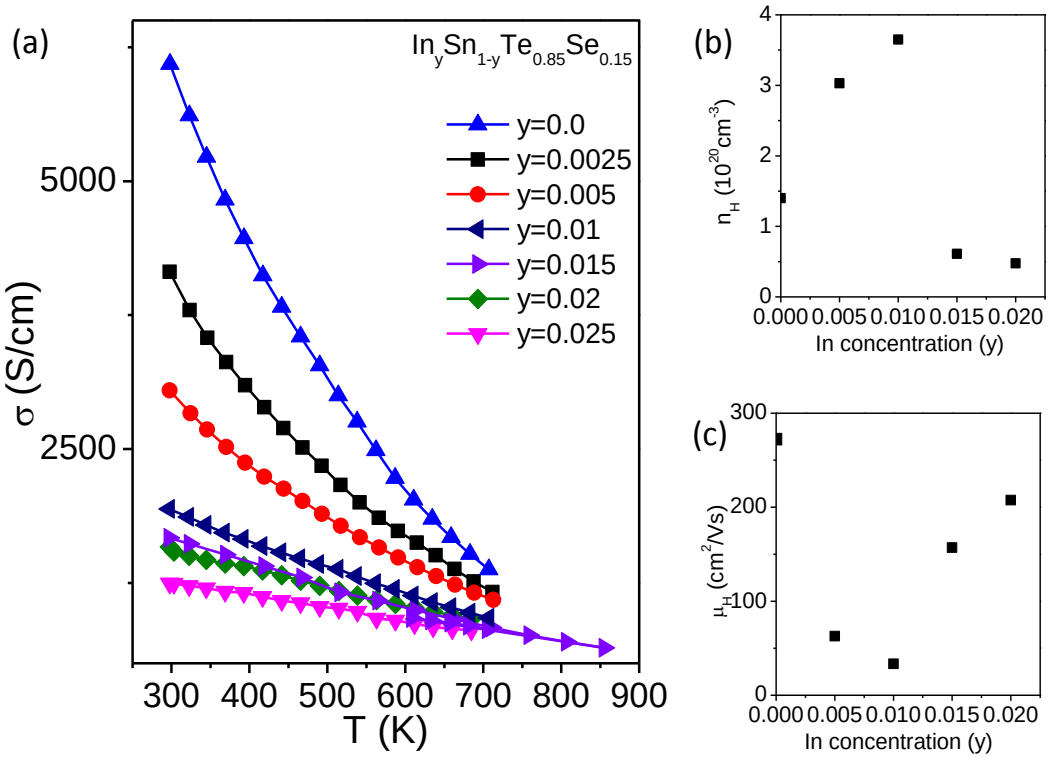

Figure 2.8 (a) Temperature dependent electrical conductivity (σ), (b) carrier concentration (n) and (c) carrier mobility (μ) at room temperature with dopant concentration y of $In_ySn_{1-y}Te_{1-x}Se_x$.

increase in In doping concentration is due to the significant decrease in μ. Carrier mobility decreases in In (< 1 mol%) doped $SnTe_{0.85}Se_{0.15}$ due to impurity scattering.[14]

Figure 2.9 (a) presents the temperature dependent Seebeck coefficient (*S*) data of In (0-2.5 mol%) doped $SnTe_{0.85}Se_{0.15}$ samples. Positive value of *S* indicates the *p*-type carriers which supports the Hall measurement. Significant improvement in the *S* have been achieved by In doping in $SnTe_{0.85}Se_{0.15}$, especially at room temperature from ~0.5 μVK^{-1} to ~70 μVK^{-1} with a In doping concentration of 2 mol%. Typically, the room temperature *S* value measured for 1.5 mol% In doped $SnTe_{0.85}Se_{0.15}$ was ~ 67 μVK^{-1} which linearly increases to ~175 μVK^{-1} at 855 K. In figure 2.9 (b), we compare the present room temperature *S* vs. *n* data with previously reported experimental data on In doped SnTe (ball mill + SPS samples),[14] Cu doped SnTe [21] and

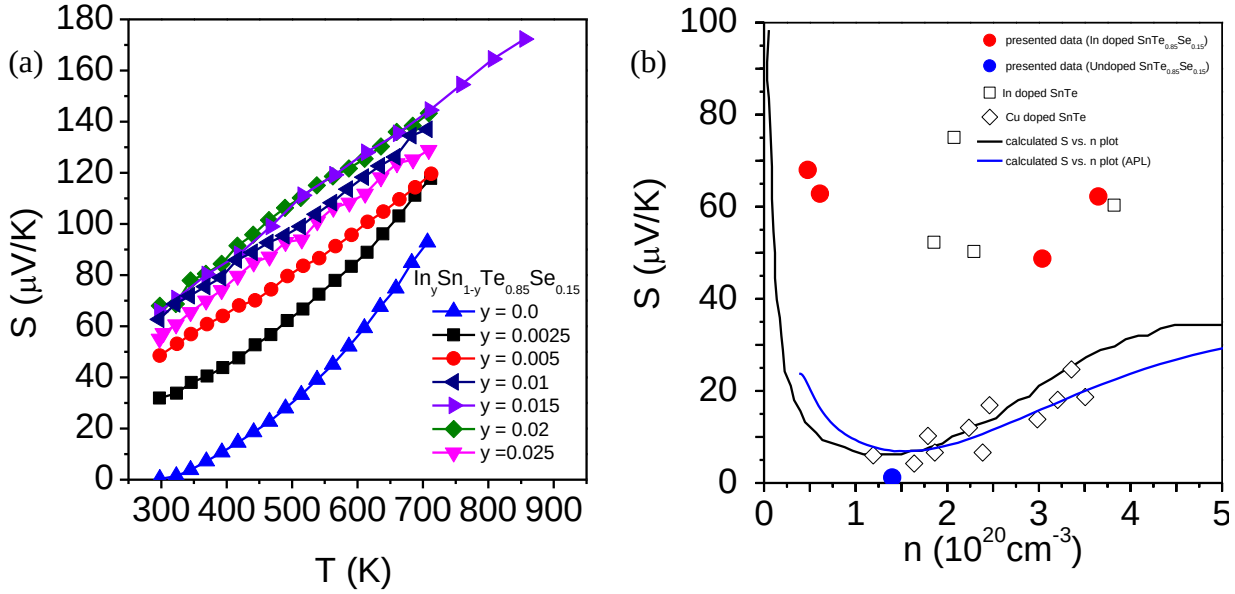

Figure 2.9 Temperature dependent Seebeck coefficient, (b) Room temperature Seebeck vs. carrier concentration plot of $In_ySn_{1-y}Te_{0.85}Se_{0.15}$ in comparison with reported data on In doped SnTe (□),[14] Cu doped SnTe (◇).[21] The solid bands are based on VBM model.

also with the earlier reported theoretical *S* vs. *n* curves.[14, 19] Theoretical Pisarenko (*S* vs. *n*) curves at room temperature have been calculated earlier by considering the contribution of both the light

hole valence band (*L* point) and heavy hole valence band (*Σ* point).[14] Significant enhancement in the present *S* values compared to the theoretical Pisarenko plots have been noticed, thus it indicates the creation of resonant level in the valence band of $SnTe_{0.85}Se_{0.15}$ by In doping. Room temperature *S* values of undoped and Cu-doped samples agree well with the Pisarenko curves.

Figure 2.10 presents the temperature dependent power factor (σS^2) data of In (0-2.5 mol%) doped $SnTe_{0.85}Se_{0.15}$ samples. Significant improvement in σS^2 has been achieved mainly due to the enhancement of the thermopower in the sample. Typically, at room temperature, σS^2 value for 1.5 mol% In doped $SnTe_{0.85}Se_{0.15}$ is ~7.3 μWcm $^{-1}K^{-2}$ which rises almost linearly to

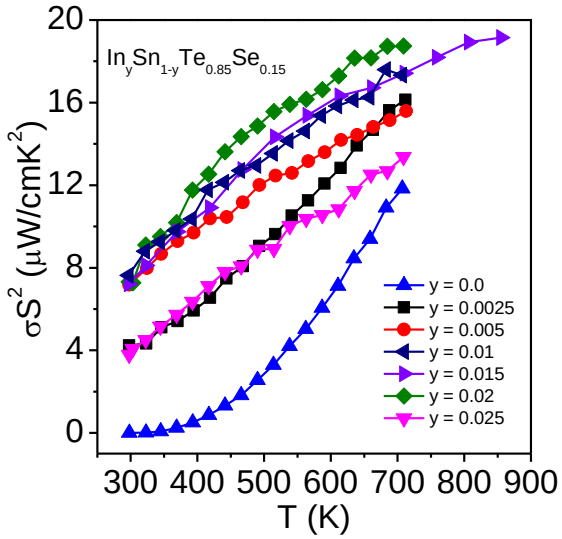

Figure 2.10 Temperature dependent power factor (σS^2) of $In_ySn_{1-y}Te_{0.85}Se_{0.15}$.

~19.2 μW cm$^{-1}K^{-2}$ at ~855 K. Enhancement of σS^2 have been observed due to the resonance level effect and also due to contribution of heavy hole valence band especially at high temperature in In doped $SnTe_{1-x}Se_x$.

In figure 2.11, we have presented thermal diffusivity (*D*) and specific heat (C_p) of $In_ySn_{1-y}Te_{0.85}Se_{0.15}$ (y = 0-0.02). Indium doping in $SnTe_{0.85}Se_{0.15}$ optimizes the temperature dependent κ_{total} (Figure 2.12) by controlling the $\kappa_{el.}$ Typically, the room temperature κ_{total} value measured

for 1.5 mol% In doped $SnTe_{0.85}Se_{0.15}$ is ~2.3 $Wm^{-1}K^{-1}$ which decreases to ~2.15 $Wm^{-1}K^{-1}$ at 873 K. The $\kappa_{el} = L \cdot \sigma \cdot T$, were extracted based on fitting of the respective Seebeck values to estimate

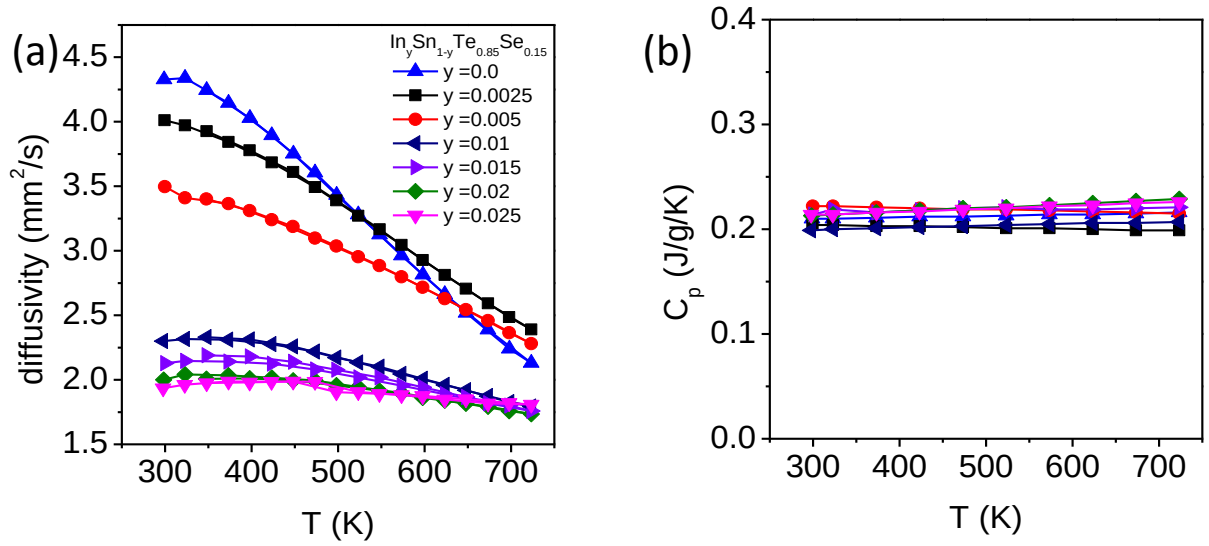

Figure 2.11 Temperature dependence of thermal diffusivity (D) and specific heat (C_p) of $In_ySn_{1-y}Te_{1-x}Se_x$.

the reduced chemical potential (η) from which the Lorenz number, L, can be obtained as explained in detail elsewhere (figure 2.13).[27] With In doping temperature dependent κ_{el}

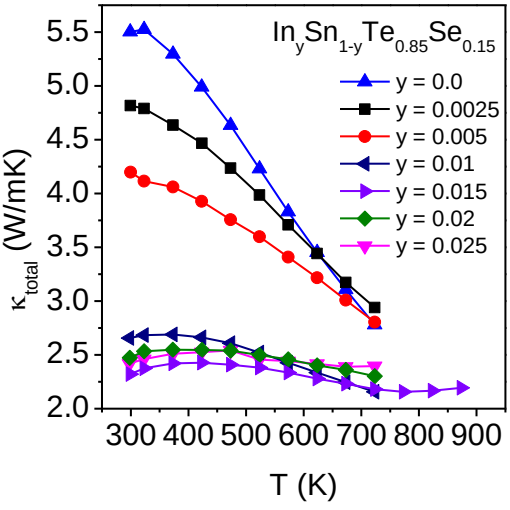

Figure 2.12 Temperature dependent total thermal conductivity (κ_{total}) of $In_ySn_{1-y}Te_{1-x}Se_x$.

decreases significantly due to the decrease in the temperature dependent σ (Figure 2.14). The

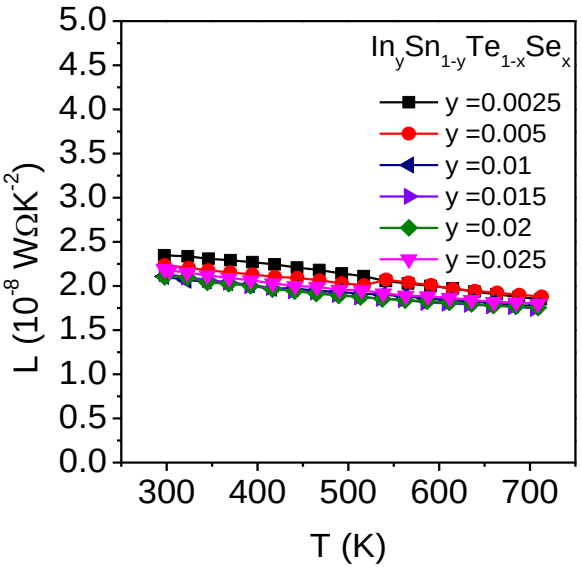

Figure 2.13 Temperature dependent Lorenz number (L) of $In_ySn_{1-y}Te_{0.85}Se_{0.15}$.

lattice thermal conductivity, κ_{lat}, was estimated after subtracting the electronic part, κ_{el}, from the

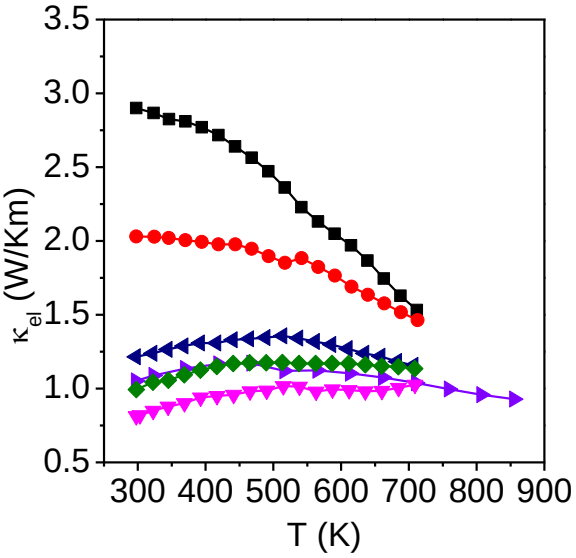

Figure 2.14 Temperature dependent electronic thermal conductivity (κ_{el}) of $In_ySn_{1-y}Te_{1-x}Se_x$.

κ_{total} (Figure 2.15). κ_{lat} decreases with increasing temperature for $In_ySn_{1-y}Te_{0.85}Se_{0.15}$ samples.

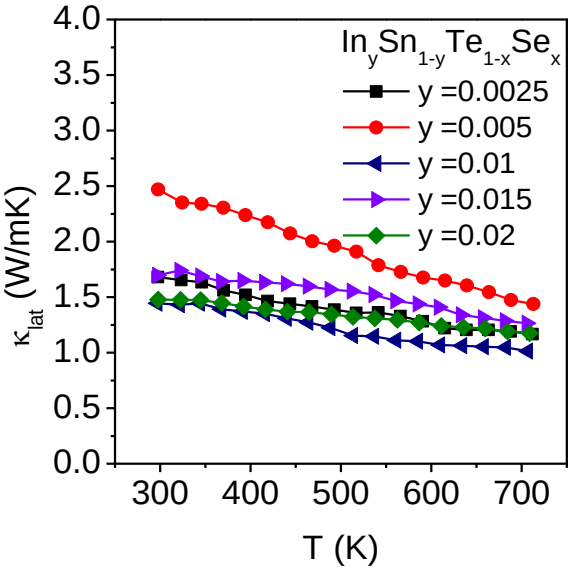

Figure 2.15 Temperature dependent lattice thermal conductivity (κ_{lat}) of $In_ySn_{1-y}Te_{0.85}Se_{0.15}$.

In Figure 2.16 we present temperature dependent *ZT*s of all In doped $SnTe_{0.85}Se_{0.15}$. The highest *ZT* value of ~0.8 at 855 K was achieved for 1.5 mol% In doped $SnTe_{0.85}Se_{0.15}$, which is significantly higher compared to undoped SnTe and $SnTe_{0.85}Se_{0.15}$ samples.

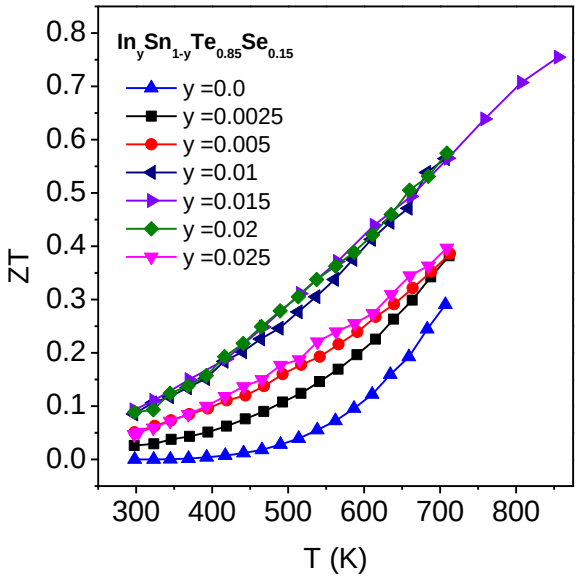

Figure 2.16 Temperature dependent figure of merit of $In_ySn_{1-y}Te_{0.85}Se_{0.15}$.

To check reversibility, measurements were done both for heating and cooling cycle. For all the samples both the heating and cooling cycle gave repeatable data.

2.4. Conclusions

High quality crystalline ingots of In-doped $SnTe_{1-x}Se_x$ (x = 0-0.15) have been synthesized by simple vacuum sealed tube melting reaction. First, the lattice thermal conductivity of SnTe has been minimized by solid solution alloying with SnSe. Resonant level formation in the valence band through In doping along with convergence of valence band through solid solution alloying significantly improve the Seebeck coefficient in In doped $SnTe_{1-x}Se_x$, resulting in a enhanced power factor. Improved power factor with relatively low thermal conductivity have resulted a *ZT* of ~0.8 in Pb-free $SnTe_{1-x}Se_x$ system. Further improvement in the thermoelectric performance of $SnTe_{1-x}Se_x$ can be achieved through reduction of the thermal conductivity further by second phase nanostructuring and all-scale hierarchical phonon scattering.

References

1. Sootsman, J.; Chung, D. Y.; Kanatzidis, M. G. *Angew. Chem. Int. Ed.* **2009**, *48*, 8616.
2. Zhao, L. -D.; Dravid, V. P.; Kanatzidis, M. G. *Energy Environ. Sci.* **2014**, *7*, 251.
3. Snyder, G. J.; Toberer, E. S. *Nat. Mater.* **2008**, *7*, 105.
4. (a) Zebarjadi, M.; Esfarjani, K.; Dresselhaus, M. S.; Ren, Z. F.; Chen, G. *Energy Environ. Sci.* **2012**, *5*, 5147; (b) Zhang, Y.; Stucky, G. D. *Chem. Mater.* **2014**, *26*, 837.
5. Biswas, K.; He, J.; Zhang, Q.; Wang, G.; Uher, C.; Dravid, V. P.; Kanatzidis, M. G. *Nat. Chem.* **2011**, *3*, 160.
6. Biswas, K.; He, J.; Blum, I. D.; Wu, C. I.; Hogan, T. P.; Seidman, D. N.; Dravid, V. P.; Kanatzidis, M. G. *Nature* **2012**, *489*, 414.
7. Zhao, L. -D.; Hao, S.; Lo, S. -H.; Wu, C. -I.; Zhou, X.; Lee, Y.; Li, H.; Biswas, K.; Hogan, T. P.; Uher, C.; Wolverton, C.; Dravid, V. P.; Kanatzidis, M. G. *J. Am. Chem. Soc.* **2013,** *135*, 7364.
8. Poudel, B.; Hao, Q.; Ma, Y.; Lan, Y.; Minnich, A.; Yu, B.; Yan, X.; Wang, D.; Muto, A.; Vashee, D.; Chen, X.; Liu, J.; Dresselhaus, M. S.; Chen, G.; Ren, Z. *Science* **2008**, *320*, 634.
9. Morelli, D. T.; Jovovic, V.; Heremans, J. P. *Phys. Rev. Lett.* **2008**, *101*, 035901.
10. Slack, G.A. *Solid State Physics* **197**9, *34*, 1.
11. (a) Liu, H.; Shi, X.; Xu, F.; Zhang, L.; Zhang, W.; Chen, L.; Li, Q.; Uher, C.; Day, T.; Snyder, G. J. *Nat. Mater.* **2012**, *11*, 422. (b) He, Y.; Day, T.; Zhang, T.; Liu, H.; Shi, X.; Chen, L.; Snyder, G. J. *Adv. Mater.* **2014**, *26*, 3974.
12. (a) Heremans, J. P.; Jovovic, V.; Toberer, E. S.; Saramat, A.; Kurosaki, K.; Charoenphakdee, A.; Yamanaka, S.; Snyder, G. J. *Science* **2008**, *321*, 554. (b) Heremans, J. P.; Wiendlocha, B.; Chamoire, A. M. *Energy Environ. Sci.* **2011**, *5*, 5510.
13. Ahmad, S.; Hoang, K.; Mahanti, S. D. *Phys. Rev. Lett.* **2006**, *96*, 56403.
14. Zhang, Q.; Liao, B.; Lan, Y.; Lukas, K.; Liu, W.; Esfarjani, K.; Opeil, C.; Broido, D.; Chen, G. ; Ren, Z. *Proc. Natl. Acad. Sci. U. S. A.* **2013**, *110*, 13261.
15. (a) Pei, Y.; Shi, X.; LaLonde, A.; Wang, H.; Chen, L.; Snyder, G. J. *Nature* **2011**, *473*, 66. (b) Pei, Y.; Wang, H.; Snyder, G. J. *Adv. Mater.* **2012**, *24***,** 6125.

16. Liu, W.; Tan, X.; Yin, K.; Liu, H.; Tang, X.; Shi, J.; Zhang, Q.; Uher, C. *Phys. Rev. Lett.* **2012**, *108*, 166601.
17. Zhao, L. D.; Wu, H. J.; Hao, S. Q.; Wu, C. I.; Zhou, X. Y.; Biswas, K.; He, J. Q.; Hogan, T. P.; Uher, C.; Wolverton, C.; Dravid, V. P.; Kanatzidis, M. G. *Energy Environ. Sci.* **2013**, *6*, 3346.
18. Guin, S. N.; Chatterjee, A.; Negi, D. S.; Datta, R.; Biswas, K. *Energy Environ. Sci.* **2013**, *6*, 2603.
19. Rogers, L. M. *J. Phys. D Appl. Phys.* **1968**, *1*, 845.
20. Efimova, B. A.; Kaidanov, V. I.; Moizhes, B. Y.; Chernik, I. A. *Sov. Phys. - Sol. Stat.* **1966**, *7*, 2032.
21. Brebrick, R. F.; Strauss, A. J. *Phys. Rev.* **1963**, *131*, 104.
22. Brebrick, R. F. *J. Phys. Chem. Solids* **1963**, *24*, 27.
23. Han, M. K.; Androulakis, J.; Kim, S. J.; Kanatzidis, M. G. *Adv. Energy Mater.* **2012**, *2*, 157.
24. Chen, Y.; Nielsen, M. D.; Gao, Y-B.; Zhu, T. J.; Zhao, X.; Heremans, J. P. *Adv. Energy Mater.* **2012**, *2*, 58.
25. Andreev, A. A. *Sov. Phys. - Sol. Stat.* **1967**, *9*, 1232.
26. Wang, H.; Gibbs, Z. M.; Takagiwa, Y.; Snyder, G. J. *Energy Environ. Sci.* **2014**, *7*, 804.
27. Zhao, L.-D.; Lo, S.-H.; He, J.; Li, H.; Biswas, K.; Androulakis, J.; Wu, C.-I.; Hogan, T. P.; Chung, D. Y.; Dravid, V. P.; Todorov, I.; Chung, D. Y.; Kanatzidis, M. G. *J. Am. Chem. Soc.* **2011**, *133*, 20476.
28. Soliman, L. I.; Farag, B. S.; Zayed, H. A.; Shehata, F. M. *Ind. J. Pure Appl. Phys.* **2003**, *41*, 131.

Chapter 3

Mg Alloying in SnTe Facilitates Valence Band Convergence and Optimizes Thermoelectric Properties†

Summary: SnTe, a lead-free rock-salt analogue of PbTe, having valence band structure similar to PbTe, recently has attracted attention for thermoelectric heat to electricity generation. However, pristine SnTe is a poor thermoelectric material because of very high hole concentration resulting from intrinsic Sn vacancies, which give rise to low Seebeck coefficient and high electrical thermal conductivity. In this chapter, we show that SnTe can be optimized to be a high performance thermoelectric material for power generation by controlling the hole concentration and significantly improving the Seebeck coefficient. Mg (2-10 mol%) alloying in SnTe modulates its electronic band structure by increasing the band gap of SnTe, and results in decrease in the energy separation between its light and heavy hole valence bands. Thus, solid solution alloying with Mg enhances the contribution of heavy hole valence band, leading to significant improvement in the Seebeck coefficient in Mg alloyed SnTe, which in turn results in remarkable enhancement in power factor. Maximum thermoelectric figure of merit, *ZT*, of ~1.2 is achieved at 860 K in high quality crystalline ingot of *p*-type $Sn_{0.94}Mg_{0.09}Te$.

†Paper based on this chapter has been published in: A. Banik, U. S. Shenoy, S. Anand, U. V. Waghmare and K. Biswas, *Chem. Mater.* **2015**, *27*, 581.

3.1. Introduction

A thermoelectric material can directly convert temperature difference to electrical voltage, thus can play an important role in generation of electrical energy from waste heat.[1-4] Materials in this field require a high value of dimensionless thermoelectric figure of merit, $ZT = \sigma S^2 T / (\kappa_{lat} + \kappa_{el})$, where σ is electrical conductivity, S is Seebeck coefficient, κ_{lat} is lattice thermal conductivity, κ_{el} is electronic thermal conductivity, and T is temperature. Significant improvement in the ZT have been achieved through the reduction of κ_{lat} via phonon scattering by the solid solution point defects, second phase nanoprecipitates,[5-7] meso-scale grain boundaries [6-8] and intrinsic bond anharmonicity.[9, 10] Enhancement of Seebeck coefficient also resulted in high ZTs either through the formation of resonance level in the electronic bands[11-13] or convergence of degenerate electronic band valleys by alloying and carrier engineering.[14-17]

Lead telluride (PbTe) and its alloys are considered to be some of the best thermoelectric materials for mid temperature power generation application.[1-3, 5-7, 11, 14] Solid solution alloying and second phase nanostructuring with group-II (Mg, Ca, Sr and Ba) alkaline earth telluride have significant effect on thermoelectric property of PbTe.[5, 6, 16, 18-20] Mention must be made that alloying of MgTe (band gap ~3.5 eV) increases the band gap of PbTe, resulting in decrease in the energy separation between the light (L point) and heavy (Σ point) valence bands to accomplish more controllable band convergence with respect to temperature.[16, 19, 20] Thus, a significant enhancement in Seebeck coefficient was obtained. However, environmental concern about Pb limits its use in large scale thermoelectric applications. Tin telluride (SnTe), a homolog of PbTe, has the potential to be a good thermoelectric material due to its valence band (light hole and heavy hole valence bands)

characteristic that is similar to PbTe.[21-23] SnTe has rarely been considered to be efficient thermoelectric material because of the inability to control its very high carrier concentration (10^{20}-10^{21} cm^{-3}) which results in low S and high κ_{el}.[23] Intrinsic Sn vacancy is responsible for high p-type carrier concentration in SnTe.[24] Recently, SnTe has been alloyed with other metal telluride such as $AgSbTe_2$ to improve its thermoelectric performance.[25, 26] Significant enhancement in the Seebeck coefficient of SnTe has been achieved due to the formation of resonance level in the valence band through In doping, which resulted a ZT of ~1.1 at 873 K.[13] Carrier concentration in the light hole valence band of SnTe was effectively tuned by iodine doping, which essentially tunes the thermoelectric properties of SnTe.[27]

In SnTe, valence band and conduction band edges are located at the L-point of Brillouin zone and the energy gap is ~0.15 eV at room temperature.[21] Interestingly, a heavy hole valence band (Σ band) lies ~0.35 eV below the light hole valence band (L band).[21-23] Earlier investigation based on temperature dependent Hall coefficient (R_H) measurement of SnTe suggested that the convergence of these two bands occurs at around 700 K.[28] Large energy separation between light and heavy hole valence bands restricts the contribution of heavy hole mass to the Seebeck coefficient. Enhancement in the Seebeck coefficient has been achieved by Cd or Hg alloying in SnTe, which decreases the energy separation between light and heavy hole valence band.[29] Solid solution alloying of SnTe with SnSe followed by In doping also improves the Seebeck coefficient due to resonance level formation in the valence band.[30] Alloying of SnTe (E_g ~0.15 eV) with MgTe, which is a wide band gap (E_g ~3.5 eV) semiconductor, may open up the band gap of SnTe, which can decrease the energy difference of the two valence bands of SnTe, thus it will facilitate the convergence of the valence band valleys.

Here, I present effects of Mg alloying on the electronic structure and the thermoelectric properties of SnTe which is synthesized by simple sealed tube melting reactions. We first suppress the excess hole concentration of SnTe by Sn-self compensation ($Sn_{1.03}Te$).[29] Mg alloying in $Sn_{1.03}Te$ samples increases the band gap, with direct evidence from the infrared diffuse reflectance spectroscopy and electronic structure calculations. Moreover, Mg alloying significantly tunes the electronic band structure of SnTe, which essentially decreases energy difference between the light hole and heavy hole valence bands, leading to an enhanced Seebeck coefficient. As a result, *p*-type $Sn_{0.94}Mg_{0.09}Te$ sample exhibits a maximum *ZT* of ~1.2 at ~860 K. These findings make SnTe-based materials an important contender for thermoelectric power generation and should stimulate further investigation and optimization.

3.2. Experimental and computational sections

3.2.1. Reagents. Tin (Alfa Aesar 99.99+ %), tellurium (Alfa Aesar 99.999+ %), and magnesium powder (Alfa Aesar 99.999+ %) were used for synthesis without further purification.

3.2.2. Synthesis. High quality crystalline ingots (~7 g) of $Sn_{1.03-x}Mg_xTe$ (x = 0-0.12) were synthesized by mixing appropriate ratios of high-purity starting materials of Sn, Mg and Te in a carbon coated quartz tube. The tubes were sealed under vacuum (10^{-5} Torr) and slowly heated to 450 ^{o} C over 12 hrs, then heated up to 900 ^{o} C in 5 hrs, soaked for 10 hrs, and cooled slowly to room temperature.

3.2.3. Powder X-ray diffraction. Powder X-ray diffraction for all of the samples were recorded using a Cu K_α (λ = 1.5406 Å) radiation on a Bruker D8 diffractometer.

3.2.4. Band gap measurement. To estimate optical energy difference between valence band and conduction band optical diffuse reflectance measurement has been done with finely ground powder at room temperature using FT-IR Bruker IFS 66 V/S spectrometer in a frequency range 4000-400 cm^{-1} with 2 cm^{-1} resolution and 50 scans. Absorption (α/Λ) data were calculated from reflectance data using Kubelka−Munk equations: $\alpha/\Lambda = (1-R)^2/(2R)$, where R is the reflectance, α and Λ are the absorption and scattering coefficients, respectively. The energy band gaps were derived from α/Λ vs E (eV) plots.

3.2.5. Electrical transport. Electrical conductivity and Seebeck coefficients were measured simultaneously under He atmosphere from room temperature to 873 K on a ULVAC-RIKO ZEM-3 instrument system. The typical sample for measurement had parallelepiped shape with the dimensions of ~2 × 2 × 8 mm^3. The longer direction coincides with the direction in which the thermal conductivity was measured.

3.2.6. Hall measurement. Carrier concentrations were determined using Hall coefficient measurements at room temperature with a PPMS system. Four-contact Hall-bar geometry was used for the measurement. At 300 K, we estimated the carrier concentration, *n*, from the formula: $n=1/eR_H$, where *e* is the electronic charge.

3.2.7. Thermal conductivity. Thermal diffusivity, *D*, was directly measured in the range 300−873 K by using laser flash diffusivity method in a Netzsch LFA-457. Coins with ~8 mm diameter and ~2 mm thickness were used in all of the measurements. Temperature dependent heat capacity, C_p, was derived using standard sample (pyroceram) in LFA-457. The total thermal conductivity, κ_{total}, was calculated using the formula, $\kappa_{total} = DC_p\rho$, where ρ is the density of the sample, measured using the sample dimension and mass. The density of the pellets obtained was in the range ~96% of the theoretical density.

3.2.8. Computational details. Density functional theoretical (DFT) electronic structure calculations of pristine SnTe and Mg alloyed SnTe were carried out using Quantum Expresso package.[31] Scalar relativistic norm conserving pseudopotentials and a Generalized Gradient Approximation (GGA) to exchange-correlation energy with functional of Perdew, Burke, and Erzenhoff (PBE) were used to perform the DFT calculations.[32] The valence electrons of Sn, Te and Mg ($5s^2 5p^2$, $5s^2 5p^4$ and $3s^2$ respectively) are included in calculations through the use of pseudopotentials. SnTe is known to crystallize in rocksalt structure, while MgTe occurs in the zinc blende structure.[20] Mg-substituted in the zinc blende site of SnTe was simulated with a tetragonal supercell ($\sqrt{2}$ x $\sqrt{2}$ x 2) containing 32 atoms. Plane wave basis for representing wavefunctions are terminated with energy cut off of 40 Ry, and 14X14X10 mesh of k points was used in sampling Brillouin zone integrations. Electronic structure of $Sn_{16}Te_{16}$, $Sn_{15}MgTe_{16}$ and $Sn_{14}Mg_2Te_{16}$ with Mg atoms substituted for Sn atoms in SnTe is determined along high symmetry lines in Brillouin zone, using theoretical equilibrium lattice constant of 6.417 Å. Theoretical calculation was performed in Prof. Umesh Waghmare's group in JNCASR. In order to support the experimental results, we have included the theoretical results in this chapter.

3.3. Results and Discussion

Previously, SnTe was not considered to be a good thermoelectric material due to its very high carrier concentration (~10^{21}) resulting from intrinsic Sn vacancy.[23] Electron donor dopant such as iodine doping in SnTe has optimizes the thermoelectric property by decreasing the carrier concentration.[27] Recently, Kanatzidis and co-worker have shown that self compensation of Sn is an effective path for optimizing the thermoelectric performance of

SnTe.[29] First, we have synthesized the self compensated $Sn_{1.03}Te$ sample, which shows significantly low hole concentration (~1.2 X 10^{20} cm^{-3}) compared to pristine SnTe (~4.5 X 10^{20} cm^{-3}). Further, the effect of Mg alloying on the thermoelectric property was investigated on self compensated $Sn_{1.03}Te$ sample.

$Sn_{1.03-x}Mg_xTe$ (x = 0, 0.02, 0.03, 0.05, 0.08, 0.09, 0.1) samples were synthesized by vacuum sealed tube melting reaction and characterized by powder XRD. Figure 3.1 (a) confirms formation of single phase nature within detection limit of PXRD and the patterns could be indexed on SnTe structure (*Fm*-3*m* space group). As shown in Figure 3.1 (b), the lattice parameter decreases with increasing the Mg concentration, consistent with the smaller radius of Mg^{2+} (86 pm) compared to that of Sn^{2+} (93 pm). Linear decrease in the lattice parameter follows solid solution Vegard's law.

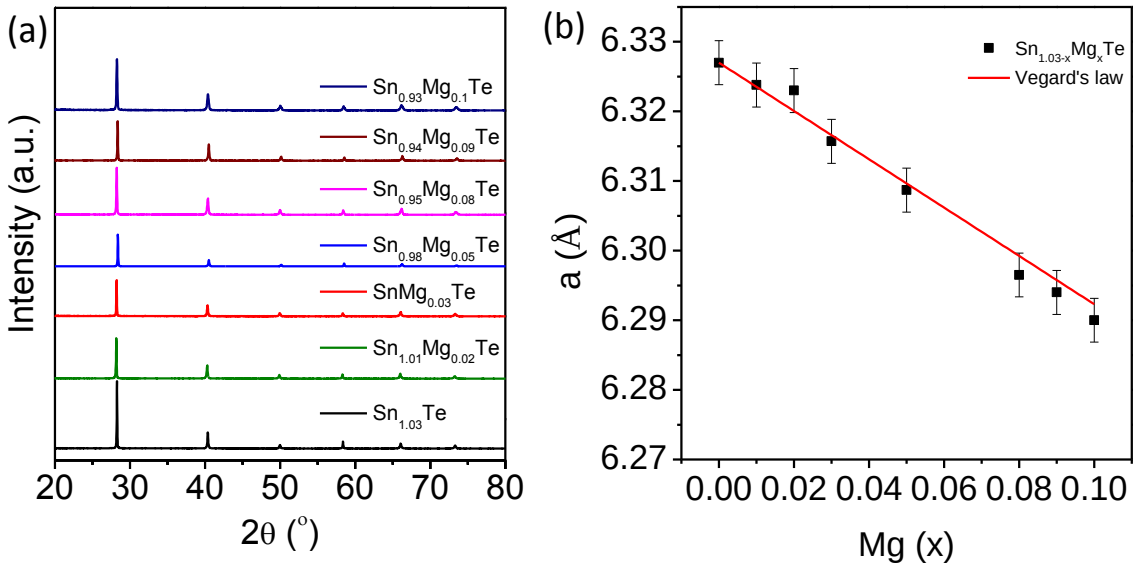

Figure 3.1 (a) Powder XRD patterns of $Sn_{1.03-x}Mg_xTe$ (x = 0 -0.1) samples. (b) Lattice parameter (*a*) vs. Mg concentration (*x*) in $Sn_{1.03-x}Mg_xTe$ and red line indicates the Vegard's law for solid solution.

We could able to resolve the band gap of $Sn_{1.03-x}Mg_xTe$ (x = 0-0.12) by diffuse reflectance IR spectroscopy (Figure 3.2). With increasing Mg concentration up to 12 mol%

the electronic absorption spectra of SnTe show a shift of absorption edge towards high energy. Generally, if MgTe (Eg ~3.5 eV) was dissolving in SnTe an increase in the band gap

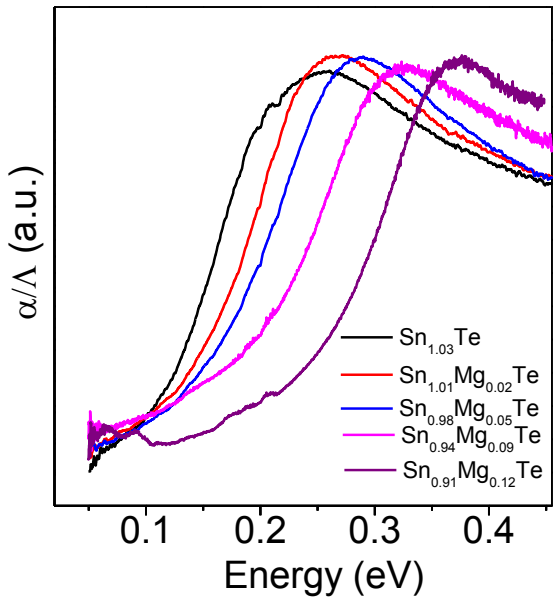

Figure 3.2 Electronic absorption spectra of $Sn_{1.03-x}Mg_xTe$.

would be expected. The band gap derived from the plot show an increase from ~0.11 eV to ~0.26 eV in going from 0 % to 12 % Mg in SnTe. This result is similar to that of MgTe alloyed with PbTe.[16] Increase in the band gap with Mg incorporation in SnTe is indicating reduction of the energy separation of light hole and heavy hole valence bands which will be discussed further in the later part of the chapter.

Figure 3.3 shows electrical transport property of $Sn_{1.03-x}Mg_xTe$ (x = 0-0.1). For all samples electrical conductivity (σ) decreases with increase in temperature which is typical of degenerate semiconductor (Figure 3.3 (a)). The electrical conductivity decreases with increasing Mg concentration up to 9 mol %, especially at room temperature from 9650 Scm^{-1} to 3114 Scm^{-1} (Figure 3.3 (a)). Typically, the room temperature σ of $Sn_{0.94}Te_{0.09}Te$ is to be 3114 Scm^{-1}, which decreases to 1015 Scm^{-1} at 856 K. The room temperature Hall

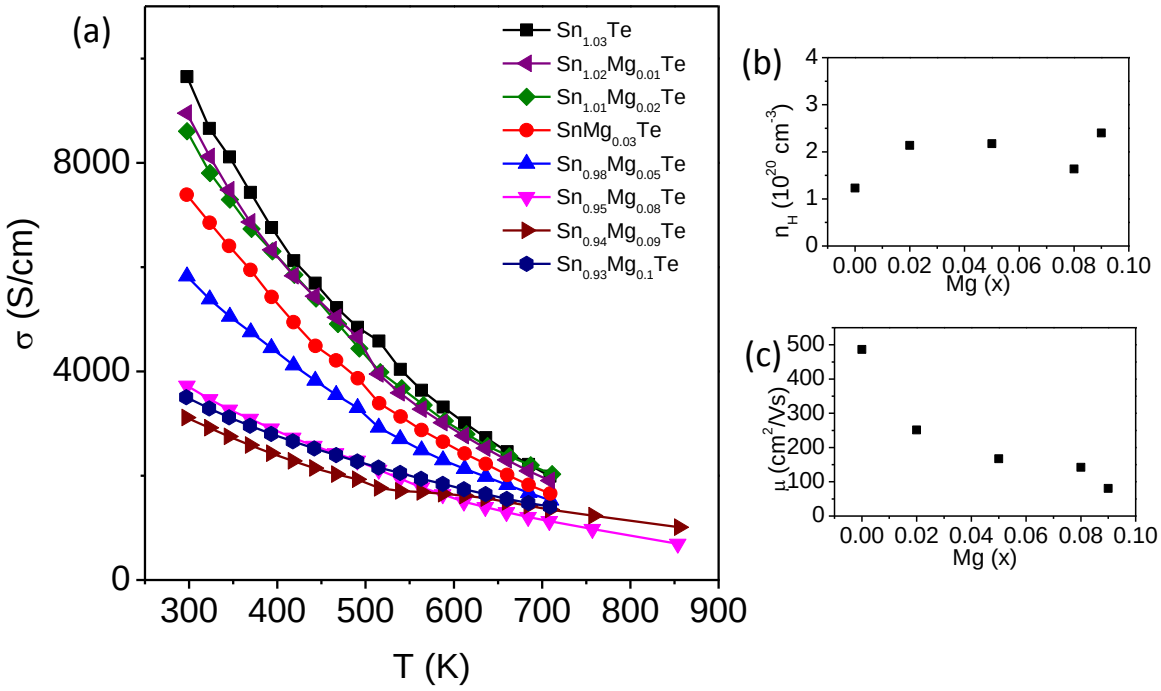

Figure 3.3 (a) Temperature dependent electrical conductivity (σ) of $Sn_{1.03-x}Mg_xTe$ samples (b) Carrier concentration (n) and (c) carrier mobility (μ) at room temperature with respect to Mg doping concentration (x) in $Sn_{1.03-x}Mg_xTe$.

coefficients, R_H, of all $Sn_{1.03-x}Mg_xTe$ (x = 0-0.1) samples are positive, which indicates the *p*-type conduction in this system. Interestingly, carrier concentration (n) at 300 K increases with increasing the Mg concentration up to 2 mol% and then almost remain flat with further increasing the Mg alloying up to 9 mol% (Figure 3.3 (b)). Anomalous change in the carrier concentration with the increase of Mg is difficult to explain, but similar behavior has been observed recently in In doped SnTe[13] and $SnTe_{1-x}Se_x$[30] and Cd alloyed SnTe.[29a] Recent report also shows the anomalous change in the carrier concentration in Hg doped SnTe.[29b] Although Mg, Cd and Hg is supposed to be isovalent with Sn; Cd appears to act as electron donor, whereas Mg and Hg acts as electron acceptor. Effect of different doping on the carrier concentration of SnTe is not very clear yet. Room temperature carrier mobility (μ) decreases with Mg concentration in $Sn_{1.03-x}Mg_xTe$ (Figure 3.3 (c)), which is due to impurity

scattering.[13, 30] Decrease in room temperature σ value with the increase in Mg doping concentration is due to the decrease in μ.

Figure 3.4 (a) represents temperature dependence of Seebeck coefficient (*S*) of $Sn_{1.03-x}Mg_xTe$ samples. Positive value of *S* indicates *p*-type conduction which supports the Hall coefficient measurement. Significant enhancement in *S* has been achieved by Mg alloying in SnTe, both at room temperature and high temperatures. Typically, the room temperature *S* value measured for $Sn_{0.95}Mg_{0.08}Te$ was ~38 μVK^{-1} which linearly increases to ~200 μVK^{-1} at 856 K. We have estimated effective mass (m^*) of $Sn_{1.03-x}Mg_xTe$ samples using the measured *S* and Hall carrier concentration (*n*) at room temperature.[17, 33] Although accurate calculation of m^* require consideration of non-parabolic band and multiple band model, present calculation of m^* considers only single parabolic band for simplicity.[17, 33] Increase in effective mass from ~0.16m_e to ~0.69m_e with increasing the Mg concentration from 0 to 9 mol% is observed (Table 3.1.), which is resulting probably due to the increasing contribution of heavy hole valence band of SnTe.

In Figure 3.4 (b), we compare the present room temperature *S* vs. *n* data of $Sn_{1.03-x}Mg_xTe$ samples with previously reported experimental data on In doped SnTe,[13] In doped $SnTe_{1-x}Se_x$,[30] Cd alloyed SnTe ,[29a] Hg alloyed SnTe,[29b] Bi doped SnTe,[34] Cu doped SnTe[23] and also with the earlier reported theoretical *S* vs. *n* curves by Zhang *et al.*[13] Theoretical Pisarenko (*S* vs. *n*) curves at room temperature have been calculated earlier by considering the contribution of both the light hole valence band (*L* point) and heavy hole valence band (Σ point) of SnTe.[13] This model uses a light hole band effective mass of ~0.168m_e, a heavy hole band effective mass of ~1.92m_e, and an energy gap between two valence bands of 0.35 eV, respectively. Indium and Cd/Hg alloyed SnTe samples show much higher Seebeck

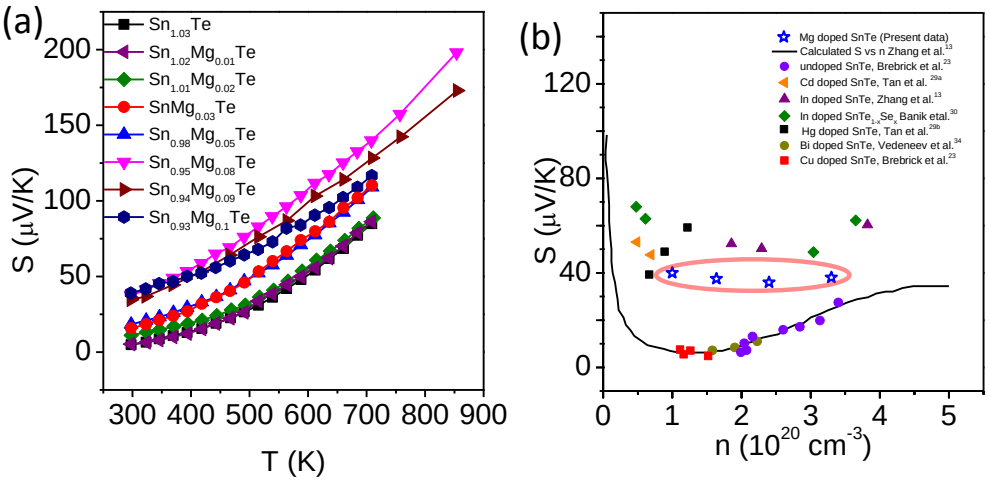

Figure 3.4 (a) Temperature dependent Seebeck coefficient (*S*) of $Sn_{1.03-x}Mg_xTe$ samples; (b) Room temperature *S* vs. *n* plot of the present $Sn_{1.03-x}Mg_xTe$ samples. For comparison, previously reported *S* vs. *n* experimental data of undoped SnTe[23], Cd doped SnTe[29], In doped SnTe,[13] In doped $SnTe_{0.85}Se_{0.15,}$[30] Hg doped SnTe,[29] Bi doped SnTe,[34] Cu-doped SnTe[23] and theoretical Pisarenko curve[13] are given in (b).

coefficient than that of theoretical Pisarenko curve due to the effect of resonance level formation[13, 30] and valence band convergence,[29] respectively. We observe that $Sn_{1.03-x}Mg_xTe$ samples also show significantly large Seebeck coefficients than that of Pisarenko curve (Figure 3.4 (b)).

Table 3.1. Room temperature carrier concentration (n_H) and effective mass (m^*) of $Sn_{1.03-x}Mg_xTe$ samples where m_e is mass of electron.

Composition	**n** (10^{20} **cm**$^{-3}$)	**m*(m$_e$)**
$Sn_{1.03}Te$	1.2	0.16
$Sn_{1.01}Mg_{0.02}Te$	2.1	0.25
$Sn_{0.98}Mg_{0.05}Te$	2.2	0.48
$Sn_{0.96}Mg_{0.07}Te$	3.3	0.90
$Sn_{0.95}Mg_{0.08}Te$	1.6	0.55
$Sn_{0.94}Mg_{0.09}Te$	2.4	0.69
$Sn_{0.93}Mg_{0.10}Te$	1.0	0.43

In order to understand the origin of enhancement in Seebeck coefficient we have performed DFT calculation of electronic structure of SnTe and Mg-alloyed SnTe (see in Figure 3.5 (a)). For $Sn_{16}Te_{16}$, $Sn_{15}MgTe_{16}$ (6 mol% Mg alloyed) and $Sn_{14}Mg_2Te_{16}$ (12 mol% Mg alloyed) systems, the principal valence band (light hole) maximum (VBM) and conduction band minima (CBM) occur at Γ point; and the heavy hole band is at Z+δ along Z →R direction. The VBM and CBM occurring at the L point in the Brillouin zone of cubic cell of SnTe folds on to the Γ point and the heavy hole valence band appearing along Σ folds on to Z+δ in the Brillouin zone of the 32 atom ($\sqrt{2}$ x $\sqrt{2}$ x 2) tetragonal supercell. Band gap of SnTe increases with increase in Mg alloying, consistent with the experimental band gap measured by diffuse reflectance spectroscopy. We note that underestimation of the gap in DFT calculations is typical. Band gap of 0.049 eV of $Sn_{16}Te_{16}$ at Γ point increases to 0.069 eV and 0.084 eV with substitution of 6 mol% and 12 mol% Mg for Sn atoms, respectively (Figure 3.5 (b)). This is due to the larger decrease in the energy of valence band in comparison with the conduction band at Γ point leading to opening of the band gap (Figure 3.5(c)).

Significant decrease in the energy separation between light and heavy valence band of SnTe is achieved with Mg alloying. The energy separation between the light hole and the heavy hole valence band decreases from 0.375 eV for pristine SnTe to 0.18 eV 12 mol% Mg alloyed SnTe sample (Figure 3.5 (c)). In figure 3.6 we have presented schematic of band diagram of $Sn_{1.03}Te$ and $Sn_{1.03-x}Mg_xTe$. From both experimental observation and theoretical calculation, it is clear that the incorporation of Mg in the SnTe leads to increase in the valence band degeneracy. Such valence band convergence is expected to result in enhancement of the Seebeck coefficient due to contribution from both the bands, as there is

an asymmetric increase in the density of states near the Fermi energy. Similar band modification have been found in Cd/Hg alloyed SnTe[29] and Cd and Mg alloyed PbTe.[16, 19]

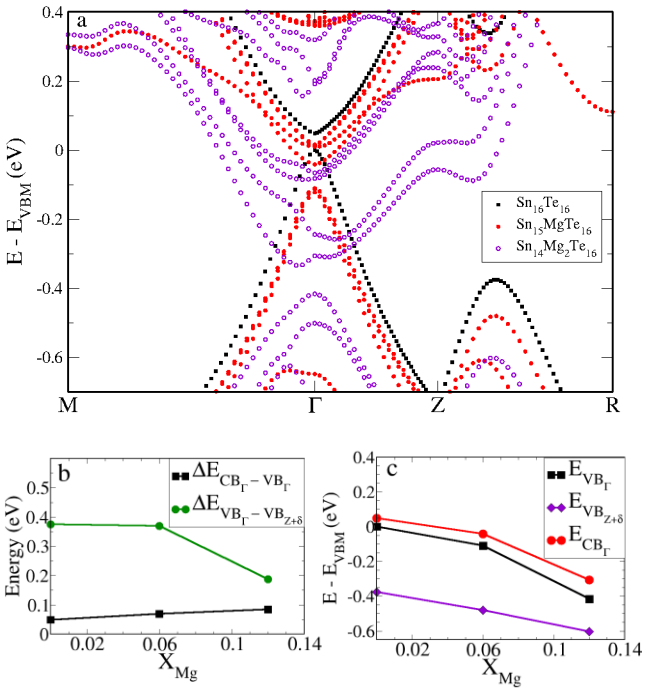

Figure 3.5 (a) Band structures of $Sn_{16}Te_{16}$, $Sn_{15}MgTe_{16}$, $Sn_{14}Mg_2Te_{16}$ supercell as a function of wavevector in supercell brillouin zone. The energies shown are relative to the valence band maxima of $Sn_{16}Te_{16}$. The band gap appears at Γ point and heavy hole band at Z+δ due to folding of the brillouin zone in the present supercell calculation. (b) Conduction band (C) and valence bands (Γ and Z+δ) energy differences as a function of concentration of Mg. (c) Band structures of $Sn_{16}Te_{16}$, $Sn_{15}MgTe_{16}$, $Sn_{14}Mg_2Te_{16}$ supercell as a function of concentration of Mg (X_{Mg}). The energies shown are relative to the valence band maxima of $Sn_{16}Te_{16}$.

Figure 3.7 represents temperature dependent power factor (σS^2) data of $Sn_{1.03-x}Mg_xTe$ (x = 0-0.1) samples. Benefiting from the significant enhancement in Seebeck coefficient both

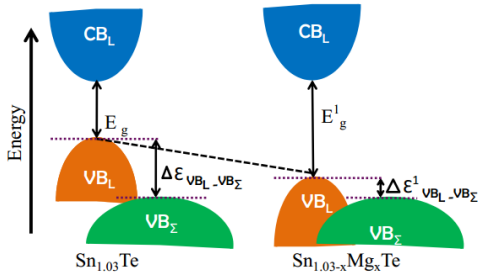

Figure 3.6 Schematic energy diagram of $Sn_{1.03}Te$ and $Sn_{1.03-x}Mg_xTe$.

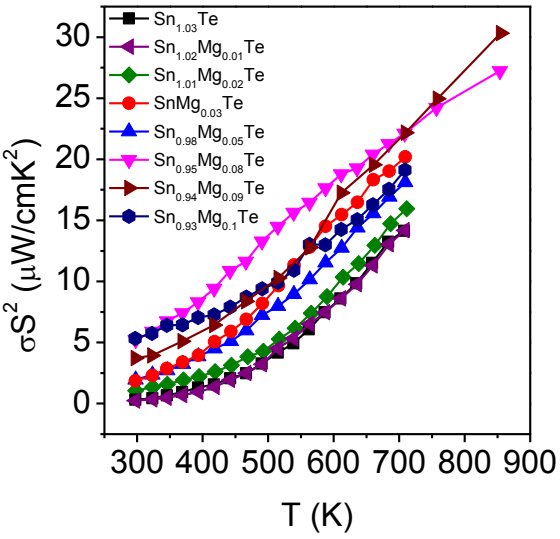

Figure 3.7 Temperature dependence of power factor (σS^2).

in low and high temperatures, Mg alloyed $Sn_{1.03}Te$ samples have much higher power factors than the undoped $Sn_{1.03}Te$ sample, with maximum values exceeding ~30.3 $\mu Wcm^{-1}K^{-2}$ (Figure 3.7). Maximum power factor value obtained in the present $Sn_{1.03-x}Mg_xTe$ ingot samples are indeed higher than previously reported spark plasma sintered In and Cd/Hg alloyed SnTe samples.[13, 29] Typically, at room temperature, σS^2 value for $Sn_{0.94}Mg_{0.09}Te$ is to be ~3.5 $\mu Wcm^{-1}K^{-2}$ which rises to ~30.3 $\mu W\ cm^{-1}K^{-2}$ at ~856 K.

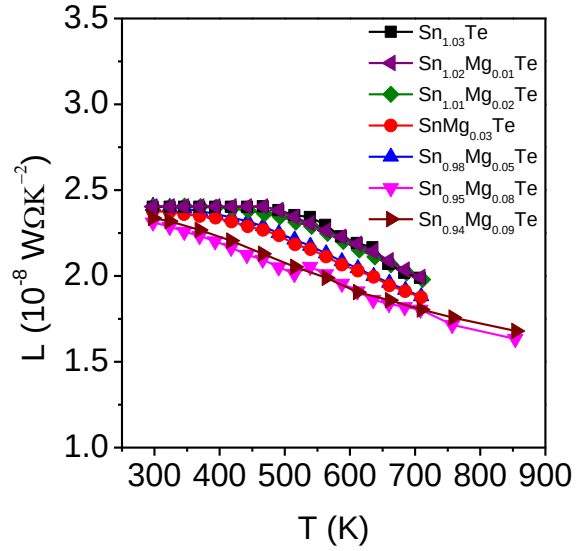

Figure 3.8 Temperature dependent Lorenz number (L) of $Sn_{1.03-x}Mg_xTe$.

The electronic thermal conductivities, $\kappa_{el} = L \cdot \sigma \cdot T$, were extracted based on fitting of the respective Seebeck values that estimate the reduced chemical potential from which the Lorenz number, L, can be obtained (Figure 3.8).[16, 17]

Mg alloying in $Sn_{1.03}Te$ optimizes the temperature dependent κ_{total} by controlling the κ_{el} (Figure 3.9). Figure 3.10 (a)) shows temperature dependent diffusivity (D) and specific heat (C_p).The temperature dependent C_p values are in good agreement with Dulong Petit C_p value (figure 3.10 (b)). In Figure 3.11, we present the temperature dependent total thermal conductivity (κ_{total}) and lattice thermal conductivity (κ_{lat}) of $Sn_{1.03-x}Mg_xTe$ (x = 0-0.09) samples. The κ_{lat} was obtained after subtracting the electronic part, κ_{el}, from the κ_{total}. With increasing the Mg concentration κ_{total} decreases due to the systematic decrease in κ_{el}. Typically, the room temperature κ_{total} value measured for $Sn_{0.94}Mg_{0.09}Te$ is ~4.9 $Wm^{-1}K^{-1}$ which decreases to ~2.2 $Wm^{-1}K^{-1}$ at 873 K. We have not observed any systematic trend for κ_{lat} with Mg concentration in $Sn_{1.03}Te$. Typically, the room temperature κ_{lat} value measured for $Sn_{0.94}Mg_{0.09}Te$ is ~2.7 $Wm^{-1}K^{-1}$ which decreases to ~0.78 $Wm^{-1}K^{-1}$ at 856 K, which is slightly higher, compared to Cd/Hg alloyed SnTe samples.[29]

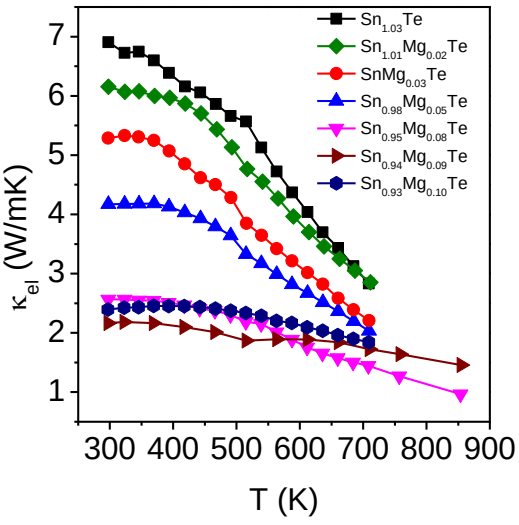

Figure 3.9 Temperature dependent electrical thermal conductivity (κ_{el}) of $Sn_{1.03-x}Mg_xTe$.

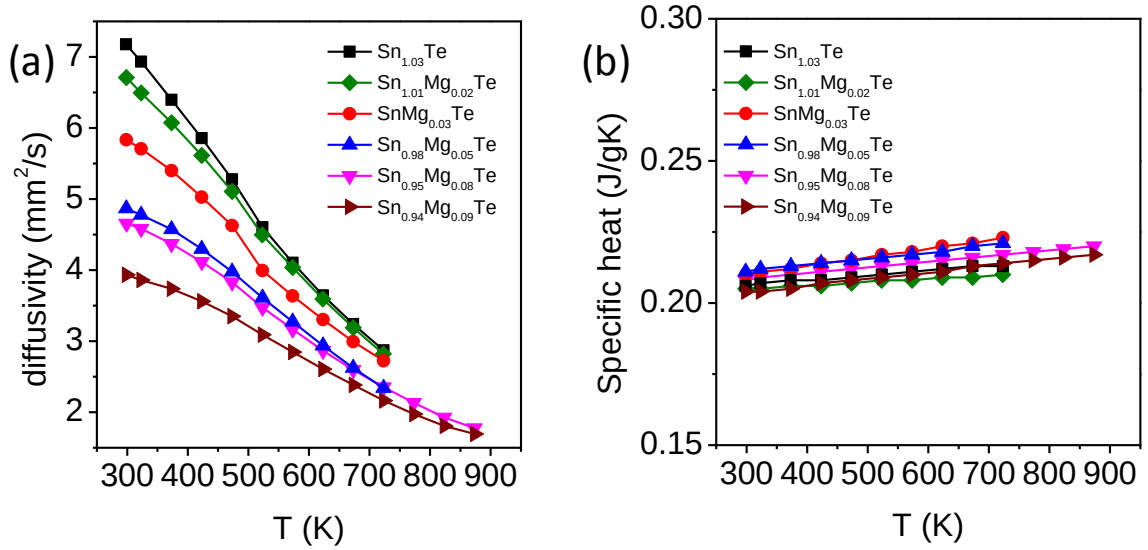

Figure 3.10 Temperature dependent (a) diffusivity (D), (b) heat capacity (C_p) of $Sn_{1.03-x}Mg_xTe$.

In Figure 3.12, we present temperature dependent ZT of $Sn_{1.03-x}Mg_xTe$ (x = 0-0.9) samples. The highest ZT value of ~1.2 at 856 K was achieved for $Sn_{0.94}Mg_{0.09}Te$, which is significantly higher compared to undoped $Sn_{1.03}Te$ sample. Highest ZT obtained in the

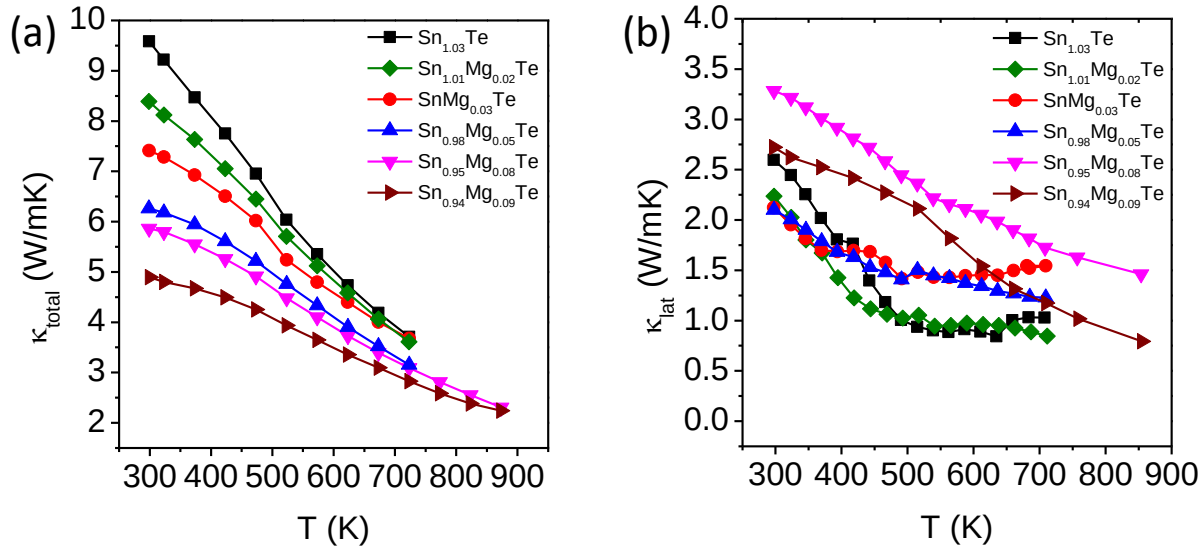

Figure 3.11 Temperature-dependent (a) total thermal conductivity (κ_{total}) and (b) lattice thermal conductivity (κ_{lat}).

present crystalline ingot sample synthesized by simple melting reaction is indeed comparable to previously reported maximum *ZT* of spark plasma sintered Cd alloyed (*ZT* ~ 1.3 at 873 K),[29] Hg alloyed (*ZT* ~1.3 at 910 K)[29] and In doped (*ZT*~1.1 at 873 K) SnTe samples.[13]

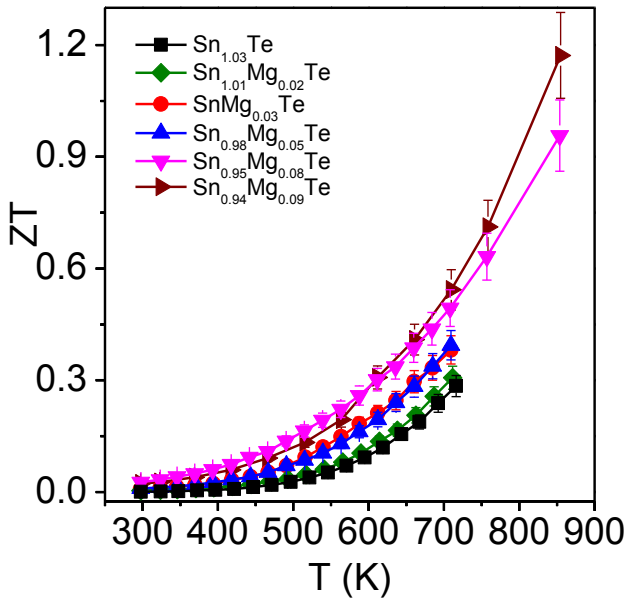

Figure 3.12 Temperature dependent *ZT* of $Sn_{1.03-x}Mg_xTe$.

3.4. Conclusions

p-type SnTe can be optimized to be a good thermoelectric material for power generation by controlling the hole concentration and improving the Seebeck coefficient. Mg alloying increases the band gap of $Sn_{1.03-x}Mg_xTe$ (x = 0-0.9) samples, which resulted decrease in the energy separation between two valence bands (light and heavy hole) of SnTe. Thus, effective convergence of the valence bands giving rise to significant enhancement in the Seebeck coefficient, resulted in remarkable increase in power factor of $Sn_{1.03-x}Mg_xTe$ (x = 0-0.9). This type of band engineering is a crucial finding of this work and is important in achieving a high figure of merit of ~1.2 at 856 K for *p*-type $Sn_{0.94}Mg_{0.09}Te$ sample. Present research suggests that SnTe-based materials are important candidates for thermoelectric

power generation and provides the promise to act as alternative of lead chalcogenides in near future.

References

1. Sootsman, J.; Chung, D. Y.; Kanatzidis, M. G. *Angew. Chem. Int. Ed.* **2009**, *48*, 8616.
2. Zhao, L. D.; Dravid, V. P.; Kanatzidis, M. G. *Energy Environ. Sci.* **2014**, *7*, 251.
3. Snyder, G. J.; Toberer, E. S. *Nat. Mater.* **2008**, *7*, 105.
4. (a) Zebarjadi, M.; Esfarjani, K.; Dresselhaus, M. S.; Ren, Z. F.; Chen, G. *Energy Environ. Sci.* **2012**, *5*, 5147. (b) Zhang, Y.; Stucky, G. D. *Chem. Mater.* **2014**, *26*, 837. (c) Gaultois, M. W.; Sparks, T. D.; Borg, C. K. H.; Seshadri, R.; Bonificio, W. D.; Clarke, D. R. *Chem. Mater.* **2013**, *25*, 2911.
5. Biswas, K.; He, J.; Zhang, Q.; Wang, G.; Uher, C.; Dravid, V. P.; Kanatzidis, M. G. *Nat. Chem.* **2011**, *3*, 160.
6. Biswas, K.; He, J.; Blum, I. D.; Wu, C. I.; Hogan, T. P.; Seidman, D. N.; Dravid, V. P.; Kanatzidis, M. G. *Nature* **2012**, *489*, 414.
7. Zhao, L. D.; Hao, S.; Lo, S. H.; Wu, C. I.; Zhou, X.; Lee, Y.; Li, H.; Biswas, K.; Hogan, T. P.; Uher, C.; Wolverton, C.; Dravid, V. P.; Kanatzidis, M. G. *J. Am. Chem. Soc.* **2013,** *135*, 7364.
8. Poudel, B.; Hao, Q.; Ma, Y.; Lan, Y.; Minnich, A.; Yu, B.; Yan, X.; Wang, D.; Muto, A.; Vashaee, D.; Chen, X.; Liu, J.; Dresselhaus, M. S.; Chen G.; Ren, Z. *Science* **2008**, *320*, 634.
9. Zhao, L. D.; Lo, S. H.; Zhang, Y.; Sun, H.; Tan, G.; Uher, C.; Wolverton, C.; Dravid, V. P.; Kanatzidis, M. G. *Nature* **2014**, *508*, 373.
10. Morelli, D. T.; Jovovic, V.; Heremans, J. P. *Phys. Rev. Lett.* **2008**, *101*, 035901.
11. Heremans, J. P.; Jovovic, V.; Toberer, E. S.; Saramat, A.; Kurosaki, K.; Charoenphakdee, A.; Yamanaka, S.; Snyder, G. J. *Science* **2008**, *321*, 554.
12. Ahmad, S.; Hoang, K.; Mahanti, S. D. *Phys. Rev. Lett.* **2006**, *96*, 56403.
13. Zhang, Q.; Liao, B.; Lan, Y.; Lukas, K.; Liu, W.; Esfarjani, K.; Opeil, C.; Broido, D.; Chen, G.; Ren, Z. *Proc. Natl. Acad. Sci. U. S. A.* **2013,** *110*, 13261.
14. Pei, Y.; Shi, X.; LaLonde, A.; Wang, H.; Chen, L.; Snyder, G. J. *Nature* **2011**, *473*, 66.
15. Liu, W.; Tan, X.; Yin, K.; Liu, H.; Tang, X.; Shi, J.; Zhang, Q.; Uher, C. *Phys. Rev. Lett.* **2012**, *108*, 166601.

16. Zhao, L. D.; Wu, H. J.; Hao, S. Q.; Wu, C. I.; Zhou, X. Y.; Biswas, K.; He, J. Q.; Hogan, T. P.; Uher, C.; Wolverton, C.; Dravid, V. P.; Kanatzidis, M. G. *Energy Environ. Sci.* **2013**, *6*, 3346.
17. Guin, S. N.; Chatterjee, A.; Negi, D. S.; Datta, R.; Biswas, K. *Energy Environ. Sci.* **2013**, *6*, 2603.
18. (a) Biswas, K.; He, J.; Wang, G.; Lo, S. H.; Uher, C.; Dravid, V. P.; Kanatzidis, M. G. *Energy Environ. Sci.* **2011**, *4*, 4675. (b) Lo, S. H.; He, J.; Biswas, K.; Kanatzidis, M. G.; Dravid, V. P. *Adv. Funct. Mater.* **2012**, *22*, 5175.
19. Pei, Y. Z.; LaLonde, A. D.; Heinz, N. A.; Shi, X. Y.; Iwanaga, S.; Wang, H.; Chen, L.; Snyder, G. J. *Adv. Mater*. **2011**, *23*, 5674.
20. Ohta, M.; Biswas, K.; Lo, S. H.; He, J.; Chung, D. Y.; Dravid, V. P.; Kanatzidis, M. G. *Adv. Energy Mater.* **2012**, *2*, 1117.
21. Rogers, L. M. *J. Phys. D Appl. Phys.* **1968**, *1*, 845.
22. Efimova, B. A.; Kaidanov, V. I.; Moizhes, B. Y.; Chernik, I. A. *Sov. Phys. - Sol. Stat.* **1966**, *7*, 2032.
23. Brebrick, R. F.; Strauss, A. J. *Phys. Rev.* **1963**, *131*, 104.
24. Brebrick, R. F. *J. Phys. Chem. Solids* **1963**, *24*, 27.
25. Han, M. K.; Androulakis, J.; Kim, S. J.; Kanatzidis, M. G. *Adv. Energy Mater.* **2012**, *2*, 157.
26. Chen, Y.; Nielsen, M. D.; Gao, Y. B.; Zhu, T. J.; Zhao, X.; Heremans, J. P. *Adv. Energy Mater.* **2012**, *2*, 58.
27. Zhou, M.; Gibbs, Z. M.; Wang, H.; Han, Y.; Xin, C.; Li, L.; Snyder, G. J. *Phys. Chem. Chem. Phys.* **2014**, *16*, 20741.
28. Andreev, A. A. *Sov. Phys. - Sol. Stat.* **1967**, *9*, 1232.
29. (a) Tan, G.; Zhao, L. D.; Shi, F.; Doak, J. W.; Lo, S-H.; Sun, H.; Wolverton, C.; Dravid, V. P.; Uher, C.; Kanatzidis, M. G. *J. Am. Chem. Soc*. **2014,** *136*, 7006. (b) Tan, G; Shi, F.; Doak, J. W.; Sun, H.; Zhao, L. D.; Wang, P.; Uher, C.; Wolverton, C.; Dravid, V. P.; Kanatzidis, M. G. *Energy Environ. Sci.* **2015**, *8*, 267.
30. Banik, A.; Biswas, K. *J. Mat. Chem. A* **2014**, *2*, 9602.

31. Giannozzi, P.; Baroni, S.; Bonini, N.; Calandra, M.; Car, R.; Cavazzoni, C.; Ceresoli, D.; Chiarotti, G. L.; Cococcioni, M.; Dabo, I.; Corso, A. D.; Gironkoli, S. de; Fabris, S.; Fratesi, G.; Gebauer, R.; Gerstmann, U.; Gougoussis, C.; Kokalj, A.; Lazzeri, M.; Martin-Samos, L.; Marzari, N.; Mauri, F.; Mazzarello, R.; Paolini, S.; Pasquarello, A.; Paulatto, L.; Sbraccia, C.; Scandolo, S.; Sclauzero, G.; Seitsonen, A. P.; Smogunov, A; Umari, P.; Wentzcovitch, R. M. *J. Phys. Condens. Matter.* **2009**, *21*, 395502.
32. Perdew, J.P.; Burke, K.; Ernzerhof, M. *Phys. Rev. Lett.* **1996**, *77*, 3865.
33. Guin, S. N.; Negi, D. S.; Datta, R.; Biswas, K. *J. Mater. Chem. A* **2014,** *2*, 4324.
34. Vedeneev, V. P.; Krivoruchko, S. P.; Sabo, E. P.; *Semiconductors* **1998**, *32*, 241.

Chapter 4

Low Temperature Soft Chemical Synthesis and Thermoelectric Properties of Ba-filled *p*-type Skutterudite Nanocrystals[†]

Summary: Bulk skutterudites, $CoSb_3$, are promising inorganic materials for thermoelectric power generation at high temperatures. Generally, bulk $CoSb_3$ is synthesized by high temperature solid state reactions. This chapter deals with the low temperature solution phase synthesis of *p*-type nanocrystalline $CoSb_3$ and Ba-filled $CoSb_3$. Increase in the temperature dependent Seebeck coefficient with simultaneous increase in temperature dependent electrical conductivity has been observed in the present nanocrystalline samples, which is unusual in the case of bulk $CoSb_3$. Efficient phonon scattering by nanoscale grain boundaries and the additional phonon damping due to the rattling of Ba in the void of nanocrystalline $CoSb_3$ give rise to low thermal conductivity, which results in improved thermoelectric performance in nanocrystalline *p*-type $Ba_{0.048}CoSb_3$.

[†]The paper based on this chapter has been published in : A. Banik and K. Biswas, *Mater. Sci. Semicond. Process*, **2014**, *27*, 593.

4.1. Introduction

Energy conservation and utilization is one of the major tasks for current century. Nearly 60% of utilized energy is wasted as heat. Thermoelectric material can be useful to convert waste heat to electrical energy and vice-versa.[1] The performance of thermoelectric materials is defined by dimensionless figure of merit, $ZT = \sigma S^2 T/(\kappa_{el} + \kappa_{lat})$, where σ, S, T, κ_{el} and κ_{lat} are the electrical conductivity, Seebeck coefficient, temperature, electronic thermal conductivity and lattice thermal conductivity, respectively.[1] Diverse approaches have been introduced to improve thermoelectric performance of inorganic materials such as introduction of resonant level in the electronic band,[2] convergence of multiple electronic bands,[3] phonon glass electron crystal approach,[4] nanostructuring of bulk materials[5] and all length scale phonon scattering.[6]

Binary skutterudites are promising inorganic materials for thermoelectric application.[7, 8] It crystallizes in body-centered cubic structure with general formula MX_3 (M = Co, Rh or Ir; X = P, As, Sb). Intrinsic nanoscale cages are created in crystal structure by corner sharing MX_6 octahedra (Figure 4.1).[9-11] The structure can be considered as simple cubic sublattice partially filled by almost square pnictogen rings, X_4. Large unit cell, heavy constituent atoms, low electronegetivity difference between atoms and high electrical conductivity make it attractive for thermoelectric application. Among skutterudites, $CoSb_3$ has attracted attention due to low band gap (~0.2 eV) and high carrier mobility. Thermal conductivity of pure $CoSb_3$ is about ~10 $Wm^{-1}K^{-1}$ at 300 K, which leads to low thermoelectric performance. Since the concept "phonon-glass-electron-crystal" was proposed by Slack,[4] extensive research has been carried out on void filling of $CoSb_3$ in order to reduce the thermal conductivity, hence to improve *ZT*.[10-20] The filling atoms are loosely bound to the nanocages (Figure 4.1),

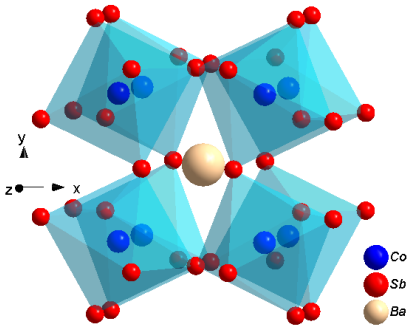

Figure 4.1 Crystal structure of Ba-filled $CoSb_3$.

leading to Einstein like vibration modes that strongly scatter phonons and reduce thermal conductivity. All these bulk void-filled $CoSb_3$ samples were synthesized by high temperature solid state techniques.

Low temperature cost effective wet chemical synthesis of inorganic nanomaterials, followed by densification into nanostructured-bulk materials provides another efficient route to decrease the thermal conductivity due to the phonon scattering by the nano/meso-scale grain boundaries. Report of low temperature solution phase synthesis of $CoSb_3$ is only few in the literature[21-24] and most of them ended up with impure $CoSb_3$ with Sb or $CoSb_2$ as second phase. Promising thermoelectric performance has been achieved in solution grown graphene /$CoSb_3$ nanocomposite due to reduction of thermal conductivity.[25] Low thermal conductivity in the temperature range 70-300 K have also been recently reported in *n*-type $CoSb_3$ synthesized via hydrothermal synthesis.[26]

In this chapter, we present a simple solution based low temperature synthesis of *p*-type nanocrystalline $CoSb_3$ and Ba-filled $CoSb_3$. Unusual increase in the temperature dependent Seebeck coefficient with simultaneous increase in the temperature dependent electrical conductivity has been observed, which is possibly due to carrier energy filtering at the nanoscale grain boundaries. Effective phonon scattering by the nano/mesoscale grain

boundaries and phonon damping due to rattling of Ba in the void of nanocrystalline $CoSb_3$ minimize the thermal conductivity to as low as ~0.42-0.6 $Wm^{-1}K^{-1}$ in 300-710 K range, resulting in improved thermoelectric performance.

4.2. Experimental section

4.2.1. Reagents. Antimony chloride ($SbCl_3$, Alfa Aesar 99+ %), cobalt chloride ($CoCl_2.6H_2O$, Sigma Aldrich 99.0 %), barium chloride ($BaCl_2$, Sigma-Aldrich 99.9 %), tetra ethylene glycol (TEG, Sigma Aldrich 99 %), and ethanol were used for synthesis.

4.2.2. Synthesis. In order to prepare $Ba_{0.075}CoSb_3$ (nominal composition) nanocrystals, $SbCl_3$ (143.8 mg, 0.630 mmol), $CoCl_2.6H_2O$ (50 mg, 0.210 mmol), $BaCl_2$ (3 mg, 0.015mmol) and TEG (20 ml) were taken in a round bottom flask and stirred the mixture for 2 hrs at room temperature inside a N_2 glove box. Then, excess $NaBH_4$ (54 mg, 1.427 mmol) was added into the reaction mixture and waited for 30 min. Black coloured reaction mixture was then transferred to Teflon lined stainless steel autoclave inside N_2 glove box. Then the autoclave was placed in a preheated hot air oven for 72 hrs at 250 °C. After completion of reaction, the autoclave was cooled slowly to room temperature and pure black product was obtained by centrifuging followed by washing with ethanol and water. Finally the product was dried under vacuum at 60 ^oC. We have also synthesized nanocrystalline $CoSb_3$ by adopting similar procedure.

In order to measure thermoelectric properties, nanocrystalline powder was pressed at room temperature into rectangular bars ($2 \times 2 \times 8$ mm^3) and disks (2 mm thickness by 8 mm diameter) shaped samples using an cold-press apparatus. The rectangular and disk shaped

samples were sealed in quartz tube under vacuum (10^{-5} Torr) and then sintered at 450 °C for 3 h.

4.2.3. Powder X-ray diffraction. Room temperature powder X-ray diffraction for all of the samples were recorded using a Cu K_α (λ = 1.5406 Å) radiation on a Bruker D8 diffractometer. Rietveld refinement of the PXRD pattern was performed using FULLPROF software.[27]

4.2.4. Field emission scanning electron microscopy. FESEM experiment has been performed using NOVA NANO SEM 600. Energy dispersive spectroscopy (EDS) analysis has been performed with an EDAX Genesis instrument attached to the SEM column. Actual concentration of Co, Sb and Ba were estimated by EDX analysis, which is nearly same to the nominal composition of the nanocrsystals.

4.2.5. Transmission electron microscopy. TEM experiments were performed using a JEOL (JEM3010) transmission electron microscope (TEM) fitted with a Gatan CCD camera operating at a 300 KV accelerating voltage. In a holey carbon coated Cu grid, one drop of nanocrystals dispersed in ethanol solution was taken for TEM imaging.

4.2.6. Electrical transport. Electrical conductivity and Seebeck coefficients were measured simultaneously under helium atmosphere from room temperature to 723 K on a ULVAC-RIKO ZEM-3 instrument system. The sample for measurement had a rectangular shape with the dimensions of ~ 2 × 2 × 8 mm^3. The longer direction coincides with the direction in which the thermal conductivity was measured. Heating and cooling cycles gave reversible electrical properties for given samples.

4.2.7. Thermal transport. Thermal diffusivity, *D*, was directly measured in the range 300−723 K by using laser flash diffusivity method in a Netzsch LFA-457. Coins with 8 mm

diameter and 2 mm thickness were used in all of the measurements. Temperature dependent heat capacity, C_p, was derived using standard sample (pyroceram) in LFA-457. Total thermal conductivity, κ_{total}, was calculated using the formula, $\kappa_{total} = D.C_p.\rho$, where ρ is the density of the sample, measured using the sample dimension and mass. The density of the pellets was ~91% of the theoretical density.

4.3. Results and discussion

Powder X-ray diffraction patterns (PXRD) (Figure 4.2) of the pristine and Ba-filled $CoSb_3$ nanocrytals obtained after 72 hrs of reaction could be indexed on the pure $CoSb_3$ structure (space group *Im*-3). Figure 4.2 also shows the PXRD of bulk $CoSb_3$ for comparison.

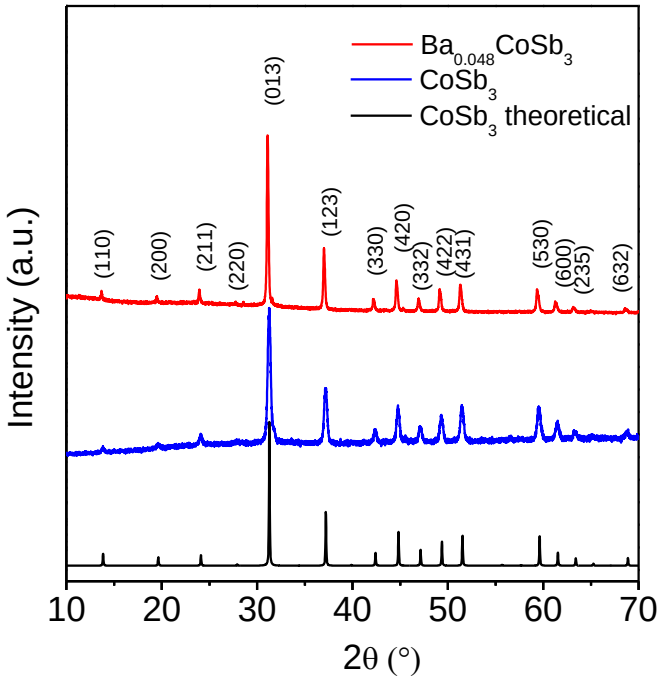

Figure 4.2 Powder XRD patterns of as prepared nanocrystalline $CoSb_3$ and Ba-filled $CoSb_3$.

In order to understand the mechanism of the formation of pure $CoSb_3$, we have measured the PXRD of the product at intermediate reaction time of 40 hrs and it indicates the formation of $CoSb_3$ along with Sb and $CoSb_2$ as intermediate phases (Figure 4.3). At the beginning, $NaBH_4$ reduces $CoCl_2$ and $SbCl_3$ to metallic Co and Sb. Partial reaction of Co and Sb may gives rise to $CoSb_2$ phase at lower reaction time. Prolonged reaction time facilitates the reaction between $CoSb_2$ and un-reacted Sb, which result in pure nanocrystalline $CoSb_3$ phases. Probable reaction mechanism could be written as follows:

$$CoCl_2 + 2NaBH_4 \rightarrow Co + 2BH_3 + 2NaCl + H_2$$

$$2SbCl_3 + 6NaBH_4 \rightarrow 2Sb + 6BH_3 + 6NaCl + 3H_2$$

$$Co + 2Sb \rightarrow CoSb_2;\ CoSb_2 + Sb \rightarrow CoSb_3$$

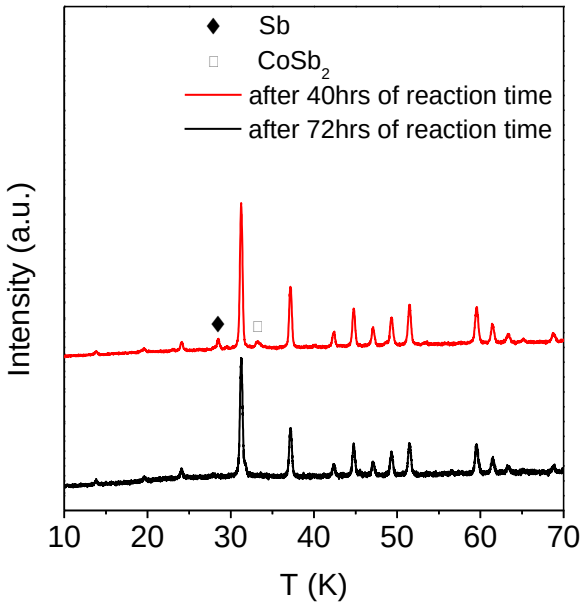

Figure 4.3 PXRD patterns of $CoSb_3$ samples synthesized at 250 ^oC for 40 hrs and 72 hrs respectively.

$BaCl_2$ acts as Ba source to partially fill the void in $CoSb_3$. We could able to confirm the presence of Ba in the nanocrystalline $Ba_{0.075}CoSb_3$ (nominal composition) by EDAX. Actual

composition of the sample obtained from EDAX is $Ba_{0.04}CoSb_3$ which is lower than the used nominal composition (Figure 4.4). This analysis suggests that only some part of the used Ba in the reaction goes to the cage of $CoSb_3$ and the remaining Ba leaves behind in the reaction solution. In order to obtain the occupancy and lattice parameter of Ba containing $CoSb_3$ we have performed Rietveld refinement of the PXRD pattern (Figure 4.5) which confirms that

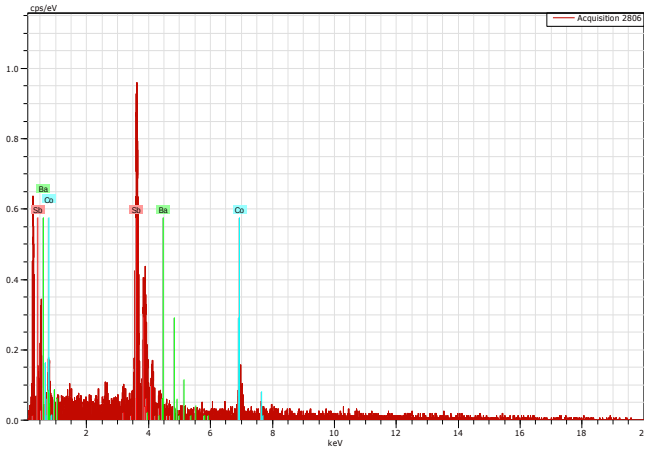

Figure 4.4 EDAX spectrum of Ba containing $CoSb_3$ which shows the presence of Ba in the $CoSb_3$ sample. Actual composition obtained from EDAX data is $Ba_{0.04}CoSb_3$.

Ba occupies classic rattler site (Wyckoff position 2a) (Table 4.1.) of $CoSb_3$. This result is

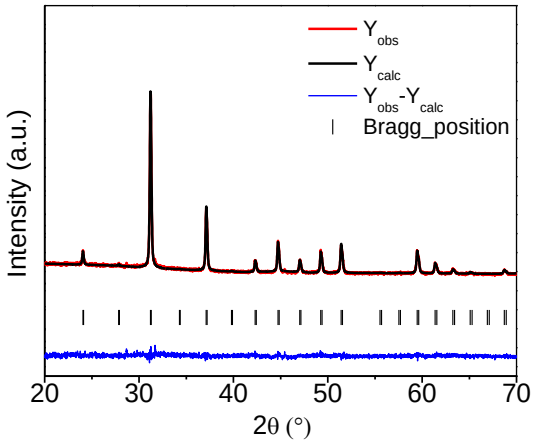

Figure 4.5 Rietveld refinement of PXRD pattern of $Ba_{0.048}CoSb_3$.

similar to that of In filled $CoSb_3$.[28] The actual composition obtained from refinement is $Ba_{0.048}CoSb_3$, which is close to EDAX composition ($Ba_{0.04}CoSb_3$). The lattice constant values obtained for $CoSb_3$ and Ba filled $CoSb_3$ were 9.0440(3) Å and 9.05493(4) Å respectively. Slight expansion of the lattice parameter in the Ba containing sample compared to that of pristine $CoSb_3$ is consistent with the literature.[13, 28] This result also indicates the filling of Ba in the cage of nanocrystalline $CoSb_3$. We must point out that we have not observed any second phase impurity in the synthesis Ba- filled $CoSb_3$ nanocrystals, which is confirmed by Rietveld refinement of the PXRD pattern.

Table 4.1. Refined atomic position for the Ba- filled $CoSb_3$ at room temperature. The refined lattice parameter is 9.05493 (4) Å. The R-Brag factor for the refinement is 6.59% over the 2θ range 20-70 ° at a wavelength of 1.54 Å. The actual composition obtained from refinement is $Ba_{0.048}CoSb_3$.

Atom	Position	Occu.	x	y	z
Co	**8c**	**1**	**0.250**	**0.250**	**0.250**
Sb	**24g**	**1**	**0**	**0.33428**	**0.15700**
Ba	**2a**	**0.19**	**0.0**	**0.0**	**0.0**

Figure 4.6 (a) and 4.6 (b) shows the FESEM and TEM images of as synthesized $CoSb_3$ sample. Shape of the nanoparticles is irregular and nanoscale grains are closely joined each other, which is due to the absence of organic capping agent in present synthesis. Average grain size obtained from FESEM and TEM image is 70 nm. The High resolution TEM (HRTEM) image of nanoparticles in Figure 4.6 (c) shows (220) planes with a *d*-spacing of 3.19Å, confirms crystalline nature.

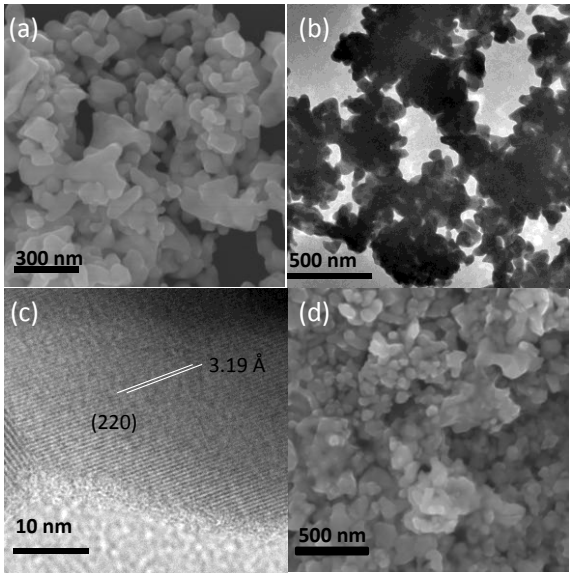

Figure 4.6 (a) FESEM image, (b) TEM and (c) HRTEM images of as synthesized nanocrystalline $CoSb_3$. (d) FESEM of $CoSb_3$ after densification and sintering.

In order to get good electronic transport properties, we have not used any external organic capping agent during the synthesis. For the electronic and thermal transport measurements, as synthesized nanocrystals were densified through cold pressing followed by sintering in a vacuum (10^{-5} Torr) sealed quartz tube at 450 °C for 3 h. The sample became much more compact, and the adjacent nanoscale grains are closely attached to each other with a small increase in the grain size (80 nm) as can be seen from the FESEM image (Figure 4.6 (d)) acquired after sintering.

The temperature dependent electrical transport properties of nanocrytalline $CoSb_3$ and barium filled $CoSb_3$ samples in the 300-710 K range are presented in figure 4.7. We have measured heating-cooling cycle electrical transport data (Figure 4.7) to exclude the sintering effect and to confirm the reproducibility. Typically, the nanocrystalline $Ba_{0.048}CoSb_3$ has σ

of ~85 Scm^{-1} at 300 K, which increases to ~150 Scm^{-1} at 710 K (Figure 4.7 (a)). Similar behaviour has also been observed for pristine $CoSb_3$ nanoparticles.

The positive sign of *S* indicates *p*-type conduction in both nanocrytalline $CoSb_3$ and $Ba_{0.048}CoSb_3$ (Figure 4.7 (b)). Typically, the room temperature *S* value is to be 46 μVK^{-1}, which increases to 145 μVK^{-1} at 710 K for nanocrystalline $Ba_{0.048}CoSb_3$ (Figure 4.7 (b)).

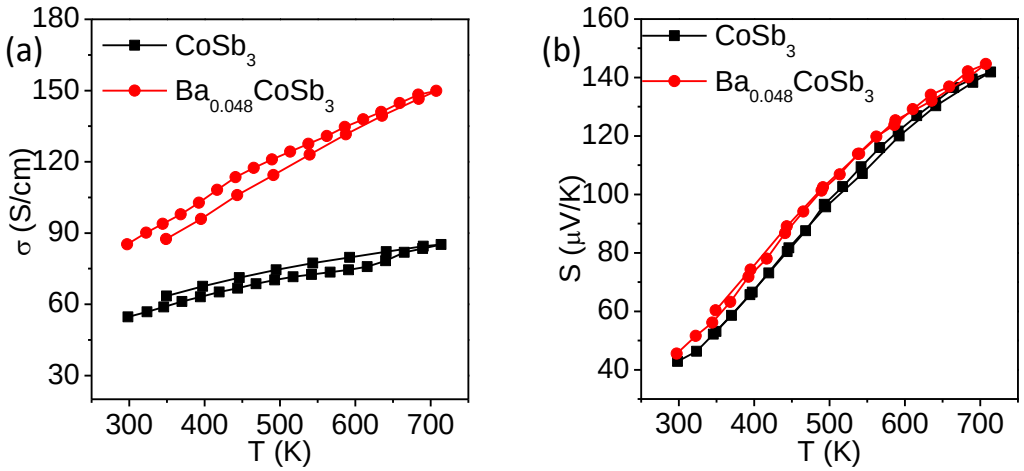

Figure 4.7 Temperature dependent (a) electrical conductivity (σ) and (b) Seebeck coefficient (*S*) of nanocrystalline $CoSb_3$ and $Ba_{0.048}CoSb_3$.

Increase in temperature dependent *S* with the simultaneous increase in the temperature dependent σ is unusual but useful for thermoelctric application. Unusual increase in *S* can be possibly due to carrier energy filtering by the potential barrier at the nanoscale grain boundaries. It is noticeable that the potential barriers at the interfaces and grain boundaries can filter low energy carriers (see figure 4.8), hence contribute to enhance its *S* value.[29]

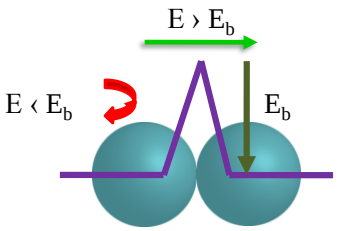

Figure 4.8 Schematic explains the carrier energy filtering at nanoscale grain boundaries.

When potential barrier scattering of carriers at the interfaces is dominant mechanism, the σ is expressed as $\sigma(T) \sim (1/T^{1/2})exp(-E_B/k_BT)$, where E_B is the barrier height.[30] A plot of $\ln(\sigma\sqrt{T})$ vs. T^{-1} is shown in the figure 4.9 along with the linear fit to the above equation, that yields a barrier height, E_B, of ~34 meV for both the pristine and Ba-filled $CoSb_3$ nanocrytals.

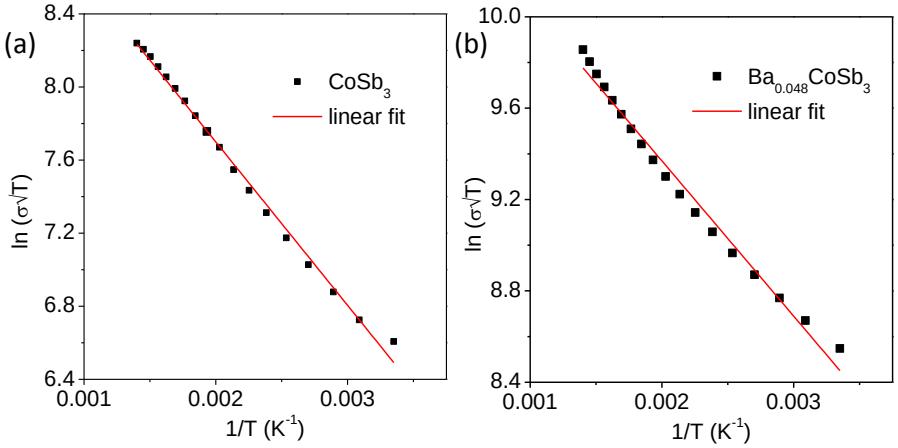

Figure 4.9 Plot of $\ln(\sigma\sqrt{T})$ vs T^{-1}. Linear fit supports the carrier energy filtering mechanism both in the case of (a) $CoSb_3$ and (b) $Ba_{0.048}CoSb_3$.

On the basis of the temperature dependent σ and S, maximum power factors, σS^2, were estimated to be ~1.7 and ~3.12 $\mu Wcm^{-1}K^{-2}$ at 707 K for nanocrystalline $CoSb_3$ and barium filled $CoSb_3$ samples, respectively (Figure 4.10). We have measured higher power factor (σS^2) for nanocrystalline Ba filled $CoSb_3$ sample compared to that of unfilled

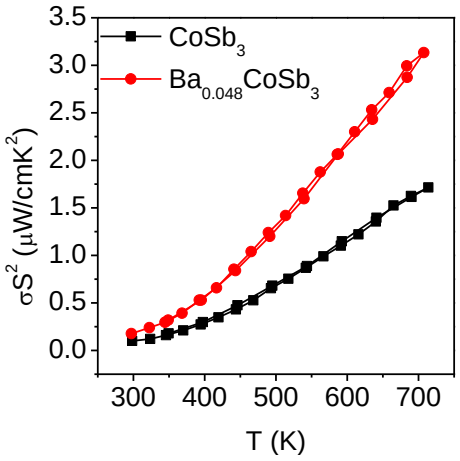

Figure 4.10 Temperature dependent power factor (σS^2) of nanocrystalline $CoSb_3$ and $Ba_{0.048}CoSb_3$.

nanocrystalline $CoSb_3$, which is due to enhanced electrical conductivity in the case of $Ba_{0.048}CoSb_3$ sample (see in Fig 4.10), which is known in the case of bulk samples.[13]

We have presented temperature dependence of thermal diffusivity (D) and specific heat capacity (C_p) in figure 4.11. Figure 4.12 shows the temperature dependent total thermal conductivity (κ_{total}) of nanocrytalline pristine $CoSb_3$ and $Ba_{0.048}CoSb_3$. At room

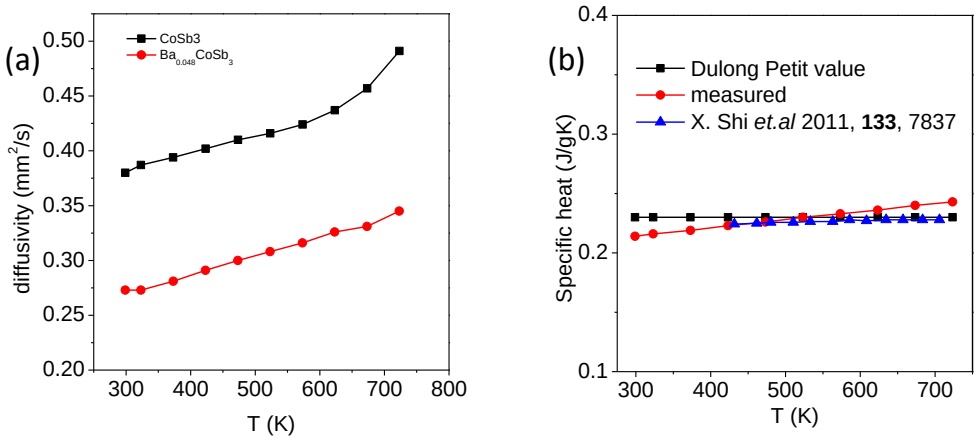

Figure 4.11 Temperature dependent (a) thermal diffusivity (D) and (b) specific heat (C_p) for $CoSb_3$ and $Ba_{0.048}CoSb_3$ samples.

temperature, κ_{total} values of ~0.6 $Wm^{-1}K^{-1}$ and ~0.42 $Wm^{-1}K^{-1}$ were measured for nanocrytalline $CoSb_3$ and $Ba_{0.048}CoSb_3$, respectively. We observe lower κ_{total} values in the case of $Ba_{0.048}CoSb_3$ compared to that of $CoSb_3$, which is due to the phonon damping owing

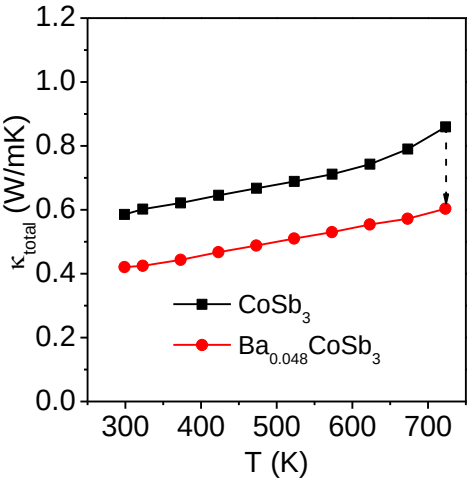

Figure 4.12 Temperature dependent total thermal conductivity (κ_{total}).

to rattling of Ba in the void of nanocrystalline $CoSb_3$.The electronic thermal conductivities ($\kappa_e = L \cdot \sigma \cdot T$) were extracted by fitting the respective Seebeck values to estimate the reduced chemical potential from which the Lorenz number, *L*, can be obtained as explained in detail elsewhere.[31] Calculated Lorenz numbers for different nanocrytalline $CoSb_3$ and $Ba_{0.048}CoSb_3$ samples are given in figure 4.13.

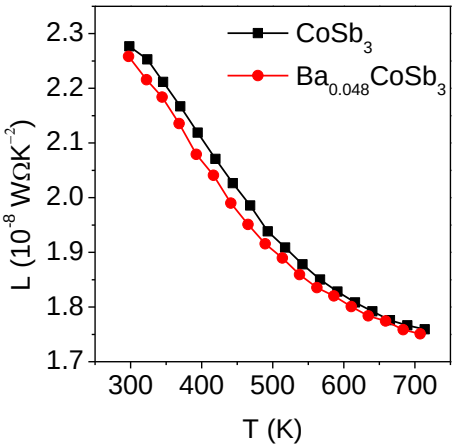

Figure 4.13 Temperature dependent Lorenz number (*L*) of nanocrystalline $CoSb_3$ and $Ba_{0.048}CoSb_3$.

The lattice thermal conductivity, κ_{lat}, (Figure 4.14) was obtained after subtracting the electronic thermal conductivity, κ_{el}, from the κ_{total}. This assumes a parabolic band model and energy independent scattering time. At room temperature $Ba_{0.048}CoSb_3$ sample exhibits κ_{lat} value of ~0.36 $Wm^{-1}K^{-1}$, which remains almost flat within the 300-700 K range. Similar low values of thermal conductivities have also been reported in literature.[23] The thermal conductivity of the present sample is lower than that for the $CoSb_3$ sample fabricated by the conventional melting-annealing route and $CoSb_3$ synthesized by a similar solution phase route followed by hot-pressing.[22] The measured low κ_{lat} in the present system is due to: a) effective phonon scattering by the nanoscale grain boundaries and b) additional phonon damping due to rattling of Ba in the void of nanocrystalline $CoSb_3$.

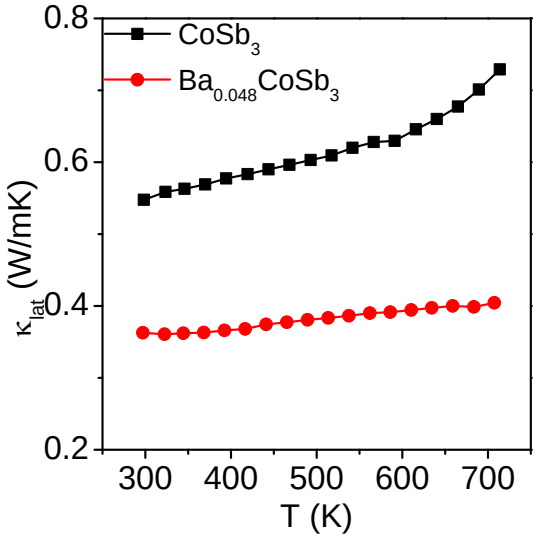

Figure 4.14 Temperature dependent lattice thermal conductivity (κ_{lat}) of nanocrystalline $CoSb_3$ and $Ba_{0.048}CoSb_3$.

Figure 4.15 presents temperature dependent *ZT* values of nanocrystalline $CoSb_3$ and $Ba_{0.048}CoSb_3$. The highest *ZT* value of ~0.4 at 710 K was achieved for $Ba_{0.048}CoSb_3$, which is significantly higher than that of pristine nanocrystalline $CoSb_3$ sample (Figure 4.15). *ZT* value of pristine bulk $CoSb_3$ is reported to be ~0.08 at 600 K which is lower than that of present nanocrystalline $CoSb_3$.[14] Thermal conductivity of the present sample is lower than that for the bulk $CoSb_3$ which gives rise to high *ZT* in nanocrystalline $CoSb_3$.

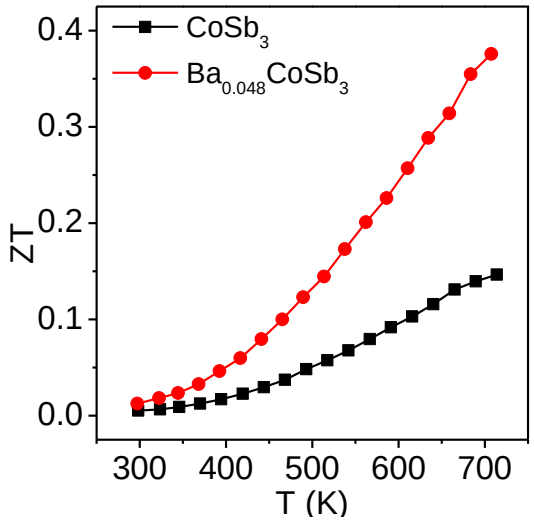

Figure 4.15 Temperature dependent thermoelectric figure of merit (*ZT*) of nanocrystalline $CoSb_3$ and $Ba_{0.048}CoSb_3$.

4.4. Conclusions

In conclusion, nanocrystalline *p*-type $CoSb_3$ and Ba-filled $CoSb_3$ samples have been synthesized by low temperature solution based synthesis. In order to obtain better electronic transport, we have not used external organic capping ligands during present synthesis. Unusual increase in the temperature dependent Seebeck coefficient with simultaneous increase in the temperature dependent electrical conductivity have been observed, which is due to the carrier energy filtering at the nanoscale grain boundaries. Effective phonon scattering by the nanoscale grain boundaries and the additional phonon damping due to the rattling of Ba in the void of nanocrystalline $CoSb_3$ give rise to low thermal conductivity. Peak *ZT* value of ~0.4 at 710 K was achieved in nanocrystalline *p*-type $Ba_{0.048}CoSb_3$, which is higher than that of pristine nanocrystalline $CoSb_3$. Present findings demonstrate the importance of cost effective low temperature solution phase synthesis to produce the advance thermoelectrics materials.

References

1. (a) Zhao, L. -D.; Dravid, V. P.; Kanatzidis, M. G. *Energy Environ. Sci.* **2014**, *7*, 251. (b) Sootsman, J.; Chung, D. Y.; Kanatzidis, M. G. *Angew. Chem. Int. Ed*. **2009**, *48,* 8616. (c) Snyder, G. J.; Toberer, E. S. *Nat. Mater.* **2008**, *7*, 105. (d) Zebarjadi, M.; Esfarjani, K.; Dresselhaus, M. S.; Ren, Z. F.; Chen, G. *Energy Environ. Sci.* **2012**, *5*, 5147. (e) Zhang, Q.; Malliakas, C. D.; Kanatzidis, M. G. *Inorg. Chem.* **2009**, *48,* 10910. (f) Zhao, W.; Fan, S.; Xiao, N.; Liu, D.; Tay, Y. Y.; Yu, C.; Sim, D.; Huey, H. H.; Zhang, Q.; Boey, F.; Ma, J.; Zhao, X.; Zhanga, H.; Yan, Q. *Energy Environ. Sci.* **2012**, *5*, 5364. (g) Wu, J.; Sun, Y.; Xu, W.; Zhang, Q. *Syn Met.* **2014**, *189*, 177.
2. (a) Heremans, J. P.; Jovovic, V.; Toberer, E. S.; Saramat, A.; Kurosaki, K.; Charoenphakdee, A.; Yamanaka, S.; Snyder, G. J. *Science* **2008**, *321*, 554. (b) Liu, W.; Tan, X.; Yin, K.; Liu, H.; Tang, X.; Shi, J.; Zhang, Q.; Uher, C. *Phys. Rev. Lett.* **2012**, *108*, 166601.
3. Pei, Y.; Shi, X.; La Londe, A.; Wang, H.; Chen, L.; Snyder, G. J. *Nature* **2011**, *473*, 66.
4. Slack, G. A. CRC Handbook of Thermoelectrics; Rowe, D. M., Ed.; CRC Press: Boca Raton, FL, **1995**, *405.*
5. (a) Biswas, K.; Zhang, H. Q.; Wang, G.; Uher, C.; Dravid, V. P.; Kanatzidis, M. G. *Nat. Chem*. **2011,** *3*, 160. (b) Poudel, B.; Hao, Q.; Ma, Y.; Lan, Y.; Minnich, A.; Yu, B.; Yan, X.; Wang, D.; Muto, A.; Vashaee, D.; Chen, X.; Liu, J.; Dresselhaus, M. S.; Chen, G.; Ren, Z. *Science* **2008**, *320*, 634.
6. (a) Biswas, K.; He, J.; Blum, I. D.; Wu, C. I.; Hogan, T. P.; Seidman, D. N.; Dravid, V. P.; Kanatzidis, M. G. *Nature* **2012**, *489*, 414. (b) Zhao, L. -D.; Hao, S.; Lo, S. –H.; Wu,

C. –I.; Zhou, X.; Lee, Y.; Li, H.; Biswas, K.; Hogan, T. P.; Uher, C.; Wolverton, C.; Dravid, V. P.; Kanatzidis, M. G. *J. Am. Chem. Soc.* **2013**, *135*, 7364.

7. Tritt, T. M. *Science* **1999**, *283*, 804.
8. Calliot, T.; Borshevesky, J. P. *Fleurial in proc. 11th Int. Confo. On Thermoelectrics (Ed :K. R. Rao) CRC Press Arlington*, TX, **1993**, *9*.
9. (a) Sales, B. C.; Mandrus, D. G.; Chakoumakos, B. C. *In Recent Trends in Thermoelectric Materials Research II, Semiconductors and Semimetals*; Tritt, T. M. Ed.; Academic Press: San Diego **2000**, 69, 1. (b) Morelli, D. T.; Meisner, G. P. *J. Appl. Phys.* **1995**, *77*, 3777. (c) Uher, C. *In Recent Trends in Thermoelectric Materials Research II, Semiconductors and Semimetals*; Tritt, T. M. *Ed.; Academic Press: San Diego* **2000**, *69*, 139.
10. Kuznetsov, V. L.; Kuznetsova, L. A.; Rowe, D. M. *J. Phys.: Condens. Matter*. **2003**, *15*, 5035.
11. Nolas, G. S.; Kaeser, M.; Littletonand, R. T.; Tritt, T. M. *Appl. Phys. Lett.* **2000**, *77*, 1855.
12. Morelli, D. T.; Meisner, G. P.; Chen, B. X.; Hu, S. Q.; Uher, C. *Phys. Rev. B* **1997**, *56*, 7376.
13. Chen, L. D.; Kawahara, T.; Tang, X. F.; Goto, T.; Hirai, T.; Dyck, J. S.; Chen, W.; Uher, C. *J. Appl. Phys*. **2001**, *90*, 1864.
14. Puyet, M.; Lenoir, B.; Dauscher, A.; Dehmas, M.; Stiewe, C.; Muller, E. *J. Appl. Phys*. **2004**, *95*, 4852.
15. Pei, Y. Z.; Chen, L. D.; Zhang, W.; Shi, X.; Bai, S. Q.; Zhao, X. Y.; Mei, Z. G.; Li, X. Y. *Appl. Phys. Lett*. **2006**, *89*, 221107.

16. Pei, Y. Z.; Yang, J.; Chen, L. D.; Zhang, W.; Salvador, J. R.; Yang, J. H. *Appl. Phys. Lett*. **2009**, *95*, 042101.

17. Sales, B. C.; Chakoumakos, B. C.; Mandrus, D. *Phys. Rev. B* **2000**, *61*, 2475.

18. Zhao, W.; Wei, P.; Zhang, Q.; Dong, C.; Liu, L.; Tang, X. *J. Am. Chem. Soc*. **2009**, *131*, 3713.

19. Shi, X.; Yang, J.; Salvador, J. R.; Chi, M.; Cho, J. Y.; Wang, H.; Bai, S.; Yang, J.; Zhang, W.; Chen, L. *J. Am. Chem. Soc*. **2011**, *133*, 7837.

20. Su, X.; Li, H.; Yan, Y.; Chi, H.; Tang, X.; Zhang, Q.; Uher, C. *J. Mater. Chem*. **2012**, *22*, 15628.

21. Mi, J. L.; Zhao, X. B.; Zhu, T. Z.; Tu, J. P.; Cao, G. S. *J. Alloys Compd*. **2006**, *417*, 269 .

22. Mi, J. L.; Zhu, T. J.; Zhao, X. B.; Ma, J. *J. Appl. Phys*. **200**7, *101*, 054314.

23. Toprak, M. S.; Stiewe, C.; Platzek, D.; Willams, S.; Bertini, L.; Rowe, M.; Gatti, C.; Zhang, Y.; Muhammed, M. *Adv. Funct. Mater.* **2004**, *14*, 1189.

24. Cable, R. E.; Schaak, R. *Chem. Mater.* **2005**, *17*, 6835.

25. Feng, B.; Xie, J.; Cao, G.; Zhu, T.; Zhao, X. *J. Mater. Chem. A* **2013**, *1*, 13111.

26. Gharleghi, A.; Pai, Y. -H.; Lin, F. -H.; Liu, C. J. *J. Mater. Chem. C*. **2014**, *2*, 4213.

27. Rodr´ıguez-Carvajal J. FULLPROF, A program for Rietveld refinement and pattern matching analysis abstracts of the Satellite Mtg on Powder Diffraction of the XV Congr. of the IUCr (Toulouse, France) **1990**, 127.

28. He, T.; Chen, J.; Rosenfeld, H. D.; Subramanian, M. A. *Chem. Mater*. **2006**, *18*, 759.

29. Popescu, A.; Woods, L. M.; Martin, J.; Nolas, G. S. *Phys. Rev. B* **2009**, *79*, 205302.

30. Martin, J.; Wang, L.; Chen, L.; Nolas, G. S. *Phys. Rev. B* **2009**, *79*, 115311.

31. Guin, S. N.; Chatterjee, A.; Negi, D. S.; Datta, R.; Biswas, K. *Energy Environ. Sci*. **2013**, *6*, 2603.

List of publications

1. Banik, A.; Biswas, K. Lead free thermoelectrics : promising performance in p-type $SnTe_{1-x}Se_x$ system. *J. Mater. Chem. A* **2014**, *2*, 9602.
2. Banik, A.; Shenoy, U. S.; Anand, S.; Waghmare, U. V.; Biswas, K. Mg Alloying in SnTe Facilitates Valence Band Convergence and Optimizes Thermoelectric Properties. *Chem. Mater*. **2015**, *27*, 581.
3. Banik, A.; Biswas, K. Low-temperature soft-chemical synthesis and thermoelectric properties of barium-filled *p*-type skutterudite nanocrystals. *Mater. Sci. Semicond. Process*, **2014**, *27*, 593.